

INFORMATION TO USERS

This manuscript has been reproduced from the microfilm master. UMI films the text directly from the original or copy submitted. Thus, some thesis and dissertation copies are in typewriter face, while others may be from any type of computer printer.

The quality of this reproduction is dependent upon the quality of the copy submitted. Broken or indistinct print, colored or poor quality illustrations and photographs, print bleedthrough, substandard margins, and improper alignment can adversely affect reproduction.

In the unlikely event that the author did not send UMI a complete manuscript and there are missing pages, these will be noted. Also, if unauthorized copyright material had to be removed, a note will indicate the deletion.

Oversize materials (e.g., maps, drawings, charts) are reproduced by sectioning the original, beginning at the upper left-hand corner and continuing from left to right in equal sections with small overlaps.

Photographs included in the original manuscript have been reproduced xerographically in this copy. Higher quality 6" x 9" black and white photographic prints are available for any photographs or illustrations appearing in this copy for an additional charge. Contact UMI directly to order.

ProQuest Information and Learning
300 North Zeeb Road, Ann Arbor, MI 48106-1346 USA
800-521-0600

UMI[®]

University of Alberta

**An Experimental Investigation of Interfacial Instabilities and
Entrainment in Exchange Flows Over a Smooth Sill**

by

Véronique M. Morin



**A thesis submitted to the Faculty of Graduate Studies and Research in partial
fulfillment of the requirements for the degree of Master of Science**

in

Water Resources Engineering

**Department of Civil & Environmental Engineering,
Edmonton, Alberta
Spring 2002**



**National Library
of Canada**

**Acquisitions and
Bibliographic Services**

**385 Wellington Street
Ottawa ON K1A 0N4
Canada**

**Bibliothèque nationale
du Canada**

**Acquisitions et
services bibliographiques**

**385, rue Wellington
Ottawa ON K1A 0N4
Canada**

Your file Votre référence

Our file Notre référence

The author has granted a non-exclusive licence allowing the National Library of Canada to reproduce, loan, distribute or sell copies of this thesis in microform, paper or electronic formats.

The author retains ownership of the copyright in this thesis. Neither the thesis nor substantial extracts from it may be printed or otherwise reproduced without the author's permission.

L'auteur a accordé une licence non exclusive permettant à la Bibliothèque nationale du Canada de reproduire, prêter, distribuer ou vendre des copies de cette thèse sous la forme de microfiche/film, de reproduction sur papier ou sur format électronique.

L'auteur conserve la propriété du droit d'auteur qui protège cette thèse. Ni la thèse ni des extraits substantiels de celle-ci ne doivent être imprimés ou autrement reproduits sans son autorisation.

0-612-69739-8

Canada

University of Alberta

Library Release Form

Name of Author: Véronique M. Morin
Title of Thesis: An Experimental Investigation of Interfacial Instabilities and Entrainment in Exchange Flows Over a Smooth Sill
Degree: Master of Science
Year this Degree Granted: 2002

Permission is hereby granted to the University of Alberta Library to reproduce single copies of this thesis and to lend or sell such copies for private, scholarly or scientific purposes only.

The author reserves all other publication and other rights in association with the copyright in the thesis, and except as herein before provided, neither the thesis nor any substantial portion thereof may be printed or otherwise reproduced in any material form whatever without the author's prior written permission.



584 Victoria Manor
Sherwood Park, Alberta, Canada
T8A 4N1

Dated January 7, 2002

To My Mother and Father for all of their love and support.

Abstract

A detailed experimental study examining the hydraulics and interfacial mixing of exchange flows passing over a smooth sill is presented. Measurements of the velocity field and the interface position were obtained using flow visualization and particle image velocimetry. Measured values of the flow rate, interface position, internal Froude number, and internal energy were compared with the predictions of internal hydraulic theory. These parameters were well predicted at the sill crest, but not in the supercritical regions of the flow; this is likely due to neglecting the effects of friction, streamline curvature, and entrainment. It was found that both the basin-scale internal seiche and the generation of Kelvin-Helmholtz instabilities at the interface produced large periodic fluctuations in the flow rate and in the interface position. Values of the entrainment coefficients for the exchange flow were considerably larger than the entrainment coefficients found for plane turbulent wall jets and gravity currents. The entrainment increased the flow rate in the upper layer by approximately 22 % downstream of the sill compared to that at the sill crest. The large amount of interfacial shear in an exchange flow is a major source of mixing at the stratified interface.

Acknowledgements

I am greatly indebted to my supervisors, Dr. D. Zhu and Dr. M. Loewen for their guidance, encouragement, and understanding throughout the research program. Their support and enthusiasm provided a constant source of inspiration.

Thank you to Perry Fedun, Instrumentation Engineering Technologist at the T. Blench Hydraulics Laboratory, for setting up the experimental arrangements and for his productive advise during the acquisition of data.

Thanks to all my colleagues, the laboratory technicians, and all the professors of the Water resources Group, Civil Engineering Department at the University of Alberta for their friendship. This provided for an enjoyable working atmosphere at the T. Blench Hydraulics Laboratory.

I deeply appreciate the financial support for this research project given from the Province of Alberta Scholarship.

Finally, I would like to express my sincere gratitude to my family and friends for their patience, encouragement, and support throughout my academic career.

Table of Contents

1.0	Introduction	1
2.0	Literature Review	3
2.1	Two-Layer Hydraulics	3
2.2	Mixing and Entrainment Studies	10
3.0	Experimental Apparatus and Technique	15
3.1	Experimental Design	15
3.2	Measurement Techniques	16
3.3	Experimental Errors	21
4.0	Hydraulics of the Flow	25
5.0	Interfacial Instability and Entrainment	32
5.1	Characteristics of the Interfacial Instabilities	32
5.2	Entrainment	39
6.0	Conclusions	42
7.0	References	44
	Appendix A – List of Programs Used for Data Processing	98
	Appendix B – Peak Locking Results	99
	Appendix C – Raw Shear Layer Thickness Data	102

List of Tables

Table 1: List of experiments.	48
Table 2: Results of the spectral analysis computed at the sill crest for both the flow rate and interface data. All data are in seconds.	49
Table 3: Frequencies determined from the spectra of the interface position at varying x locations for Experiment 1. Spectral resolution $\Delta f = 0.0083$ Hz.	50
Table 4: Frequencies determined from the spectra of the interface position at varying x locations for Experiment 2. Spectral resolution $\Delta f = 0.0111$ Hz.	50
Table 5: Frequencies determined from the spectra of the interface position at varying x locations for Experiment 3. Spectral resolution $\Delta f = 0.0139$ Hz.	50
Table 6: Comparison of the velocity computed from the cross-correlation of the interface position to the depth averaged velocity and the velocity at the density interface at varying x locations for Experiment 1.	51
Table 7: Comparison of the velocity computed from the cross-correlation of the interface position to the depth averaged velocity and the velocity at the density interface at varying x locations for Experiment 2.	51
Table 8: Comparison of the velocity computed from the cross-correlation of the interface position to the depth averaged velocity and the velocity at the density interface at varying x locations for Experiment 3.	52

List of Figures

Figure 1: Two-layer maximal exchange flow over a smooth sill.	53
Figure 2: Non-dimensional control curve plots.	54
Figure 3: Experimental Setup and Instrumentation: (a) plan view, (b) side view.	55
Figure 4: Photographs of the experimental setup.	56
Figure 5: Schematic of particle image velocimetry experimental setup.	57
Figure 6: (a) Sample raw PIV image, (b) the corresponding pre-processed image. Images taken from Experiment 3 with a 33 x 33 cm field of view.	58
Figure 7: (a) Sample raw velocity vector field, (b) the corresponding corrected and interpolated velocity vector field. Velocity fields taken from Experiment 3.	59
Figure 8: Sample interface position image taken from Experiment 1.	60
Figure 9: Series of images depicting the gravity current moving along the channel bed (images taken from Experiment 2 with a 1.5 s interval).	61
Figure 10: Series of images taken 6 minutes into Experiment 1; 1 s interval.	62
Figure 11: Series of images taken 4 minutes into Experiment 2; 1 s interval.	63
Figure 12: Series of images taken 3 minutes into Experiment 3; 1 s interval.	64
Figure 13: Flow rate measured in the upper layer at the sill crest ($x=0$ cm) for Experiment 1, (b) spectrum of the flow rate (spectral resolution $\Delta f = 0.0083$ Hz).	65
Figure 14: Flow rate measured in the upper layer at the sill crest ($x=0$ cm) for Experiment 2, (b) spectrum of the flow rate (spectral resolution $\Delta f = 0.0104$ Hz).	66
Figure 15: Flow rate measured in the upper layer at the sill crest ($x=0$ cm) for Experiment 3, (b) spectrum of the flow rate (spectral resolution $\Delta f = 0.0139$ Hz).	67
Figure 16: Mean interface position of Experiments 1, 2, and 3 measured along the sill compared to the theoretical interface prediction.	68
Figure 17: Average velocity profiles for Experiment 1 showing mean interface position.	69
Figure 18: Average velocity profiles for Experiment 2 showing mean interface position.	70

Figure 19: Average velocity profiles for Experiment 3 showing mean interface position.	71
Figure 20: Variation of the flow rate divided by the sill crest flow rate along the sill for Experiments 1, 2, and 3.	72
Figure 21: (a) Comparison of predictions of internal energy with experimental measurements for maximal exchange flow, (b) comparison of predictions of internal Froude number measurements for maximal exchange flow (— inviscid, hydrostatic prediction; ●, *, ▲ inviscid hydrostatic prediction of q with measured value of y for Experiments 1,2, and 3; ○, +, Δ measured q and measured y for Experiments 1, 2, and 3).	73
Figure 22: Images of Experiment 4a (6 minutes and 20 s into the experiment, 3 s interval).	74
Figure 23: Average velocity profiles for Experiment 4a.	76
Figure 24: Variation of (a) the shear layer thickness calculated from average velocity profiles, δ^* , and (b) the shear layer thickness calculated from instantaneous velocity profiles, δ .	77
Figure 25: Variation of (a) the Reynolds number, R_θ , and (b) the Richardson number, R_i along the sill.	78
Figure 26: Variation of interface position with time at different x locations for Experiment 1, (b) spectrum of the interface position time series (spectral resolution $\Delta f = 0.0083$ Hz).	79
Figure 27: Variation of interface position with time at different x locations for Experiment 2, (b) spectrum of the interface position time series (spectral resolution $\Delta f = 0.0111$ Hz).	81
Figure 28: Variation of interface position with time at different x locations for Experiment 3, (b) spectrum of the interface position time series (spectral resolution $\Delta f = 0.0139$ Hz).	83
Figure 29: Series of instantaneous vorticity plots calculated from Experiment 3. Vorticity is expressed in s^{-1} .	85
Figure 30: Series of instantaneous turbulent kinetic energy plots calculated from Experiment 3. Turbulent kinetic energy is expressed in cm^2/s^2 .	89
Figure 31: (a) Average vorticity field (s^{-1}) computed for Experiment 1, (b) average turbulent kinetic energy (expressed in cm^2/s^2) field computed for Experiment 1.	93
Figure 32: (a) Average vorticity field (s^{-1}) computed for Experiment 2, (b) average turbulent kinetic energy (expressed in cm^2/s^2) field computed for Experiment 2.	94

Figure 33: (a) Average vorticity field (s^{-1}) computed for Experiment 3, (b) average turbulent kinetic energy (expressed in cm^2/s^2) field computed for Experiment 3. 95

Figure 34: Entrainment of fluid from the upper into the lower layer. 96

Figure 35: (a) Variation of Ri^* ($^\circ$, $+$, Δ Experiments 1, 2, and 3, respectively), (b) variation of the entrainment coefficient along the sill ($^\circ$, $+$, Δ using Equation 28 for Experiments 1, 2, and 3, respectively; \cdots , $---$, $---$ entrainment results for gravity currents using Parker et. al.'s (1987) relationship and Ri^* values from Experiments 1, 2, and 3, respectively; $---$ entrainment coefficient for a plane turbulent wall jet (Rajaratnam, 1976). 97

List of Symbols

b	width of the rectangular channel
C_i	propagation speed of interfacial waves
e_r	entrainment rate
E	internal energy for two-layer flow
E_i	mechanical energy for layer i
f	frequency
F	Froude number
F_i	densimetric Froude number for layer i
F_Δ	stability Froude number
g	gravitational acceleration
g'	reduced gravitational acceleration
G	composite (or internal) Froude number
h	height of sill
h_s	height of sill at the sill crest
H	total depth of flow
L_s	length of sill
p_i	pressure in layer i
p_s	pressure at water surface
q_i	flow rate per unit width of channel in layer i
Re	Reynolds number
R_i	bulk Richardson number
S_c	slope due to flow curvature
S_f	friction slope
S_o	topographic slope

t	time
T	characteristic time scale
TKE	turbulent kinetic energy
u	streamwise velocity
u'	turbulent component of the streamwise velocity
U_i	streamwise mean velocity in layer i
v	cross-stream velocity
v'	turbulent component of the cross-stream velocity
w	vertical velocity
w'	turbulent component of the vertical velocity
x	horizontal coordinate (with origin at sill crest)
z_i	thickness of layer i
z_{ie}	thickness of layer i at the channel exit
z_{io}	thickness of layer i at the sill crest
z	vertical elevation
α_e	entrainment coefficient
δ	shear layer thickness
ε	relative density difference
λ_{\pm}	phase speed of small disturbances with respect to channel banks
ν	kinematic viscosity
ρ_i	density of layer i
ω	vorticity

1.0 Introduction

Adjacent water bodies connected by straits or channels often have slightly different densities as a result of differences in salinity, temperature, and/or sediment concentration. This difference in density causes the fluids to exchange. Such exchange flows are common in nature; for example, the exchange of more saline Mediterranean Sea water with less saline Atlantic Ocean water through the Strait of Gibraltar (Armi and Farmer, 1988) and the summertime exchange of warmer heavily polluted Hamilton Harbor water with cooler (more dense) Lake Ontario water through the Burlington ship canal (Hamblin and Lawrence, 1990). Even slight differences in density can cause enormous amounts of fluid to exchange. For example, the density difference between the Atlantic Ocean and the Mediterranean Sea water is approximately two parts per thousand, yet the exchange flow in the Strait of Gibraltar is in the order of magnitude of $1,000,000 \text{ m}^3/\text{s}$ each way. At the interface of such exchange flows, interfacial instabilities can develop. These instabilities can cause mixing between the upper and lower layers, which directly impacts the circulation and water quality of both water bodies. The goal of the present study is to understand these phenomena through laboratory experiments.

Earlier studies have focused on the hydraulics of such exchange flows (i.e. Farmer and Armi, 1986). The effects of friction and non-hydrostatic forces were considered by Zhu and Lawrence (2000). Interfacial instabilities generated in exchange flows were also studied by Zhu and Lawrence (2001) where the focus was on the subcritical section of the flow and only Holmboe instabilities were observed. Wilkinson and Wood (1983) observed that the supercritical flow down a sill causes a layer of intermediate density. Experimental observations by Zhu et al. (2001) and Pawlak and Armi (2000) indicate that the interfacial mixing was caused by large-scale interfacial instabilities.

In this study, experiments were performed in a tank where steady two-layer exchange flow of fresh and salt water over a smooth bottom sill could be examined. The section of supercritical flow down the sill was the main focus of this research. Shear-generated interfacial instabilities and the resulting flow entrainment were examined. It is important to understand the entrainment and mixing that occurs in exchange flows in order to predict the water quality of both water bodies connected by such channels. This study will help to improve our understanding of many geophysical flows such as the stratified flow over the Knight Inlet sill (Farmer and Armi, 1999) and airflow over ridges.

This thesis is structured as follows. Section 2 reviews the hydraulics of two-layer flows and previous experimental and numerical studies examining entrainment and mixing. A brief review of gravity currents is also presented for the purpose of comparing entrainment coefficients in later discussions. Section 3 discusses the experimental setup and instrumentation, the measurement techniques used, and the estimated experimental error. Results of the experimental study are presented in Sections 4 and 5. In Section 4, measured parameters are compared to their theoretical predictions (using two-layer hydraulic theory). Characteristics of the interfacial instabilities generated in the exchange flow and the associated entrainment is discussed in Section 5. Conclusions are presented in Section 6.

2.0 Literature Review

2.1 Two Layer Hydraulics

Two layer flows have been studied both theoretically and experimentally for many years. Both Long (1954) and Baines (1984) conducted towing tank experiments to investigate two-layer flows over an obstacle. Farmer and Armi (1986) investigated flows passing over a sill, through a contraction, and through a combination of both a sill and a contraction. Lawrence (1993) investigated steady two-layer flow over a fixed obstacle both theoretically and experimentally. In his experiments the obstacle was fixed at the bottom of a flume and the two-layer fluid system flowed over it at a constant rate, rather than towing the obstacle through still water. Zhu and Lawrence (2000) extended the basic hydraulic theory to include the effects of friction and streamline curvature for the case of flow over a sill. Internal hydraulic theory is summarized in this section.

Consider a two-layer exchange flow over a two-dimensional smooth sill in a rectangular channel, as illustrated in Figure 1. The rectangular channel connects two reservoirs with fluids of slightly different densities. The case where the denser bottom layer flows from left to right and the less dense top layer flows from right to left will be considered here. Therefore, the interface level rises from the right side of the sill to the right-hand reservoir.

Flow over a sill is turbulent and viscous; however, by incorporating a series of simplifying assumptions, a set of approximate equations can be derived. It is assumed that the flow is irrotational, inviscid and in a steady state. If the maximum slope of the sill is small, the streamlines of the flow will be essentially horizontal. Therefore, the vertical velocity is negligible, and the flow can be considered to be one-dimensional. Let us assume that a hydrostatic pressure distribution adequately represents the pressure distribution. Long (1954) stated that the hydrostatic pressure distribution is applicable if

the sill is 'gentle'; that is if the minimum radius of curvature is much greater than the height of the sill. The 'layered flow assumption', where the velocity only varies in the direction of flow and the density is constant within each layer, is applied. And finally, it is assumed that no mixing occurs between the two layers.

The equations for two layer flows can be derived using the continuity equation for the two layers together with the energy equation for both layers (Denton, 1987; Lawrence, 1993). Applying the above mentioned assumptions, the mechanical energy for layer i is

$$E_i = p_i + \rho_i gz + \frac{1}{2} \rho_i U_i^2 \quad [1]$$

where p , ρ , z , and U are the pressure, density, vertical elevation, and horizontal velocity, respectively. Neglecting the effects of friction and in the absence of flow discontinuities, such as flow separation and hydraulic jumps, the energy head is conserved. The pressure in each layer (using the hydrostatic assumption) can be expressed as the following

$$p_1(z) = p_s + \rho_1 g(z_1 + z_2 + h - z) \quad [2]$$

$$p_2(z) = p_s + \rho_1 g z_1 + \rho_2 g(z_2 + h - z) \quad [3]$$

where p_s , z_1 , z_2 , and h are the pressure at the water surface, the upper layer thickness, the lower layer thickness, and the height of the sill, respectively. Substituting Equations [2] and [3] into Equation [1], and applying zero pressure at the free surface the energy head for each layer can be expressed as

$$E_1 = \rho_1 g H + \frac{1}{2} \rho_1 U_1^2 \quad [4]$$

$$E_2 = \rho_1 g H + (\rho_2 - \rho_1) g(z_2 - h) + \frac{1}{2} \rho_2 U_2^2 \quad [5]$$

where H is the total depth.

The Boussinesq approximation can be applied to flows where the density difference between the two layers is very small. This approximation states that the variation of density can be neglected everywhere except in the buoyancy terms. For such flows where the relative density difference is small, i.e. $\varepsilon = (\rho_2 - \rho_1)/\rho_2 \ll 1$, the slope of the free surface is negligible compared to that of the interface. This is commonly referred to as the “rigid lid” or horizontal free surface assumption. Thus the total depth

$$H = z_1 + z_2 + h \quad [6]$$

remains a constant.

In two-layer stratified flow, we define the internal energy, E , as

$$E = \frac{E_2 - E_1}{(\rho_2 - \rho_1)g} \quad [7]$$

Applying the Boussinesq approximation and replacing E_2 and E_1 in Equation [7] with Equations [4] and [5] leads to

$$E = z_2 + h + \frac{1}{2g'}(U_2^2 - U_1^2) \quad [8]$$

where $g' = \varepsilon g$ is called the reduced gravitational acceleration. As mentioned previously, for inviscid, irrotational flow, the energy head along a channel is conserved for each layer if flow separation and hydraulic jumps are not present. Consequently, the internal energy must also be constant along the channel, and $dE/dx = 0$, where x is the horizontal distance along the channel. Differentiating Equation [8] with respect to x leads to an equation that represents the variation of the interface slope at any given position, except where discontinuities occur.

$$\frac{d(z_2 + h)}{dx} = \frac{-1}{1 - G^2} \left\{ F_2^2 h_x + (F_1^2 z_1 - F_2^2 z_2) \frac{b_x}{b} \right\} \quad [9]$$

In the above equation the subscript x denotes differentiation with respect to x , b is the channel width, $F_i^2 = U_i^2/g'z_i$ is the densimetric Froude number for layer i , and $G = \sqrt{F_1^2 + F_2^2}$ is the composite (or internal) Froude number.

If the channel has a constant width, then b_x is equal to zero, and Equation [9] reduces to

$$\frac{d(z_2 + h)}{dx} = \frac{-F_2^2 \frac{dh}{dx}}{1 - G^2} \quad [10]$$

The numerator on the right hand side of the equation is simply the topographic slope, $S_o = F_2^2 dh/dx$. Zhu and Lawrence (2000) extended Equation [10] to include friction and non-hydrostatic forces due to streamline curvature.

$$\frac{d(z_2 + h)}{dx} = \frac{S_f - S_o - S_c}{1 - G^2} \quad [11]$$

where S_f is the friction slope and S_c is the slope due to flow curvature.

Before examining the hydraulic controls of two-layer flows, one layer hydraulics will first be reviewed. In one layer flows, the phase speed of small disturbances with respect to the channel banks is

$$\lambda_{\pm} = U \pm \sqrt{gz} \quad [12]$$

where U is the convective mean velocity and \sqrt{gz} is the phase speed of the infinitesimal long waves. The Froude Number, F , is the ratio of the convective velocity to the phase speed. Multiplying the two phase speeds together leads to the equation below.

$$F^2 - 1 = \frac{\lambda_+ \lambda_-}{gz} \quad [13]$$

When the Froude number is less than unity, or alternatively, when the product of the two phase speeds is less than zero, the disturbances can propagate in both directions and the flow is said to be subcritical. Conversely, when the Froude number is larger than

one, or the product of the two phase speeds is greater than zero, the disturbances can only propagate downstream and the flow is supercritical. And finally, the flow is critical when the Froude number is equal to unity.

Schiff and Schonfeld (1953) solved the propagation speed of interfacial long waves with respect to the channel bank in two layer flows.

$$\lambda_{\pm} = \frac{U_1 z_2 + U_2 z_1}{z_1 + z_2} \pm \left(\frac{g' z_1 z_2}{z_1 + z_2} (1 - F_{\Delta}^2) \right)^{1/2} \quad [14]$$

Where $F_{\Delta}^2 = (U_2 - U_1)^2 / [g'(z_2 + z_1)]$ is the stability Froude number. Note that $F_{\Delta}^2 \leq 1$ to avoid imaginary internal phase speeds. The product of the two interfacial long waves will generate the following equation for two layer flows.

$$G^2 - 1 = \frac{z_1 + z_2}{z_1 z_2} \lambda_+ \lambda_- \quad [15]$$

In two layer flows, the composite Froude number G describes the criticality of the flow. Thus, when $G < 1$, or $\lambda_+ \lambda_- < 0$, disturbances can propagate in both directions, and the flow is internally subcritical. When $G > 1$, or $\lambda_+ \lambda_- > 0$, small disturbances can only propagate downstream and the flow is internally supercritical. The flow is internally critical at locations where $G = 1$. Even though the composite Froude number is not a Froude number in the strictest sense (it is not the ratio of convective velocity to a long wave phase speed), Lawrence (1990) showed that it correctly specifies the criticality of the flow.

Two-layer flows can have up to two internal controls, whereas, single-layer flows can only have one control. Farmer and Armi (1986) identified two basic flow regimes: maximal exchange and submaximal exchange. The development of the hydraulic controls in two-layer flow over a sill will be illustrated using the exchange flow in Figure 1. The exchange flow commences once the barrier separating the two reservoirs is removed. In the absence of barotropic forcing, the flow in the upper layer, q_1 , will equal

the flow in the lower layer, q_2 . The bottom, more dense layer passes from left to right and the top, less dense layer moves from right to left. The control at the sill crest is first established. As long as the depth of the lower layer at the channel exit remains below a certain level, the flow will remain subcritical at the exit. To the right of the sill crest, the flow will be internally supercritical, and therefore, any disturbances in the right reservoir will not affect the exchange flow. The flow rate will increase as the interface in the left reservoir rises; however, any change in the level of the right reservoir will have no effect on the flow rate due to the supercritical flow on the right side of the sill. This flow regime is called submaximal exchange.

As the depth of the lower layer at the channel exit rises, the flow rate will increase and the thickness of the upper layer will decrease until eventually, a control is established at the left hand exit. Therefore, the flow is critical at both the sill crest and at the left hand exit. Between the two controls the flow is internally subcritical. To the left of the exit control, supercritical flow will result with any further increase in the depth of the lower layer at the channel exit, but the flow rate will not be increased. To the right of the sill crest the lower layer accelerates down the sill as supercritical flow and eventually matches the level of the right hand reservoir interface through some mixing mechanisms. These mixing mechanisms do not affect the flow rate of the exchange flow since the supercritical flow isolates the control region. Once the two controls have been established, the flow rate can no longer be increased. This concept of having two internal controls is what characterizes maximal exchange. Note that the location of the internal controls may shift if other factors such as friction, and streamline curvature are considered (Zhu and Lawrence, 2000). Given specific channel geometry and a density difference between the two reservoirs, the maximal exchange exhibits the maximum flow rate possible.

Using the internal hydraulic theory presented above, the maximal exchange flow rate can be determined. For a channel of constant width, the unknowns include the flow rate in the upper layer, q_1 , the flow rate in the lower layer, q_2 , the water depths of the upper and lower layers at the sill crest, z_{1o} and z_{2o} , respectively, and the water depths of the upper and lower layers at the channel exit, z_{1e} and z_{2e} , respectively. Hence, six equations are necessary to solve for the maximal exchange flow rate. In the absence of barotropic forcing, and at steady state, the flow rate in the upper layer is equal to the flow rate in the lower layer.

$$q_1 = q_2 \quad [16]$$

The two equations for the total water depths at the sill crest and at the exit control are, respectively.

$$z_{1o} + z_{2o} + h = H \quad [17]$$

$$z_{1e} + z_{2e} = H \quad [18]$$

Also, for maximal exchange flow, the composite Froude number $G^2 = 1$ at both controls. Therefore, the composite Froude number is equal to unity at the sill crest and at the exit.

$$\frac{q_1^2}{g' z_{1o}^3} + \frac{q_2^2}{g' z_{2o}^3} = 1 \quad [19]$$

$$\frac{q_1^2}{g' z_{1e}^3} + \frac{q_2^2}{g' z_{2e}^3} = 1 \quad [20]$$

The final equation uses the conservation of energy and equates the internal energy, E , at the sill crest to the internal energy at the exit control.

$$z_{2o} + h_o + \frac{1}{2g'} \left(\frac{q_2^2}{z_{2o}^2} - \frac{q_1^2}{z_{1o}^2} \right) = z_{2e} + \frac{1}{2g'} \left(\frac{q_2^2}{z_{2e}^2} - \frac{q_1^2}{z_{2e}^2} \right) \quad [21]$$

With Equations [16] – [21], the six unknowns can be determined.

Zhu (2001) presented a control curve approach that graphically determines the flow rate prediction. In this approach, the relationship between the internal energy versus the flow rate is plotted for both the sill and the exit control. For a range of z_2 values, z_1 can be determined given the total water depth and the height of the sill using Equation 6. Values of the flow rate can then be determined using the condition that at the control, $G = 1$. And finally, the internal energy can be determined using Equation 8. This relationship between the internal energy and the flow rate can be plotted for both the sill crest control (given $h = h_s$) and the exit control (given $h = 0$). The predicted flow rate for the given channel geometry can then be determined from the intersection of the two curves. The control curve approach is useful in identifying the number of controls as well as the actual locations of these controls. In the flow shown in Figure 1, the controls are located at the sill crest and at the channel exit. This approach was used to determine the predicted flow rate for our experimental setup. The non-dimensional control curves for the sill crest and the channel exit are plotted in Figure 2. The intersection between the two control curves gives a predicted value of the flow rate. Later, it will be useful to compare the flow rates determined experimentally to the theoretical prediction.

2.2 Mixing and Entrainment Studies

Velocity gradients present at the interface of two-layer flows generate interfacial shear, which in turn, can generate interfacial instabilities. These instabilities may produce interfacial turbulence and cause interfacial mixing. Sheared density interfaces have been studied since the work of Taylor (1931) and Goldstein (1931). Their analysis led to an equation governing the stability of inviscid, parallel, stratified shear flows to two-dimensional infinitesimal disturbances, which later became known as the Taylor-Goldstein equation.

Kelvin-Helmholtz instabilities are considered the primary mode of instabilities generated in stratified shear flows. They are characterized by the rolling up of the density interface; causing two-dimensional billows of zero phase speed relative to the mean velocity at the interface. Holmboe (1962) applied temporal linear stability analysis to piecewise linear velocity profiles with a two-layer density structure. He predicted that for inviscid flows where the shear layer thickness is much greater than the density interface a second mode of instability would be generated. These instabilities were later termed Holmboe instabilities, and are characterized by two sets of waves with one cusping into the upper layer and the other into the lower layer. The waves have the same growth rate and wave speed, but propagate in opposite directions with respect to the mean flow velocity.

The relative strength of the stratification to the strength of the velocity shear is measured using the bulk Richardson number,

$$R_i = g'\delta/\Delta U^2 \quad [22]$$

where δ is the shear layer thickness, and ΔU is the velocity difference between the upper and lower layer. The bulk Richardson number has been used to identify which type of instability will occur at the interface. Holmboe (1962) studied the case where the flow has a two-layer density structure with a location that is symmetric about the center of the shear layer. Using linear stability analysis, he found that K-H instabilities can only occur when $R_i < 0.071$, while Holmboe instabilities could occur for any positive bulk Richardson number.

Hazel (1972) extended Holmboe's analysis by allowing a finite density layer thickness and studying the effects of varying the relative scales of the density and velocity interfaces. He found that the Holmboe mode may be generated whenever the thickness of the shear region exceeds the thickness of the density interface by a factor

of two. Using linear stability analysis, Haigh and Lawrence (1999) studied the effect of displacing a thin density interface with respect to the center of the shear layer on the stability of an inviscid, stably stratified parallel flow. They showed that for symmetric flows where the interface displacement is zero, K-H instabilities are possible for $R_i < 0.071$; however when $0.046 < R_i < 0.071$, Holmboe instabilities are more unstable than K-H instabilities. Haigh and Lawrence (1999) also found that when the interface displacement is non-zero, the symmetry of the background flow is broken, and one mode of the Holmboe instability has a larger growth rate than the other. Therefore, instead of having two waves, as characterized by the Holmboe instability, the observed wave exhibits a “one-sidedness” with the wave protruding into one layer only.

Early experimental studies of mixing layers were conducted in spatially evolving splitter plate configurations (Roshko, 1976; Koop and Browand, 1979) or in temporally evolving tilting tube facilities (Thorpe, 1968, 1971, 1973). The existence of organized two-dimensional vortical structures in the mixing layer was documented in these investigations. In the experiments conducted by Thorpe (1968, 1971, 1973) the velocity interface thickness approximately equaled the density interface thickness. Browand and Wang (1972) investigated the spatial growth characteristics for the case where the density interface is positioned at the midpoint of the sheared region through a series of experiments. Lawrence, Browand, and Redekopp (1991) investigated the stability of stratified shear flows when the density interface is much thinner than, and displaced with respect to, the velocity interface. Experiments performed in mixing layer channels found that an offset in the centers of the velocity and density interfaces resulted in the dominance of one of the two Holmboe modes. Recently, Hogg and Ivey (2001) found that the transition of KH instabilities to Holmboe instabilities occurred at $R_i = 0.08$ for their experimental conditions.

Pawlak and Armi (1998) examined the vortex mechanisms developed in a stratified shear layer subjected to spatial acceleration in a hydraulically controlled wedge flow. They observed that spatial acceleration and buoyancy caused the developing vortex core to pinch off and separate from the vorticity source at the interface. The original vortex core would convect slowly downstream and as a secondary core developed, the original core would eventually interact with the following upstream structure. Pawlak and Armi (2000) conducted experiments that examined mixing and entrainment in a hydraulically controlled wedge flow. Two distinct regions were identified: an initial region of low shear layer Richardson number characterized by rapid growth of the mixing layer and high entrainment rates called the transition region, and a subsequent high Richardson number region characterized by weak entrainment and the collapse of turbulence from the initial region. They calculated entrainment rates within each region and estimated the length of the transition region for the various slopes considered.

Gravity currents and the associated entrainment have also been studied extensively. A gravity current is a mass of dense fluid that moves forward into a slightly less dense fluid. Ellison and Turner (1959) demonstrated that the entrainment rate of the upper layer into the lower layer, e_r , is related to the Richardson number, R_i . In their calculations, the Richardson number was defined using the thickness of the lower layer as the vertical scale. They found that decreasing the Richardson number increased the amount of mixing across the interface, and; hence, increased the entrainment of low-momentum fluid into the density current. Parker et al. (1987) studied turbidity currents, and defined a relationship relating the entrainment rate to the bulk Richardson number;

$$e_r = \frac{0.075}{(1 + 718R_i^{2.4})^{0.5}} \quad [23]$$

It will be useful to compare such entrainment rate relationships for gravity currents with the results of our exchange flow study. Refer to Alavian et al. (1992) for a detailed summary of the work conducted on gravity currents.

3.0 Experimental Apparatus and Technique

3.1 Experimental Design

Laboratory experiments of exchange flows were conducted in a water tank at the T. Blench Hydraulics Laboratory, University of Alberta, Edmonton, Alberta. A schematic of the experimental setup and instrumentation is shown in Figure 3. The tank was divided into two reservoirs that were connected by a rectangular channel of constant width $b = 10$ cm. A smooth bottom sill was placed in the rectangular channel with its crest located approximately 35 cm from the left hand end of the channel. The sill followed the shape $h(x) = h_m \cos^2(\pi x/L_s)$, with $h_m = 10$ cm and $L_s = 50$ cm. Also, for some of the experiments, a bottom weir was added to the right hand side of the channel, approximately 110 cm away from the sill crest. Figure 4 presents photographs of the experimental setup. The experimental setup detailed above enabled us to create an exchange flow where the characteristics of an accelerating flow field could be investigated for flow over a sill.

Table 1 presents a detailed list of the 7 experiments conducted. The density difference between the two layers, the field of view, and the weir height at the right hand side of the channel were varied to study a range of experimental conditions. In Experiments 1, 2, and 3 the density difference between the two layers was varied, with the reduced gravitational acceleration g' equal to 1.62, 3.23 and 6.47 cm/s², respectively. The field of view for these experiments focused on the sill region with the goal of studying the instabilities generated at the interface and the associated entrainment for varying densities. At each density difference, the experiment was repeated at least once; one experiment used dye to obtain the interface position and another experiment was conducted without dye to obtain the velocity field.

Experiments 4a-d focused on the area downstream of the sill. These experiments were performed in order to obtain information on the transition of internally supercritical flow to internally subcritical flow, with g' equal to 1.62 cm/s^2 . In addition, the effects of a bottom weir with heights of 2.0, 4.5 and 9.0 cm, for Experiments 4b, 4c, and 4d were investigated. In Experiment 4a, both the velocity field in the upper layer and the interface position were measured. In Experiments 4b-d only the interface position camera was used.

3.2 Measurement Techniques

In all experiments, the tank was filled with tap water to a depth of 30 cm. A barrier was then inserted into the rectangular channel to separate the two reservoirs. A known amount of salt (NaCl) was added into the left hand reservoir to create the driving buoyancy force. The water temperature was recorded and the density of each water body was determined based on the water temperature and salt concentration. Rhodamine 6G dye was added to the salt water in order to visualize the lower layer. The concentration of Rhodamine 6G was always kept below 0.5 g/m^3 to ensure that the dye remained within the linear range of the luminescence-concentration relation (Pawlak and Armi, 1998). The water in both reservoirs was seeded with silver coated glass spheres having a mean diameter of $15 \text{ }\mu\text{m}$ and a specific gravity of 1.65 (Potters Industries, Paoli, Pennsylvania). A reference grid was placed on the channel and a single frame was captured prior to each experiment in order to determine the position of the physical coordinates. Digital particle image velocimetry (DPIV) was used to measure the velocity field of the exchange flow and laser induced fluorescence (LIF) were used to obtain the position of the interface.

The presence of the Rhodamine dye in the salt water made it difficult to detect the tracer particles in the lower layer, and hence, prevented PIV measurements in the

lower layer when dye was present. Likewise, the silver coated spherical particles interfered with the measurements of the interface position. Therefore, low-pass and high-pass filters were used to filter out light at the undesired wavelengths. Rhodamine 6G has a wavelength of 590 nm and the argon-ion laser (which illuminated the particles) was operating at a wavelength of 514 nm. To obtain the position of the interface, a high-pass filter with a cutoff of 520 nm (Melles Griot Inc., Irvine, California) was placed in front of the interface position camera to filter out the reflections of the tracer particles illuminated by the laser light. The particles were completely filtered out of the images and a sharp interface existed between the dyed lower layer and the upper layer. A low pass filter (Melles Griot Inc., Irvine, California) with a typical rejection range of 570 to 680 nm was placed in front of the PIV camera with the intention of filtering out the Rhodamine dye. The filter did not work as intended; however, and the dye in the lower layer was still visible in the images. This filter likely did not have a sharp enough cutoff, and so light at the wavelength of the Rhodamine dye was still able to pass. Since the filters did not work as intended, Experiments 1, 2, and 3 were repeated at least once; one experiment used dye to obtain the interface position and another experiment was conducted without dye to enable PIV measurements in the lower layer.

DPIV is a non-intrusive measurement technique that is capable of measuring two-dimensional velocities at many points in a flow field, simultaneously. The main steps for particle image velocimetry are as follows: image acquisition (requiring an appropriate experimental setup), image processing (to compute the raw velocity vectors), velocity vector analysis and post-processing, and finally, error analysis.

The experimental setup of a typical DPIV system consists of a light source, light sheet optics, seeding particles, a camera, and a PC equipped with a frame grabber and image acquisition software. A 5W Argon-ion laser (Stabilite 2017, Spectra-Physics Lasers, Mountain View, California) operating at a wavelength of 514 nm was used as the

light source for the experiments conducted in this study. The argon-ion laser produces a continuous beam of light. An optical fiber equipped with light sheet optics (OZ Optics Ltd., Nepean, Ontario) was used to deliver the laser beam to the plane of study. The fiber optic head was placed 130 cm above the channel bed, creating a 2 mm thick light sheet that illuminated an 80 cm long section of the channel at the water surface. The flow was then seeded with the silver coated glass tracer particles. A digital CCD camera (Pulnix TM-1040, Pulnix America Inc., Sunnyvale, California) with a resolution of 1008 by 1008 pixels with a 10-bit dynamic range was used to record the PIV images. The field of view of a typical PIV image was approximately 32 x 32 cm, giving a true resolution of 0.03 cm/pixel. The camera was connected to a Pentium III class personal computer equipped with a frame grabber (Road Runner, Bitflow, Woburn, Massachusetts), and image acquisition software (Video Savant , IO Industries Inc., London, Ontario). A schematic diagram of the PIV system used in this study is illustrated in Figure 5.

In a traditional PIV system, the time separation between an image pair, Δt , is determined by the time separation between the laser pulses of a pulsed laser. In our experimental setup, the argon-ion laser produced a continuous beam of light. As a result, the time separation between the images was determined by the frame rate of the images acquired. The CCD camera can digitize images at rates up to 30 frames per second; however, the image acquisition software (Video Savant) enabled the images to be grabbed at any specified frame rate less than 30 frames per second. This technique made for a simpler PIV system, which worked well in our experiments because of the relatively low velocities encountered. In experiments 1, 2, and 3, images were collected at 10, 30, and 30 Hz for 11, 7, and 9 minutes, respectively. This corresponded to enormous amounts of data with each PIV experiment using 6, 12, and 15 Gigabytes of disk space to store the PIV images.

Once the images were acquired, they were exported, and then pre-processed. In Figures 6(a) and (b), a sample raw image and the corresponding pre-processed image are displayed. The areas above the water surface and below the lowermost part of the channel bed were cropped. Also, particles located along the bed caused a bright white line to appear in the images that defined the position of the bed (Figure 6(a)). This bright white line affected the cross-correlation near the channel bed; and was therefore set to the background grayscale value (Figure 6(b)).

The image pairs were then processed using a PIV algorithm to compute the velocity fields. The basic concept of a PIV scheme is as follows. The first image is split into sub-regions called interrogation windows and the second image is split into sub-regions called search windows. Cross-correlation of these sub-regions within an image pair gives the average displacement of all of the particles within the interrogation window. Dividing this displacement by the time separation between the two images gives the instantaneous velocity vector for that interrogation window. This process is then repeated for all the interrogation regions to obtain the velocity field over the entire field of view.

A standard cross-correlation PIV algorithm written by Marxen (1998) was used. In this method, the cross-correlation is computed between an interrogation window in the first image and a search window in the second image. The interrogation window size in the first image was set to 16x16 pixels in Experiment 1 and 32x32 pixels in Experiments 2 and 3. The search window size in the second image was always set to 64x64 pixels. Allowing the search window to be bigger than the interrogation window increases the likelihood that all of the particles in the interrogation window remain in the search window. In cases where the interrogation window was set to 32x32 pixels, a 50 % window overlap was used to increase the nominal resolution to 16x16 pixels. This resulted in a true resolution of approximately 5 mm for the velocity vectors in a typical

PIV experiment. A sub-pixel peak fitting scheme was used to obtain sub-pixel accuracy. The three-point Gaussian estimator was used because it has been found to be the most accurate scheme for determining sub-pixel accuracy (Siddiqui et al., 2001).

Post-processing of the raw velocity fields involved identifying and correcting spurious vectors and interpolating the raw data onto a regular grid. A scheme developed by Siddiqui et al. (2001) was adapted and used for the post-processing. The coordinates of the channel bed profile was used to discard all of the velocity vectors below the sill. Next, the spurious vectors were identified and corrected using a local median test. It has been shown that the local median test is a more robust method of correcting spurious vectors than the local mean test (Westerweel, 1994). Both the magnitude and direction of each vector was compared to the local median value of the eight or fewer neighboring vectors, depending on the location of the vector. Spurious vectors were replaced with the local median value. On average, it was found that 7 % of the vectors were spurious. Once the spurious vectors were corrected, the irregularly spaced velocity vectors were interpolated onto a regular grid using Adaptive Gaussian Window (AGW) interpolation (Agüí and Jiménez, 1987). Velocity fields calculated at 5, 15, and 15 Hz for Experiments 1, 2, and 3, respectively, were used to obtain volumetric flow rates, shear layer thickness, vorticity fields, and turbulent kinetic energy fields. Figures 7(a) and (b) illustrate a sample raw velocity vector field and the corresponding corrected and interpolated velocity vector field, respectively.

To obtain the position of the interface, a Sony Digital 8 video camera with a resolution of 640 by 480 pixels recorded images of the dyed lower layer. A typical interface image had a field of view of approximately 45 by 34 cm, giving a true resolution of 0.07 cm/pixel. A sharp interface existed between the dyed lower layer and the upper layer. Images were digitized at a frame rate of 5 frames/s for Experiments 1, 2, and 3. A sample interface position image is displayed in Figure 8. The interface position was

determined by thresholding the image based on the differing grayscale values of the upper and lower layers.

3.2 Experimental Errors

DPIV measurements are subject to error due to the velocity gradients, particle density, particle diameter, out-of-plane-motion, dynamic range, peak locking, and AGW interpolation (Cowen and Monismith, 1997). In this study, the particles had a size of 15 μm , giving a non-dimensional particle diameter of 0.05 pixels/pixel. Particles smaller than one pixel always occupy one pixel in a DPIV image; thus, the true position of the particle cannot be resolved within a pixel. A small ratio of particle size to pixel size was inevitable in our experimental setup due to the large field of view required for the study.

Peak locking refers to the bias that occurs when the estimated location of the correlated peak is shifted towards the next integer value. Fincham and Spedding (1997) reported that peak locking will occur in any type of Image Velocimetry technique where sub-pixel determination of the correlation peak is attempted. Siddiqui et al. (2001) demonstrated that the three-point Gaussian estimator was the peak fitting scheme which caused the least amount of peak locking. Using Fincham and Delerce's (2000) method of determining peak locking, it was found that on average, 10 % of the streamwise velocity vectors and 18 % of the vertical velocity vectors were affected by peak locking (refer to Appendix). The vertical velocity vectors were more adversely affected by peak locking due to the smaller vertical velocities, resulting in a smaller dynamic range. The peak locking results are consistent with Fincham and Spedding's (1997).

The results of Cowen and Monismith (1997) and Prasad et al. (1992) were used to estimate the errors in the DPIV data. The mean values of the largest velocity gradients in the streamwise and vertical directions were computed from the raw DPIV data. Both the mean streamwise and mean vertical velocity gradients were 2 %. In

Figure 5(e) of Cowen and Monismith (1997) the approximate errors due to the velocity gradients are presented. The total error due to a mean 2 % gradient is estimated to be 0.06 pixels for a particle diameter of 2.0 pixels. Cowen and Monismith (1997) plot the errors as a function of the particle size; however, the smallest particle diameter presented in their analysis is 1.0 pixel. From Figure 5(a) (Cowen and Monismith, 1997) the error due to the velocity gradients is increased by 0.02 pixels when the particle diameter is lowered from 2.0 pixels to 1.0 pixel. Therefore, the total error due to a 2 % gradient for a particle diameter of 1.0 pixels is estimated to be 0.08 pixels.

The error corresponding to a particle diameter of 0.05 pixels was estimated using Figure 13 in Prasad et al. (1992), which shows the variation of the bias (peak locking) and RMS errors as a function of particle diameter. From this figure it is calculated that the errors associated with a particle diameter of 0.05 pixels are 40 % larger than the errors associated with a particle diameter of 1.0 pixels. The estimates of Prasad et al. (1992) were based on a center of mass peak-fitting scheme, which is the scheme most susceptible to peak locking errors (Fincham and Spedding, 1997). It is expected that the errors in the present case would be small since a three-point Gaussian estimator is much less susceptible to peak locking than the center of mass scheme (Cowen and Monismith, 1997). A more realistic estimate of the increase in errors due to small particle size is 20 %. Hence, the final error due to 2 % velocity gradients and a 0.05 pixels/pixel particle size is 0.096 pixels. Out of plane motion in the present case was assumed to be negligible. The error due to AGW interpolation was estimated from Figure 5(f) of Cowen and Monismith (1997) and was found to be 0.08 pixels.

The total error in the velocity can then be estimated as the error due to the velocity gradients, particle size, and AGW interpolation; $0.096 + 0.08 = 0.176$ pixels. This error expressed in velocity units is 0.06, 0.16, and 0.16 cm/s for Experiments 1, 2, and 3, respectively. Given the velocities encountered in Experiments 1, 2, and 3, the

experimental error in the instantaneous velocity would range from 1-6 %. An error of 6 % is the worst case scenario, when the velocities were extremely slow moving. Therefore, the average error in the instantaneous velocity field measurements was estimated to be 4 %.

The instantaneous flow rate was then obtained by integrating the measured instantaneous velocity profiles over the depth. The error in locating the free surface and the bottom positions increased the error in the estimates of the instantaneous flow rate. Due to the size of the search window in the PIV measurements, the first velocity measurement was located approximately 1 cm below the water surface. Therefore, to calculate the flow rate, from the water surface to the first data point, it was assumed that the velocity remained constant. Effects such as the surface tension may reduce the velocity at the water surface; however, these effects are negligibly small. The average flow rate for each experiment was then calculated by averaging the instantaneous flow rates over the entire steady period. We expect that using large sample sizes of 1800, 3600, and 2700, for Experiments 1, 2, and 3, respectively, eliminated the random error in our measurements. An error of approximately 3 % was estimated for the average flow rate based on replicate experiments.

The interface position images (640 x 480 pixels) had a field of view of approximately 45 cm (horizontal) by 33 cm (vertical). It was estimated that the in the determination of the interface position, errors of 2-3 pixels could occur, which corresponds to errors of 0.05 - 1 % in the interface position. Images of the interface position were collected every 1/5 s for Experiments 1, 2, and 3. Rhodamine dye dissolved in the lower layer made the position of the interface clearly visible in the interface position images. The presence of large-scale K-H instabilities located at the interface led to some ambiguity in the definition of the true interface position. That is, there was some uncertainty as to whether the position of the interface should be defined

as the top or bottom of the K-H instability. To alleviate any concerns that the interface position would be biased to either the upper or lower portion of the instability, an algorithm was developed that identified both the uppermost and the lowermost part of the instability. The average of the two values was used as the interface position. The instantaneous interface positions (collected every 1/5 s) were then averaged over the steady period, to obtain the mean interface position.

The thickness of the shear layer, δ , was calculated from the instantaneous velocity profiles. For each experiment, the velocity profiles were plotted for 16 to 19 instances in time. Then, from each acceptable velocity profile, the shear layer thickness was calculated (sometimes instabilities present at the interface prevented the shear layer thickness from being measured). This resulted in approximately 10 estimates of the shear layer thickness for every x location (see Appendix). These values were then averaged to obtain an estimate of the shear layer thickness. Values of the standard deviation were computed to be approximately 10 % of the shear layer thickness. Even though the measurement technique was quite crude, it will be demonstrated later that the measurements seem quite consistent for all experiments. Values of the shear layer thickness were also calculated using mean velocity profiles averaged over the steady period, δ^* . Differences between the measured values of δ and δ^* will be discussed in Section 5. The experimental error in the Richardson number is equal to the sum of the errors in δ and in ΔU^2 .

4.0 Hydraulics of the Flow

It is convenient to non-dimensionalize the flow variables with respect to the vertical scale, $H = 30$ cm, the lateral scale, $B = 10$ cm, the velocity scale, $(g'H)^{1/2}$, and the flow rate scale $H(g'H)^{1/2}$. The horizontal distance will be non-dimensionalized with respect to $\frac{1}{2}L_s$, where $L_s = 50$ cm is the length of the sill. This length scale was chosen so that $x = 0$ at the sill crest and $x = 1$ at the right-hand end of the sill. The characteristic time scale, T , for the experiments is equal to a length scale divided by the velocity scale. The length scale in T was chosen as $\frac{1}{2}L_s$ in order to remain consistent; giving $T = L_s/[2(g'H)^{1/2}]$. With these scales, the following set of dimensionless variables are obtained:

$$\begin{aligned} z_i^* &= z/H; \quad h^* = h/H; \quad x^* = x/(2L_s); \quad b^* = b/B; \quad E^* = E/H; \\ U_i^* &= U/(g'H)^{1/2}; \quad q_i^* = q/(H(g'H)^{1/2}); \quad t^* = t/T \end{aligned} \quad [24]$$

where the parameters with an asterisk are dimensionless. Unless otherwise indicated dimensionless parameters will be used for the remainder of this thesis, and the asterisks will be dropped.

The exchange flow commenced once the barrier in the rectangular channel was removed. Images taken from Experiment 2, which depict the gravity current moving forward, are presented in Figure 9. The denser salt water began to move forward into the slightly less dense fresh water, and gradually an unsteady flow was established. After the initial unsteady period, the hydraulic control at the sill crest was established, and at a later time the exit control was established. Exchange flow with two controls is called maximal exchange and is characterized by both a steady flow rate and mean interface position. A series of images which illustrate the flow over the sill during the steady periods of Experiments 1, 2, and 3 are presented in Figures 10, 11, and 12, respectively. These figures will be discussed more thoroughly in Section 5, where

interfacial instabilities will be discussed. The accumulation of fresh water in the left hand reservoir eventually flooded the exit control, and the flow returned to an unsteady state with only one hydraulic control at the sill crest (submaximal exchange). The evolution of flow regimes was studied in Zhu and Lawrence (2000).

In this study, we are primarily interested in the steady-state maximal exchange flow. Figures 13(a), 14(a), and 15(a) plot the measured instantaneous flow rate, q , over time for Experiments 1, 2, and 3, respectively; measured in the upper layer at the sill crest ($x=0$ cm). The flow rate was measured at a frequency of 1/5 s for Experiment 1 and 1/15 s for Experiments 2 and 3. The development of the three flow regimes can be seen in the flow rate versus time figures. First, there is an initial unsteady period where the flow increases to maximal exchange. Once both hydraulic controls are established (at the sill and at the exit), maximal exchange occurs and the flow remains steady for a period of time. Note that even during the steady period, the flow rate experienced large periodic fluctuations. These fluctuations and their cause will be discussed further in Section 5. The end of the steady period (maximal exchange) occurs once the exit control is flooded. The exchange flow then becomes submaximal, which is characterized by a decreasing flow rate.

For each experiment the instantaneous flow rates were averaged over their respective steady periods; resulting in a time-averaged flow rate, q , of 0.125, 0.126, and 0.122, at the sill crest for Experiments 1, 2, and 3, respectively. For such maximal exchange flows, the flow rate can be predicted using the control curve approach (Zhu, 2002) assuming that the flow is inviscid and hydrostatic. With two controls located at the sill crest and at the channel exit, and given the channel geometry in our experimental setup, a predicted q of 0.117 is predicted from the non-dimensional control curve plot in Figure 2. All three predicted flow rates compare well with the corresponding measurements made for each experiment at the sill crest with a difference of 7, 8, and

4 % for Experiments 1, 2, and 3, respectively (refer to Table 1). All measured values are greater than the predicted flow rate. The difference between the measured and predicted flow rate is likely due to the fact that the theoretical prediction neglects the effects of friction and streamline curvature. Including the effects of friction would tend to decrease predicted flow rate; however, Zhu and Lawrence (1998) demonstrated that including the effects of non-hydrostatic forces generated in flow over a sill may result in an increase in the predicted flow rate. Since the values of the measured flow rate are all greater than the predicted flow rate, this suggests that the effects of neglecting non-hydrostatic forces has a greater impact than neglecting the effects of friction. That is, the effect of neglecting non-hydrostatic forces is that the flow rate is underestimated even for exchange flows over smooth topography.

To the right of the sill crest, the flow becomes supercritical. The thickness of the lower layer continues to decrease away from the sill crest, and the composite Froude number G continues to increase. At the interface of the two layers, large-scale Kelvin-Helmholtz (K-H) instabilities grow and move downstream. These instabilities can be seen quite clearly in Figures 10, 11, and 12 and will be discussed further in Section 5.

In Figure 16, the measured mean interface positions (calculated as discussed in Section 3) for Experiments 1, 2, and 3 are compared to the theoretical prediction. The measured interface position did not vary significantly between Experiments 1, 2, and 3. This is consistent with the theory, which predicts that the interface position should remain constant when varying the reduced gravitational acceleration. Accurate determination of the interface position was crucial in the determination of G , since for supercritical flows, relatively small errors in the flow depth can lead to significant errors in G . The theoretical interface position was calculated using the condition that for maximal exchange flow $G = 1$ at the sill crest, and assuming the internal energy remains constant along the channel. The theory predicts the position of the interface quite

accurately at the sill crest; however, it underestimates it to the right of the sill crest. Zhu and Lawrence (2000) demonstrated that neglecting the effects of non-hydrostatic forces results in underestimating the interface position in supercritical regions. Therefore, the inclusion of non-hydrostatic forces might result in a more accurate prediction of the interface position to the right of the sill crest. As will be discussed later, there was a significant amount of entrainment observed along the sill, resulting in a large increase in flow rate. The varying flow rate would cause the internal energy, E , to vary along the sill. Recall that to calculate the prediction of the interface along the sill it was assumed that the internal energy remains constant. Thus, the fact that the flow rate varies along the sill may also contribute to the inaccurate prediction of the interface in the supercritical region.

The average velocity profiles in Experiments 1, 2, and 3 and the corresponding mean interface positions are plotted in Figures 17, 18, and 19, respectively. The density interface is the interface determined from the interface position images, while the velocity interface is located at the point where the velocity is equal to the average of the mean velocity in the upper and lower layers. It can be seen in Figures 17, 18, and 19 that the density interface is located below the velocity interface in all experiments. Therefore, in the upper layer, where the water is flowing right to left, a small zone of backflow exists where flow is actually moving left to right. As seen in Figures 17, 18, and 19, this zone of backflow increases down the sill. The flow rate along the sill was calculated by integrating the average velocity profiles from the water surface to the density interface. Since there was no net flow between the two layers, the flow rate calculated in the upper layer must be balanced by the flow rate in the lower layer.

The variation of the average flow rate along the sill for Experiments 1, 2 and 3 is plotted in Figure 20. In this figure, the flow rate at every x location was normalized by dividing it by the flow rate at the sill crest. It is evident that the flow rate increases along

the sill; this phenomenon will be discussed further in Section 5. Note that in calculating the instantaneous flow rates at the sill crest, plotted in Figure 12(a), 13(a), and 14(a), the backflow zone was neglected. Since the velocity and interface images were acquired from separate experiments, it was not possible to identify the interface at the exact instant that each instantaneous velocity profile was calculated. However, these instantaneous flow rates were calculated at the sill crest where the backflow zone is negligibly small. Neglecting the backflow zone at the sill crest caused the instantaneous flow rate to be overestimated by approximately 2 %.

The internal energy, E , (Equation [8]) was calculated using three different methods. Method I used both the predicted flow rate and the predicted interface position to calculate the internal energy. Method II used the predicted flow rate with the measured interface position, and finally, Method III used both the measured values of the flow rate and the interface position to calculate E . The internal energy values computed from Methods I, II, and III are plotted in Figure 21(a). Internal hydraulics (Method I) predicts a constant internal energy, E , of 0.65. When the measured interface position was used rather than the predicted interface (Method II), the internal energy no longer remained constant. In the supercritical region the internal energy decreased along the sill. For all three experiments; however, the internal energy calculated at each x location remains quite consistent using Method II. This is because the measured interface position remained constant for all experiments (as illustrated in Figure 16). As compared to the Method II, incorporating the increase in flow rate along the sill (Method III) had the effect of increasing the internal energy along the sill in the supercritical section. In other words, using both the measured flow rate and interface position, the loss of internal energy along the sill was less than when the predicted flow rate was used with the measured interface position.

The internal Froude number, G , was calculated along x in a similar manner as the internal energy. The same three methods were used, and the results for all three experimental conditions are plotted in Figure 21(b). From the measured data (Method III), the internal Froude number demonstrates that the flow is subcritical left of the sill crest, reaches critical at the sill crest, and is supercritical along the sill. All measured values of G are quite close to the theoretical value of 1.0 at the sill crest. In the supercritical region, the theory substantially overpredicts the internal Froude number. Again, this is likely due to the interface position being underestimated.

After a certain distance, the supercritical flow goes through a transition and becomes subcritical as controlled by the downstream flow condition. A series of images depicting the transition of the flow from supercritical to subcritical is presented in Figure 22. The images were taken 6 minutes and 20 seconds into the steady period of Experiment 4a ($g'=1.62 \text{ cm/s}^2$), and are separated by a time interval of 3 s. The lower layer is moving left to right and the upper layer is moving right to left. These images illustrate the growth of the mixed layer. As the flow in the lower layer moves downstream, the interfacial instabilities grow and eventually collapse. The transition of the supercritical flow to subcritical is dominated by these large-scale instabilities, quite different from open channel hydraulic jumps. After a certain length, the flow becomes uniform. Another interesting feature of this flow is that there was a stagnant fluid layer of intermediate density between the upper and lower layer, as reported by Wilkinson and Wood (1983), see Figure 22. This exchange flow is much different than open channel flow where the density difference across the air-water interface is large. Here, the density difference is quite small and so the inertia of the flow can overcome the buoyancy forces and we see large eddies forming between the two layers. The break down of these eddies causes entrainment of the upper layer into the lower layer, and thus, mixing between the two layers.

Downstream of the sill ($x \approx 3$) the mixed layer disappeared and the flow returned to a two-layer flow structure. The internal Froude number, G , was calculated at a few x locations at the right hand end of the channel to determine where the flow returned to a subcritical state. To calculate G in this portion of the channel, the interface was only collected once every 5 s over the duration of the steady period. In subcritical flows, the accuracy of the interface position is less crucial in determining G . Furthermore, the variations in the interface position were quite small at this location since no interfacial instabilities were observed here. The measured flow rate used in the G calculations was determined by integrating the upper layer of the velocity profiles from Experiment 4a. These velocity profiles are plotted in Figure 23. Note that the velocities in the lower layer were not reliable in this experiment due to the Rhodamine dye present in the lower layer (for flow visualization). As can be seen in Figure 23, velocity profiles were only available for $x < 2.5$, due to the field of view of the PIV camera. Therefore, a constant flow rate of 0.144 was assumed for $x > 2.5$. This assumption is valid since little variation existed in the flow rate at the downstream portion of the channel. From the internal Froude number calculations, the flow became uniform at approximately $x = 3.0$ with a value of G of 0.94.

Experiments 4b-d examined the effect of varying the height of a bottom weir on the flow. Bottom weir heights of 2.0, 4.5 and 9.0 cm were used for Experiments 4b, 4c, and 4d, respectively. As expected, it was observed that as the height of the weir increased, the interface level also increased. As the weir height increased, the mixing zone became flooded much more quickly.

5.0 Interfacial Instability and Entrainment

Downstream of the sill crest, in the supercritical section of the flow, the lower layer thickness decreases. As a result, the velocity in the lower layer and the interfacial shear between the two layers increases. The large interfacial shear between the two layers generates K-H instabilities at the interface, as depicted in Figures 10, 11, and 12. These figures demonstrate some very interesting features of the flow. The fluid seems to pile up near the sill crest causing the lower layer thickness to increase at the sill crest and decrease at the end of the sill. The piled up fluid is then released and the large interfacial shear causes the generation of K-H instabilities. Figures 10, 11, and 12, illustrate the fluid piling up and then being flushed down the sill. When comparing the figures, it is also evident that the K-H instabilities were much more coherent structures in Experiment 1 than in Experiment 3. The interface was also much more turbulent in Experiment 3 than it was in Experiment 1. Characteristics of the K-H instabilities in a spatially accelerating flow and the associated entrainment will be studied in this section.

5.1 Characteristics of the Interfacial Instabilities

The shear layer thicknesses, δ and δ^* are plotted in Figures 24(a) and (b) for all three experimental conditions. Recall that δ^* was measured from the time-averaged velocity profiles, while δ was measured from numerous instantaneous velocity profiles, and then averaged (see Appendix C). The values of δ^* measured from the averaged velocity profiles are approximately 2.5 to 3 times the size of the δ values measured from the instantaneous velocity profiles. This is because the average velocity profiles are so smoothed out that they cannot produce accurate predictions of the shear layer thickness. Therefore, accurate instantaneous velocity profile measurements are necessary to calculate δ because using average velocity profiles significantly

overestimates shear layer thickness values. Pawlak and Armi (2000) found shear layer thickness values ranging from 1 to 8 cm in their experiments. These values compare well with our δ^* measurements computed from the average velocity profiles, but not with our values computed from the instantaneous velocity profiles. Figure 24 demonstrates that the shear layer thickness did not vary significantly as g' was varied. However, for each experiment the δ values did increase down the sill. On average, shear layer thickness values ranged from 1.8 cm at the sill crest to 3 cm at the right hand end of the sill with standard deviations of 0.2 cm and 0.3 cm, respectively.

The shear layer Reynolds number, defined as

$$R_\theta = \frac{\Delta U \delta}{\nu} \quad [25]$$

where ν is the kinematic viscosity, is plotted in Figure 25(a) for Experiments 1, 2, and 3. Since the shear layer thickness and the kinematic viscosity remained essentially the same when varying the density difference, the Reynolds number calculated for Experiments 1, 2, and 3 really only varied as a function of the velocity difference between the upper and lower layer at any given x location. The Reynolds number calculations demonstrate that the flow was much more turbulent as g' was increased. This was also observed in the images presented in Figures 10, 11, and 12.

Values of the bulk Richardson number were calculated using δ , not δ^* , as the vertical scale. The results for all three experimental conditions are presented in Figure 25(b). Linear stability analysis predicts K-H instabilities are possible in the range $0.046 < R_i < 0.071$; but that Holmboe instabilities are the most unstable in that range (Haigh and Lawrence, 1999). Therefore, according to linear stability analysis, K-H instabilities are the most likely instabilities to develop only for the case where $R_i < 0.046$. Hogg and Ivey (2001) found the transition of K-H instability to Holmboe instability occurred at $R_i = 0.08$ for their experimental conditions. In our experimental observations; however, K-H

instabilities were observed for values of R_i as high as 0.10. This is most likely due to the high vertical acceleration of the flow as it moves down the sill. In their experiments, Pawlak and Armi (2000) found that K-H instabilities occurred for values of R_i ranging from 0.08 to 0.33.

As was illustrated in Figures 13(a), 14(a), and 15(a), the instantaneous flow rate experienced large periodic fluctuations. The spectrum of the flow rate time series data was computed for Experiments 1, 2, and 3, and the results are presented in Figures 13(b), 14(b), and 15(b), respectively. The dominant frequency of each spectrum corresponds to periods of 17.1, 16, and 14.4 s. These frequencies are associated with the K-H instabilities generated at the interface. Visual examination of the video confirmed that these instabilities were being generated approximately every 18, 15, and 13 s for Experiments 1, 2, and 3, respectively. Differences between the two values are likely due to the finite resolution of the computed frequency spectra. These spectral analysis results demonstrate that the K-H instabilities not only affect the position of the interface, but also significantly influence the instantaneous flow rate.

The first peak frequencies in Figures 13(b), 14(b), and 15(b) correspond to periods of 60, 48, and 36 s. These low frequency oscillations are believed to be associated with the basin internal seiche. As described by Zhu et al. (2001), an approximate estimate of the seiche period can be obtained by assuming the reservoir is a closed two-dimensional basin with a length $L_b = 123$ cm. The propagation speed of the interfacial wave is given by $C_i = \sqrt{g' z_1 z_2 / (z_1 + z_2)}$, and then the fundamental mode of the internal seiche has a period of $T_o = 2L_b / C_i$. Assuming the interface is at the mid-depth of the reservoir, i.e., $z_1 = z_2 = 15$ cm, the periods of the internal seiche are estimated to be 70, 50, and 35 s for Experiments 1, 2, and 3, respectively. Therefore, this simple model yields values for the basin internal seiche that compare well with the

measurements. Note that the actual seiche period will be affected by some factors that are not considered in this simple model: the effect of the connecting channel and the fact that the basin is close to rectangular (i.e.: three-dimensional).

Time series of the interface position at varying x locations for Experiments 1, 2, and 3 are plotted in Figures 26(a), 27(a), and 28(a), respectively. It is evident from these figures that as x increases, the fluctuations in the interface position become larger and shift to higher frequencies. The corresponding spectra of this data are plotted in Figures 26(b), 27(b), and 28(b). Again, we see that at the sill crest ($x = 0$ cm) the first peak frequency of the spectrum corresponds approximately to the fundamental basin oscillations with periods of 60, 45, and 36 s for Experiments 1, 2, and 3, respectively. Recall that the fundamental mode of the internal seiche was 70, 50, and 35 s when g' was varied from 1.62 to 3.23 to 6.47 cm/s². The second peak in the spectra at the sill crest corresponds to periods of 24, 15, and 14.4 s for Experiments 1, 2, and 3, respectively. Similar frequencies were observed in the spectra of the flow rate. Again, these periods correspond to the frequencies of occurrence of the K-H instabilities. The results of the spectral analysis for both the flow rate and interface position time series at the sill crest are presented in Table 2. Theoretical predictions of the basin internal seiche and to the observed frequency of the K-H instabilities for all three experimental conditions are also presented in Table 2. Differences between the periods computed from the flow rate and interface position time series are likely due to the finite resolution of the computed frequency spectra.

Figures 26(b), 27(b), and 28(b) illustrate how the spectra of the interface position varied down the sill. It is evident from these figures that as x increases, the spectral energy shifts to higher frequencies. This is due to the fact that K-H instabilities are being generated along the upstream portion of the sill. The spectral analysis demonstrates that at the sill crest, the K-H instabilities are generated approximately every 24, 15, and

14 s for Experiments 1, 2, and 3, respectively. Further downstream at any given x location, these instabilities will propagate past, but in addition, new K-H instabilities generated between the sill crest and x will also be observed. Therefore, the frequency of K-H instabilities that pass this location will be higher. And again, at some third location downstream of the second location all of the instabilities that passed through section two will pass through section three, along with new K-H instabilities that will be generated. The spectral analysis computations of the interface position for Experiments 1, 2, and 3 all reflect this pattern.

Experiment 3 (Figure 28) will be used to explain the variation of the interface position spectra down the sill. At $x = 0$, the peak that corresponds to the K-H instabilities is 0.0694 Hz (period of 14.4 s), while further downstream, at $x = 0.32$, a new frequency, 0.125 Hz (period of 8 s) is observed. Even further downstream, a new frequency, 0.182 Hz (period of 5.5 s) appears. The frequencies increase with x since K-H instabilities are generated down the length of the sill. This trend was observed until approximately $x = 0.48$, where the generation of instabilities seemed to stop. The spectra reflects this as the results from $x = 0.48$ to $x = 0.96$ are essentially the same, with no new peaks appearing. The effect of the basin oscillations also seems to diminish downstream of the sill crest. In fact, for Experiment 3, there is no spectral peak associated with the basin internal seiche at $x \geq 0.48$. The change in peak frequencies down the sill for Experiments 1, 2, and 3 are summarized in Tables 3, 4, and 5, respectively. The Tables show that similar trends as was described for Experiment 3 are observed in Experiments 1 and 2. As x increases, higher frequencies are observed. In fact when x is doubled and tripled, the new frequencies that appear are approximately double and triple the initial frequency. This is observed until $x = 0.48$ where K-H instabilities are no longer generated.

Time series of the interface position at different x locations were cross-correlated and the results for Experiments 1, 2, and 3 are presented in Tables 6, 7, and 8, respectively. The cross-correlation of the time series at different x locations resulted in a time lag between the two series. The time lag could then be converted to a velocity by multiplying it by Δx and dividing by the sampling frequency (1/5 s). The resulting velocity was an estimate of the speed at which the instabilities were traveling downstream. From Tables 6, 7, and 8, the results indicate that no time lag existed until $x = 0.41$. This is because the instabilities are being generated in this region of the sill. It is only at $x > 0.41$ that a time lag between the interface positions time series can be identified. Most of the instabilities have been created and are moving downstream in this region.

Theoretically, it is predicted that K-H instabilities will move downstream with the average of the mean velocity in the upper and lower layers. At every x location, this velocity was computed, and the results for Experiments 1, 2, and 3 are presented in Tables 6, 7, and 8, respectively. The results show that the K-H instabilities were moving down the sill at speeds much faster than the mean velocity. In fact, on average, they were traveling at speeds twice as fast as the mean velocity. It was believed that this could be a result of the density interface being shifted some distance lower than the velocity interface. To investigate this, the velocity at the density interface was determined from the velocity profiles in Figure 17, 18, and 19. The results are also presented in Tables 6, 7, and 8. The velocity of the interfacial instabilities computed from the cross-correlation of the interface position time series data is quite close to the values of the velocity determined at the density interface. This demonstrates that the location of the K-H instabilities relative to the velocity interface significantly affects the speed at which they travel.

The vorticity and turbulent kinetic energy fields were computed for Experiments 1, 2, and 3. Vorticity, given as

$$\omega = \frac{\partial w}{\partial x} - \frac{\partial u}{\partial z} \quad [26]$$

was calculated using the central difference method. The turbulent kinetic energy was computed using the formula

$$TKE = \frac{3}{4} (\overline{u'^2} + \overline{w'^2}) \quad [27]$$

where u' and w' are the turbulent components of the streamwise and vertical velocities, respectively. Note that this formula assumes $v'^2 = \frac{1}{2}(u'^2 + w'^2)$ since values of v' were not computed in the DPIV measurements. Also, the density term was left out so that TKE values are expressed per unit mass. A series of sample instantaneous vorticity fields and instantaneous turbulent kinetic energy fields computed from Experiment 3 are presented in Figures 29 and 30, respectively. The instantaneous velocity vector field is overlaid in each plot. One can actually see a K-H instability being generated, growing, and moving downstream in Figure 29.

The instantaneous vorticity fields and the instantaneous turbulent kinetic energy fields computed in Experiments 1, 2, and 3 were averaged over their respective steady periods. The results are presented in Figures 31, 32, and 33. It is interesting that in each experiment, the highest vorticity region is located at approximately $-0.2 < x < 0.6$. This is because most of the K-H instabilities are generated in this region. Recall that the spectral analysis results also indicated that the instabilities were generated in the region $0 < x < 0.48$. The turbulent kinetic energy is highest at approximately $0.4 < x < 1$. This is likely due to the collapse of the K-H instabilities in this region. Therefore, the results of the average vorticity and turbulent kinetic energy fields indicate that K-H instabilities are generated, move downstream and continuously grow in the region $-0.2 < x < 0.6$, and they become unstable and cause interfacial turbulence in the region $0.4 < x < 1$. This data is consistent with the spectral analysis data.

As the reduced gravitational acceleration was increased, the velocities observed in both the upper and lower layer and the interfacial shear between the two layers increased significantly. In fact, the instabilities observed at the interface were quite different as g' was varied. The K-H instabilities observed when g' was 1.62 cm/s^2 (Figure 10) were much more coherent than when g' was 6.47 cm/s^2 (Figure 12). The interface was much more turbulent and not quite as well defined in Experiment 3 as it was in Experiment 1. The average turbulent kinetic energy plots reflect this. From Figure 31(b), the average turbulent kinetic energy in Experiment 1 reached a maximum value of $3.5 \text{ cm}^2/\text{s}^2$, while in Experiments 2 and 3, the average turbulent kinetic energy reached maximum values of $5 \text{ cm}^2/\text{s}^2$ (Figure 32(b)) and $10 \text{ cm}^2/\text{s}^2$ (Figure 33(b)), respectively. This demonstrates that as g' was increased the flow was in fact much more turbulent. The shear Reynolds number (plotted in Figure 25(a)) also demonstrated that the flow was much more turbulent as the reduced gravitational acceleration was increased.

5.2 Entrainment

Large interfacial instabilities entrain fluid from the upper layer into the lower layer. To investigate the entrainment phenomenon, the variation of the flow rate in the upper layer, q_1 , along the sill was examined. As mentioned previously, the variation of the average flow rate for Experiments 1, 2 and 3 is plotted in Figure 20. In Experiment 1, q_1 increased from 0.117 at the sill crest to a maximum value of 0.144 near the end of the sill, corresponding to a 21.5 % increase in the flow rate. The increase in q_1 occurs because the lower layer entrains fluid along the sill. In other words, the flow rate in the upper layer is decreasing from the right-hand end of the sill towards the sill crest because fluid from the upper layer is being entrained into the lower layer. Similar trends

were observed for Experiments 2 and 3 where 19.9 % and 21.2 % increases in flow rate were observed, respectively.

Entrainment coefficients for Experiments 1, 2, and 3 were calculated using the formula

$$\alpha_e = \Delta q_1 / (\Delta x \cdot u_{2ave}), \quad [28]$$

where α_e is the entrainment coefficient, Δq_1 is the change in flow rate in the upper layer over a distance Δx , and u_{2ave} is the average velocity in the lower layer. The average velocity in the lower layer, u_{2ave} , was calculated by dividing the mean flow rate computed in the upper layer by the average lower layer thickness. In doing so, it was assumed that the mean flow rate in upper layer was balanced by the mean flow rate in lower layer. This assumption is valid since no net flow existed between the two layers. The variation of the entrainment coefficient across the sill is illustrated in Figure 35(b). In Experiment 1 values for the entrainment coefficient reached a maximum of 0.089 at $x = 0.21$. As g' was increased, the x location of maximum entrainment moved down the sill, and the maximum value of the entrainment coefficient decreased. For Experiments 2 and 3, the entrainment coefficient reached a maximum value of 0.070 at $x = 0.35$, and 0.066 at $x = 0.64$. Note that even though similar increases in flow rate were observed for Experiments 1, 2, and 3 along the sill (approximately 20 %), the entrainment rate decreased as g' was increased because of the differing values of u_{2ave} .

Many studies have tried to relate entrainment rates to the bulk Richardson number. In order to compare our entrainment coefficient values with the results from the literature, the bulk Richardson number was defined as $R_i^* = g'z_2/\Delta U^2$ where z_2 is the lower layer thickness, in this sub-section. Values of R_i^* are plotted in Figure 35(a) for all Experiments 1, 2, and 3. The bulk Richardson number is quite high at the sill crest with values of approximately 0.3 for all three experiments, and decreases to approximately

0.15 at the right-hand end of the sill. It is expected that the bulk Richardson number will decrease down the sill, since the lower layer thickness decreases down the sill and the velocity difference between the upper and lower layer increases down the sill.

Using this bulk Richardson number the entrainment coefficient expected for gravity currents was calculated using Parker et al.'s (1987) formula (Equation 23). The results are also plotted in Figure 35(b). We see that based on their relationship, we would expect entrainment coefficients to range from 0.01 to 0.03; however, our experimental results demonstrate that the entrainment coefficients were much higher. This demonstrates how different spatially accelerating exchange flow is from previously studied gravity currents. The large interfacial shear between the layers and the K-H instabilities significantly impact the mixing. One could also compare the entrainment coefficients calculated for Experiments 1, 2, and 3 with the entrainment coefficient of 0.035 for a plane turbulent wall jet (Rajaratnam, 1976). Again, we see that the entrainment in exchange flows is significantly larger than what is predicted for a plane turbulent wall jet. Many have thought that the stable density stratification would reduce the amount of entrainment; however, this is not what we observed. The large amount of interfacial shear in an exchange flow is a major source of mixing at the stratified interface.

6.0 Conclusions

A detailed experimental study of the hydraulics of exchange flows and the interfacial mixing was presented. Experimental results describing the hydraulics of exchange flows were discussed first and the evolution of flow regimes (sub-maximal and maximal exchange) was examined. High frequency instantaneous measurements enabled us to observe large periodic fluctuations in the flow rate, even during the steady period. Measured values of the flow rate, interface position, internal Froude number, and internal energy were compared with the predictions calculated using internal hydraulic theory. It was found that the flow rate is well predicted at the sill crest; however, entrainment of the upper layer into the lower layer increases the flow rate in the supercritical region of the flow to values well above the predicted flow rate. Likewise, the interface position, the internal energy and the internal Froude number are all predicted well at the sill crest, but not in the supercritical regions of the flow. The transition of the supercritical flow to subcritical was dominated by large-scale instabilities, quite different from open channel hydraulic jumps.

Large-scale K-H instabilities were observed on the downstream side of the sill where the flow was supercritical and the interfacial shear was strong. These instabilities continuously grew and eventually broke down which then led to the transition from supercritical to subcritical flow. It was found that using average velocity profiles to compute the shear layer thickness significantly overestimated the values of δ . Linear stability analysis predicts that K-H instabilities are the most unstable in the range $R_i < 0.046$; however, we observed the generation of K-H instabilities for values of the bulk Richardson number as high as 0.1. This is likely due to the high vertical acceleration of the flow as it moves down the sill.

Spectral analysis was used to demonstrate that fluctuations in the interface position and the flow rate were caused not only by basin-scale internal seiches, but most importantly by K-H instabilities generated at the interface. It was also found that as x increases, the spectral energy shifted to higher frequencies since K-H instabilities are generated down the upstream two thirds of the sill. The results of the spectral analysis indicated that instabilities were not generated downstream of approximately $x = 0.48$. The vorticity and turbulent kinetic energy calculations were consistent with the spectral analysis data and demonstrated that K-H instabilities are generated and move downstream in the region $-0.2 < x < 0.6$, and they are broken down and cause interfacial turbulence in the region $0.4 < x < 1$. Cross-correlation of the interface position time series at different locations was used to compute the speed at which the K-H instabilities traveled down the sill. On average, they were traveling at speeds twice as fast as the depth-averaged (predicted) velocity. It was demonstrated that the K-H instabilities traveled at speeds approximately equal to the velocity at the density interface. Thus, the fact that the density interface was shifted lower than the velocity interface had a significant impact on the speed at which the K-H instabilities traveled.

It was also found that the interfacial instabilities entrained fluid from the upper layer into the lower layer. The maximum entrainment coefficients for Experiment 1, 2, and 3 were found to be 0.089, 0.070, and 0.066, respectively. These values are considerably larger than the entrainment coefficients found for plane turbulent wall jets and gravity currents. The large amount of interfacial shear in an exchange flow is a major source of mixing at the stratified interface. The entrainment increased the flow rate in the upper layer by approximately 22 % downstream of the sill compared to that at the sill crest.

7.0 References

- Agüí, J.C. and Jiménez, J. 1987 On the performance of particle tracking. *J. Fluid Mech.* **185**, 447-468.
- Alavian, V., Jirka, G.H., Denton, R.A., Johnson, M.C. and Stefan, H.G. 1992 Density currents entering lakes and reservoirs. *J. Hydraulic Engng.* **118**, 1464-1487.
- Armi, L. and Farmer, D.M. 1988 The flow of Mediterranean water through the Strait of Gibraltar. *Progress in Oceanography* **21**, 1-105.
- Baines, P.G. 1984 A unified description of two-layer flow over topography. *J. Fluid Mech.* **146**, 127.
- Browand, F.K. and Wang, Y.H. 1972 An experiment on the growth of small disturbances at the interface between two streams of different densities and velocities. *Proceedings of the International Symposium on stratified flows*, pp 491-498. Novosibirsk, USSR: ASCE.
- Cowen, E.A., and Monismith, S.G. 1997 A hybrid digital particle tracking velocimetry technique. *Exp. Fluids* **22**, 199-211.
- Denton, R.A. 1987 Locating and identifying hydraulic controls for layered flow through an obstruction. *J. Hydraul. Research* **25**, 281-299.
- Ellison, T. H and Turner, J. S. 1959 Turbulent entrainment in stratified flows. *J. Fluid Mech.* **6**, 423-448.
- Farmer, D. and Armi, L. 1986 Maximal two-layer exchange over a sill and through the combination of a sill and contraction with barotropic flow. *J. Fluid Mech.* **164**: 53-76.
- Farmer, D. and Armi, L. 1999 Stratified flow over topography: the role of small scale entrainment and mixing in flow establishment. *Proc. Roy. Soc. Lond. A* **455**, 3221-3258.

- Fincham, A.M. and Delerce, G. 2000 Advanced optimization of correlation imaging velocimetry algorithms. *Exp. Fluids [Suppl.]*, S13-S22.
- Fincham, A.M. and Spedding, G.R. 1997 Low cost, high resolution DPIV for measurement of turbulent fluid flow. *Exp. Fluids* **23**, 449-462.
- Goldstein, S. 1931 On the stability of superimposed streams of fluids of different densities. *Proc. Roy. Soc. Lond. A* **132**, 524-548.
- Haigh, S.P., and Lawrence, G. A. 1999 Symmetric and nonsymmetric instabilities in an inviscid flow. *Phys. Fluids* **11**, 1459-1468.
- Hamblin, P.F. and Lawrence, G.A. 1990 Exchange flows between Hamilton Harbour and Lake Ontario, *Proc. of 1990 Annual Conf. of Canadian Society for Civil Eng.*, V: 140-148.
- Hazel, P. 1972 Numerical Studies of the stability of inviscid stratified shear flows. *J. Fluid Mech.* **51**, 39-61.
- Hogg, A. and Ivey, G. 2001 The Kelvin-Helmholtz to Holmboe instability transition in stratified exchange flows. *J. Fluid Mech.* in press.
- Holmboe, J. 1962 On the behavior of symmetric waves in stratified shear layers, *Geofysiske Publikasjoner* **24**, 67-113.
- Koop, C. G. and Browand, F. K. 1979 Instability and turbulence in a stratified fluid with shear. *J. Fluid Mech.* **93**, 135-159.
- Lawrence, G. A. 1990 On the hydraulics of Boussinesq and non-Boussinesq two-layer flows. *J. Fluid Mech.* **215**, 457-480.
- Lawrence, G. A. 1993 The hydraulics of steady two-layer flow over a fixed obstacle. *J. Fluid Mech.* **254**, 605-633.
- Lawrence, G.A, Browand, F.K. and Redekopp, L.G. 1991 The stability of a sheared density interface. *Phys. Fluids* **3**, 2360-2370.

- Long, R.R. 1954 Some aspects of the flow of stratified fluids. II. Experiments with a two-fluid system. *Tellus* **6**, 97.
- Marxen, M. 1998 Particle Image Velocimetry in Stromugen mit starken Geschwindigkeitsgradienten, Diplom Thesis, Fakultat fur Physik und Astronomie, Ruprecht-Karls-Universitat Heidelberg.
- Parker, G., Garcia, M., Fukushima, M and Yu, W. 1987 Experiments on turbidity currents over an erodable bed. *J. Hydraul. Research* **25**, 123-147.
- Pawlak, G. and Armi, L. 1998 Vortex dynamics in a spatially accelerating shear layer. *J.Fluid Mech.* **376**, 1-35.
- Pawlak, G. and Armi, L. 2000 Mixing and entrainment in developing stratified currents. *J.Fluid Mech.* **424**, 45-73.
- Prasad, A.K, Adrian, R.J., Landreth, C.C., and Offutt, P.W. 1992 Effect of resolution on the speed and accuracy of particle image velocimetry interrogation. *Exp. Fluids* **13**, 105-116.
- Rajaratnam, N. 1976 Turbulent Jets. Elsevier Publishing Co., Amsterdam and New York, 1976, 304 pages.
- Roshko, A. 1976 Structure of turbulent shear flows: A new look. *AIAA J.* **14** (10), 1349-1357.
- Schiff, J. B. and Schonfeld, J.C. 1953 Theoretical considerations on the motion of salt and fresh water. *Proc. Minnestoa Int. Hydraulics Conference*, Joint meeting IAHR and Hyd. Div., ASCE, September 1953, 321-330.
- Siddiqui, M.H.K., Loewen, M.R., Richardson, C., Asher, W.E., Jessup, A.T. 2001 Simultaneous particle image velocimetry and infrared imagery of microscale breaking waves. *Physics of Fluids* **13**, 1891-1903.
- Thorpe, S.A. 1968 A method of producing shear flow in a stratified fluid. *J. Fluid Mech.* **32**, 693-704.

- Thorpe, S.A. 1971 Experiments on the instability of stratified shear flows: miscible fluids. *J. Fluid Mech.* **46**, 299-319.
- Thorpe, S.A. 1973 Experiments on instability and turbulence in a stratified shear flow. *J. Fluid Mech.* **61**, 731-751.
- Taylor, G.I. 1931 Effect of variation in density on the stability of superimposed streams. *Proc. Roy. Soc. Lond. A* **132**, 499-523.
- Westerweel, J. 1994 Efficient detection of spurious vectors in particle image velocimetry data. *Exp. Fluids* **16**, 236.
- Wilkinson, D.R. and Wood, I.R. 1983 The formation of an intermediate layer by horizontal convection in a two-layer shear flow. *J. Fluid Mech.* **136**, 167-187.
- Zhu, D.Z. 2002 Control curves of two-layer flows. *J. Hydraulic Engng.* **128** (1).
- Zhu, D.Z., Fouli, H. and Okyere, Y.A. 2001 Exchange flow through an opening. *J. Hydraul. Research* in press.
- Zhu, D.Z. and Lawrence, G.A 1998 Non-hydrostatic effects in layered shallow water flows. *J. Fluid Mech.* **355**, 1-16.
- Zhu, D.Z. and Lawrence, G.A 2000 Hydraulics of exchange flows. *J. Hydraulic Engng.* **126** (12), 921-928.
- Zhu, D.Z. and Lawrence, G.A 2001 Holmboe instabilities in exchange flows, *J. Fluid Mech.* **429**, 391-409.

Table 1: List of experiments.

Experiment	Weir Height (cm)	Water Temp. (°C)	g' (cm/s ²)	Measured Flow Rate q_m^* (cm ² /s)	Predicted Flow Rate q_p (cm ² /s)	$(q_m - q_p)/q_p$ (%)	Time Scale T^{**}
1	0	14.7	1.62	0.125***	0.117	7	3.59
2	0	16.0	3.23	0.126	0.117	8	2.54
3	0	16.7	6.47	0.122	0.117	4	1.79
4a	0	7	1.62	—	—	—	3.59
4b	2	9	1.62	—	—	—	3.59
4c	4.5	10	1.62	—	—	—	3.59
4d	9	8.5	1.62	—	—	—	3.59

Sill crest height, $h_s = 10$ cm, and water depth, $H = 30$ cm for all experiments.

* q_m measured at the sill crest

** non-dimensional time scale, $T = L/(g'H)^{1/2}$ where L is the half length of the sill

*** $q_m = 0.125 \pm 3\%$, experiment repeated 3 times

Table 2: Results of the spectral analysis computed at the sill crest for both the flow rate and interface data. All data are in seconds.

	Theoretical Period of the Basin Internal Seiche	Observed Period of K-H Instabilities at Sill Crest from Video Recordings	Spectrum of Flow Rate		Spectrum of Interface	
			1 st Peak	2 nd Peak	1 st Peak	2 nd Peak
Experiment 1	70	18	60	17.1	60	24
Experiment 2	50	15	48	16	45	15
Experiment 3	35	13	36	14.4	36	14.4

Table 3: Frequencies (Hz) determined from the spectra of the interface position at varying x locations for Experiment 1. Spectral resolution $\Delta f = 0.0083$ Hz.

	$x=0$	$x=0.16$	$x=0.32$	$x=0.48$	$x=0.64$	$x=0.80$	$x=0.96$
f_0 basin internal sieche	0.0166	–	0.0166	0.0166	0.0166	0.0166	0.0166
f_1 K-H instability first peak	0.0417	0.0333	0.0333	0.0416	0.0416	0.0416	0.0416
f_2 K-H instability second peak				0.0666	0.0666	0.0666	–
f_3 K-H instability third peak				0.125	0.125	0.125	0.1333

Table 4: Frequencies (Hz) determined from the spectra of the interface position at varying x locations for Experiment 2. Spectral resolution $\Delta f = 0.0111$ Hz.

	$x=0$	$x=0.16$	$x=0.32$	$x=0.48$	$x=0.64$	$x=0.80$	$x=0.96$
f_0 basin internal sieche	0.0222	0.0222	0.0333	–	0.0333	–	–
f_1 K-H instability first peak	0.0666	0.0666	0.0666	0.0666	0.0666	0.0666	0.0666
f_2 K-H instability second peak			0.1	0.1222	0.1	0.1	0.1
f_3 K-H instability third peak					0.1666	0.1666	0.1666

Table 5: Frequencies (Hz) determined from the spectra of the interface position at varying x locations for Experiment 3. Spectral resolution $\Delta f = 0.0139$ Hz.

	$x=0$	$x=0.16$	$x=0.32$	$x=0.48$	$x=0.64$	$x=0.80$	$x=0.96$
f_0 basin internal sieche	0.0278	0.0278	0.0278	–	–	–	–
f_1 K-H instability first peak	0.0694	0.0694	0.0833	0.0972	–	–	–
f_2 K-H instability second peak			0.125	0.125	0.125	0.125	0.125
f_3 K-H instability third peak				0.1806	0.1806	0.1806	0.1944

Table 6: Comparison of the velocity computed from the cross-correlation of the interface position to the depth averaged velocity and the velocity at the density interface at varying x locations for Experiment 1.

x	total depth-averaged velocity (cm/s)	velocity at density interface (cm/s)	correlation coefficient	shift of interface position	shift of interface position in velocity units (cm/s)
0.00	0.48				
0.08	0.73	1.43	0.67	0	0
0.19	0.96	1.57	0.63	0	0
0.30	0.99	1.93	0.61	0	0
0.42	1.08	2.18	0.61	4.5	2.90
0.52	1.13	2.38	0.58	5	2.69
0.64	1.16	3.11	0.57	5	2.61
0.74	1.16	3.19	0.50	5	2.69
0.86	-*	3.32	0.48	4	3.27
0.96	-*	-*	0.44	4	3.36

* note that these points were left out because the PIV did not capture the maximum velocity

Table 7: Comparison of the velocity computed from the cross-correlation of the interface position to the depth averaged velocity and the velocity at the density interface at varying x locations for Experiment 2.

x	total depth-averaged velocity (cm/s)	velocity at density interface (cm/s)	correlation coefficient	shift of interface position	shift of interface position in velocity units (cm/s)
0.00	0.89	1.83			
0.10	1.22	2.35	0.51	0	0
0.21	1.51	2.98	0.65	0	0
0.31	1.64	3.74	0.61	0	0
0.41	1.81	4.23	0.60	3.5	3.92
0.52	1.92	4.95	0.63	4	3.33
0.62	2.04	5.30	0.63	3	4.44
0.72	2.18	5.30	0.63	3	4.44
0.83	2.31	5.32	0.62	3	4.44
0.93	2.45	4.70	0.60	2.5	5.33

Table 8: Comparison of the velocity computed from the cross-correlation of the interface position to the depth averaged velocity and the velocity at the density interface at varying x locations for Experiment 3.

x	total depth-averaged velocity (cm/s)	velocity at density interface (cm/s)	correlation coefficient	shift of interface position	shift of interface position in velocity units (cm/s)
0.00	1.30	3.80			
0.11	1.91	3.71	0.70	0	0
0.21	2.27	4.92	0.67	0	0
0.32	2.39	5.34	0.59	0	0
0.42	2.57	5.31	0.57	2.5	5.40
0.53	2.65	5.00	0.58	2.5	5.26
0.64	2.88	5.31	0.58	2.5	5.40
0.74	3.00	5.26	0.61	2.5	5.26
0.85	3.17	6.11	0.61	2	6.75
0.96	3.33	6.20	0.58	2	6.75

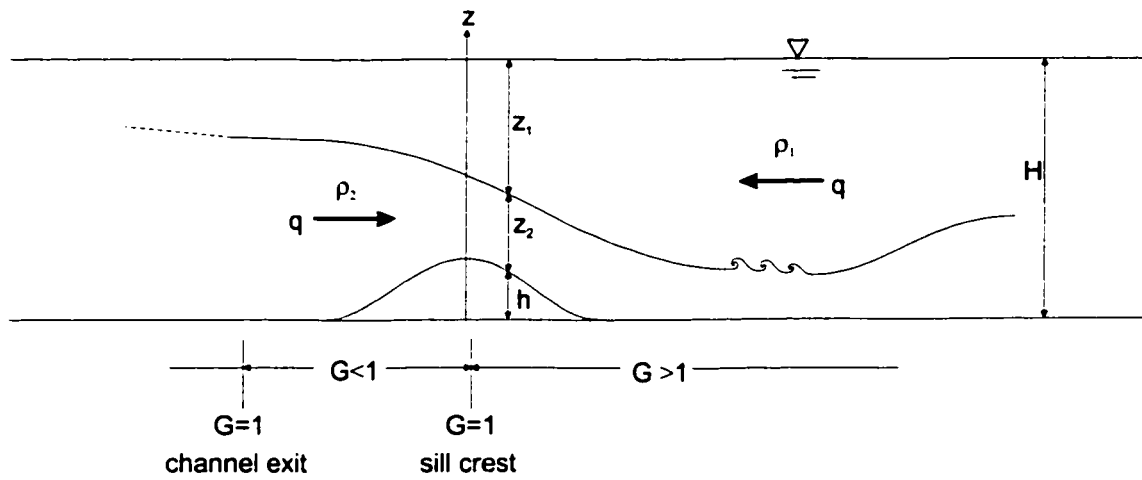


Figure 1: Two-layer maximal exchange flow over a smooth sill.

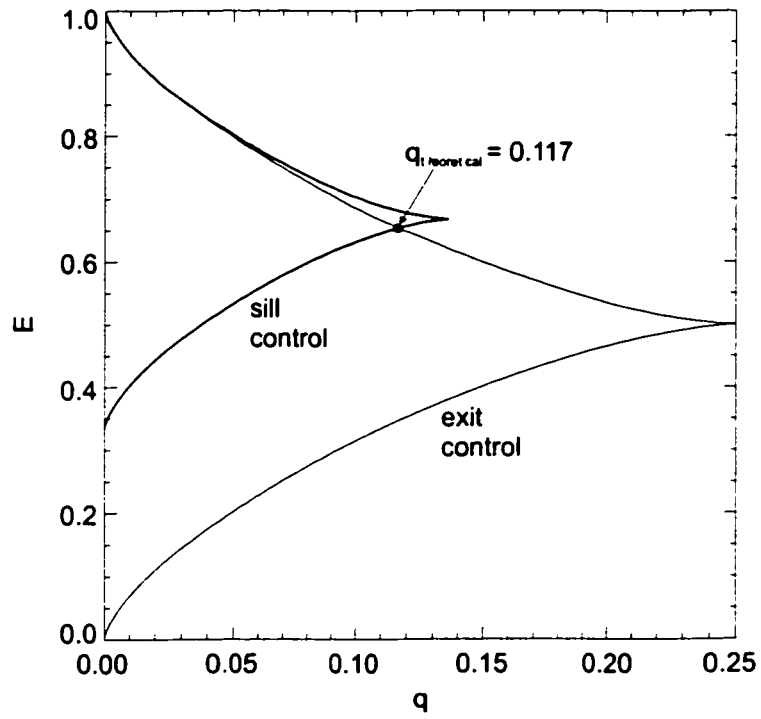


Figure 2: Non-dimensional control curve plots.

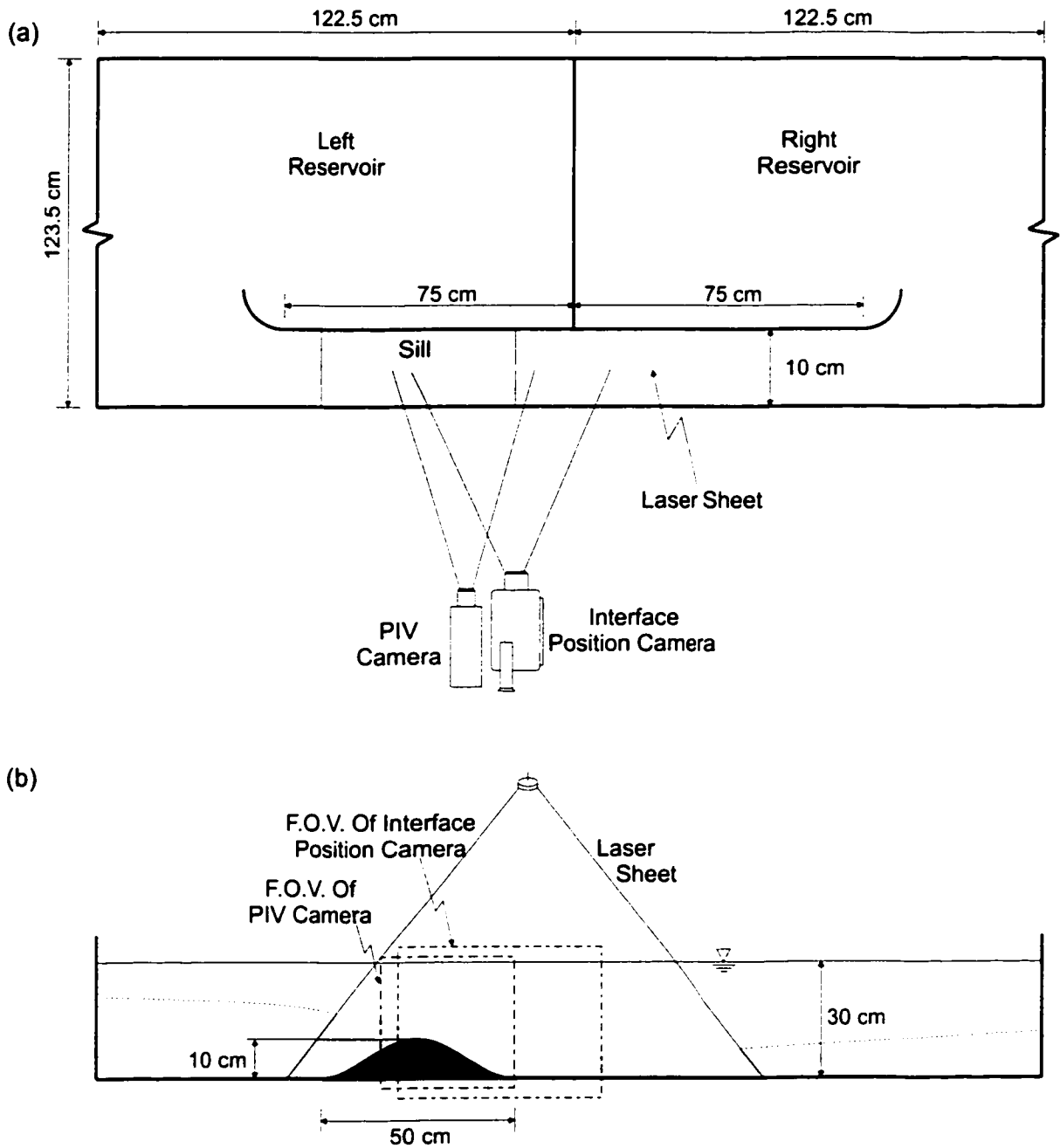


Figure 3: Experimental setup and instrumentation: (a) plan view, (b) side view.

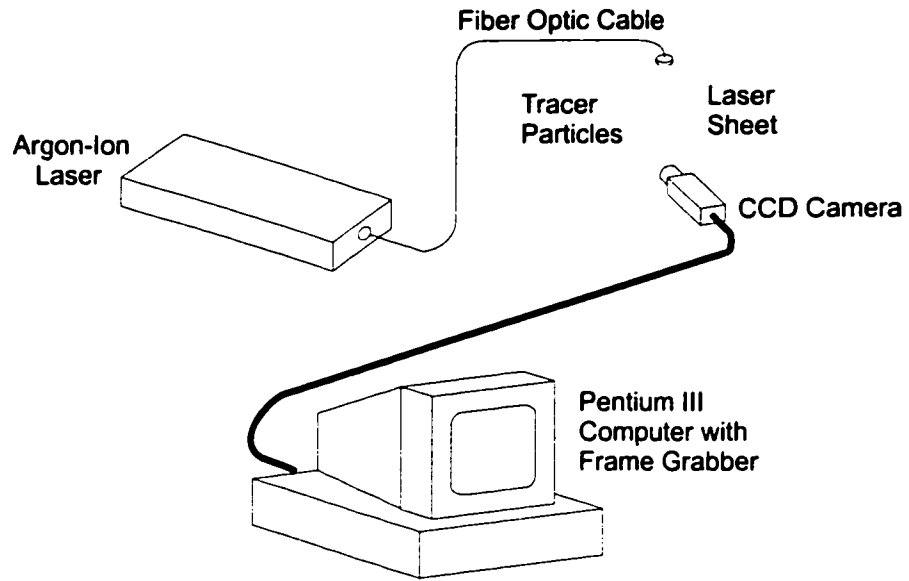


Figure 5: Schematic of particle image velocimetry experimental setup.

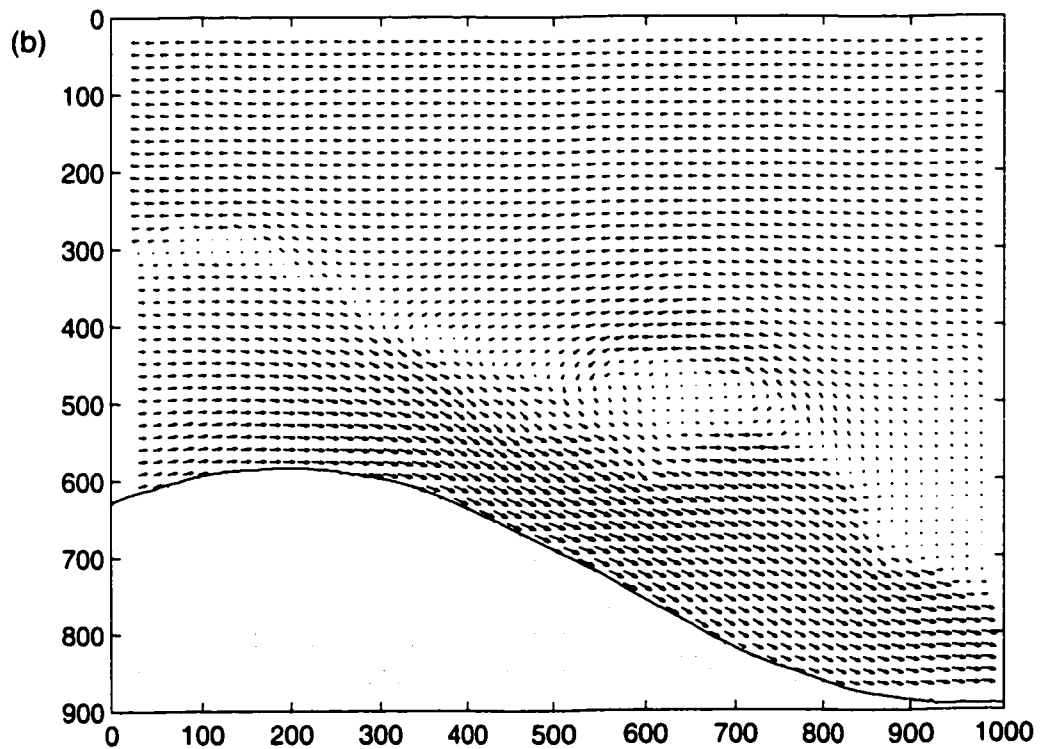
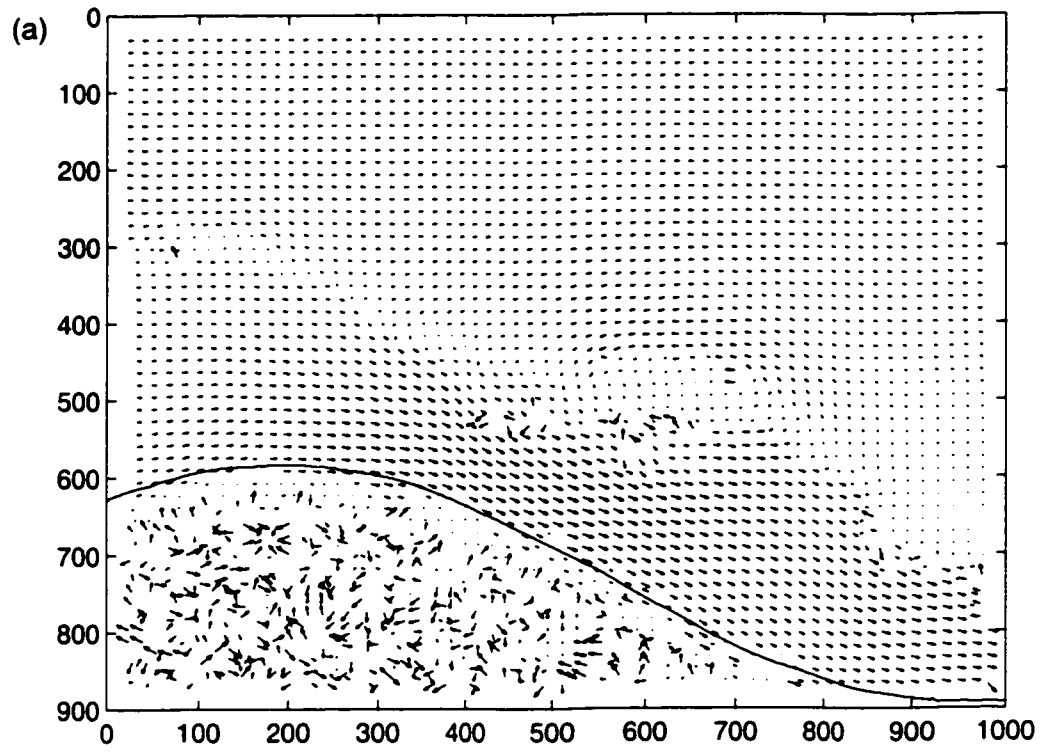


Figure 7: (a) Sample raw velocity vector field, (b) the corresponding corrected and interpolated velocity vector field. Velocity fields taken from Experiment 3.



Figure 8: Sample interface position image taken from Experiment 1.

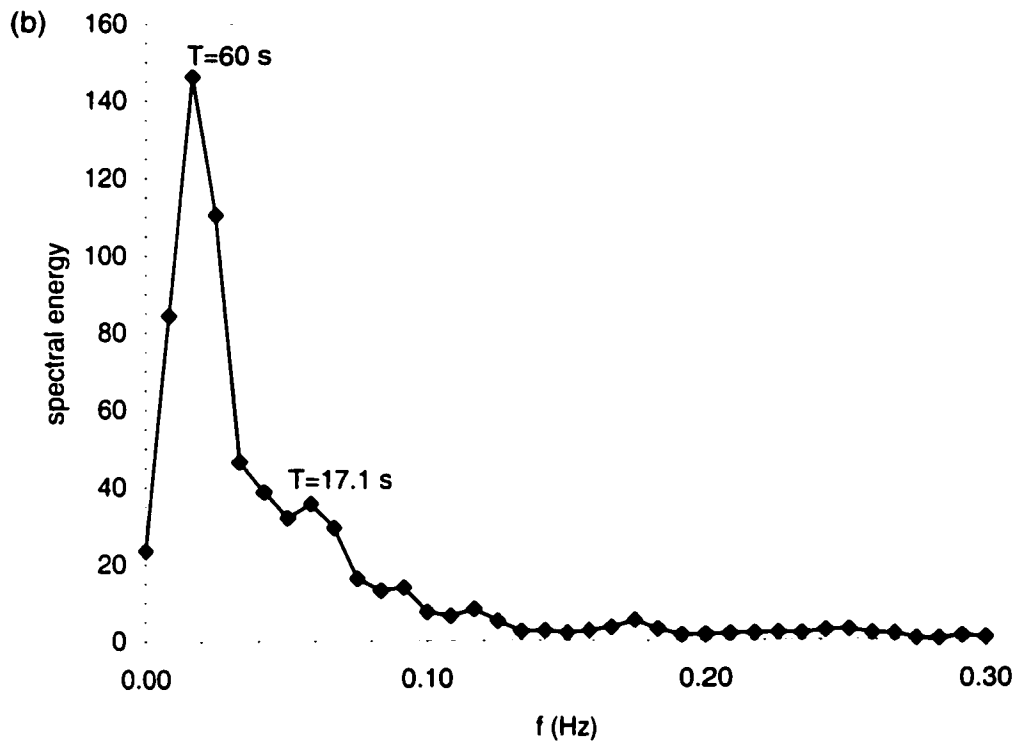
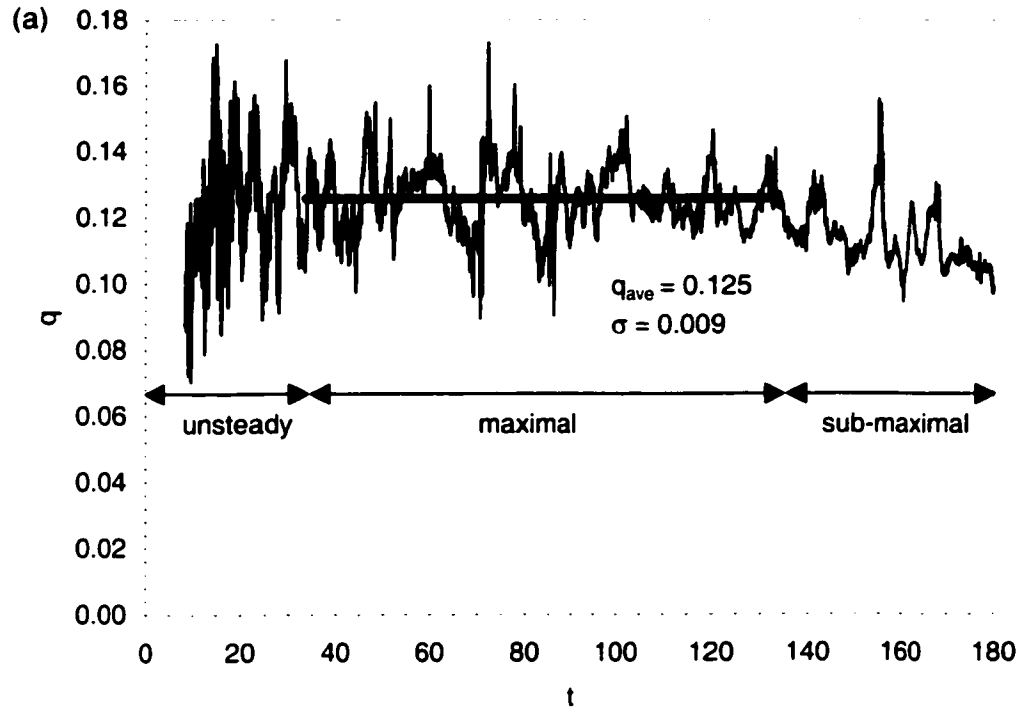


Figure 13: Flow rate measured in the upper layer at the sill crest ($x=0$ cm) for Experiment 1, (b) spectrum of the flow rate (spectral resolution $\Delta f = 0.0083$ Hz).

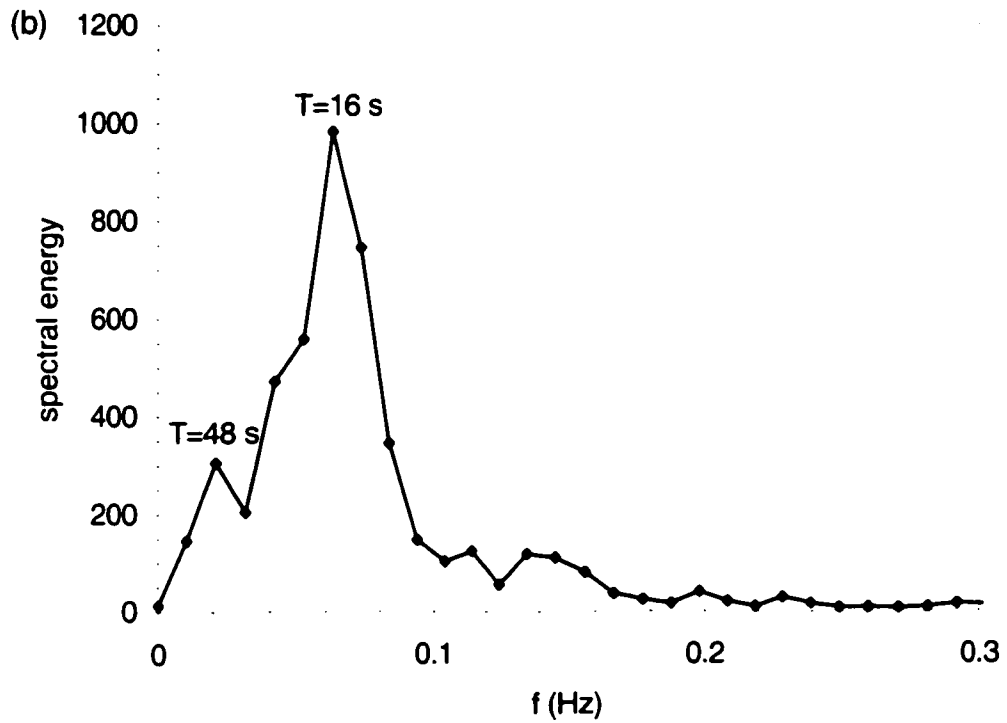
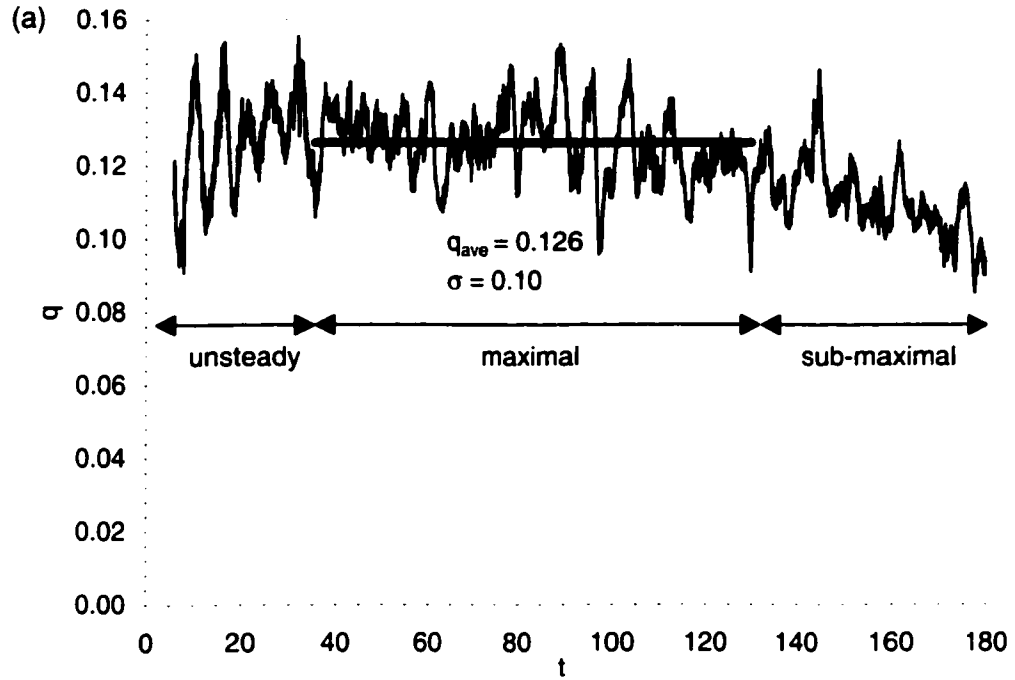


Figure 14: Flow rate measured in the upper layer at the sill crest ($x=0$ cm) for Experiment 2, (b) spectrum of the flow rate (spectral resolution $\Delta f = 0.0104$ Hz).

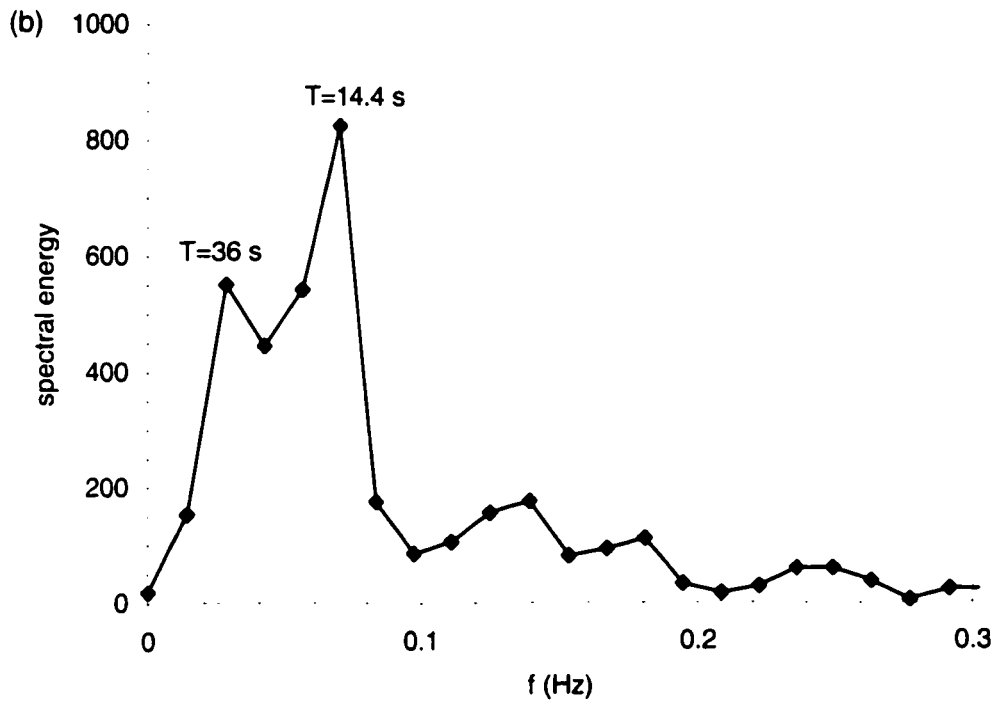
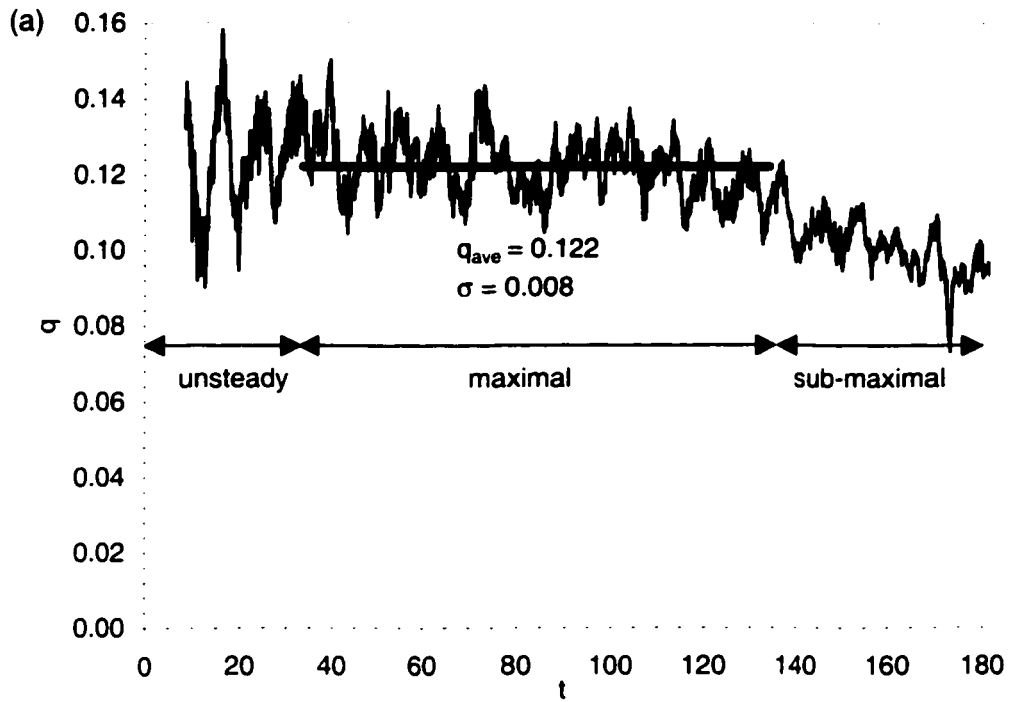


Figure 15: Flow rate measured in the upper layer at the sill crest ($x=0$ cm) for Experiment 3, (b) spectrum of the flow rate (spectral resolution $\Delta f = 0.0139$ Hz).

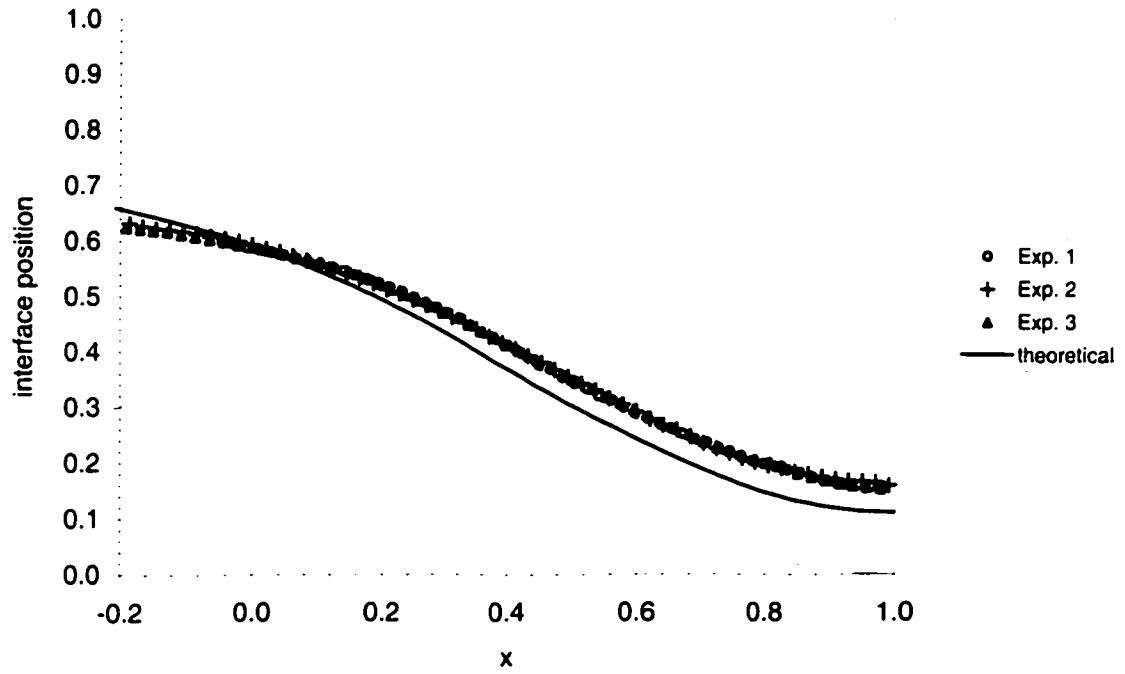


Figure 16: Mean interface position of Experiments 1, 2, and 3 measured along the sill compared to the theoretical interface prediction.

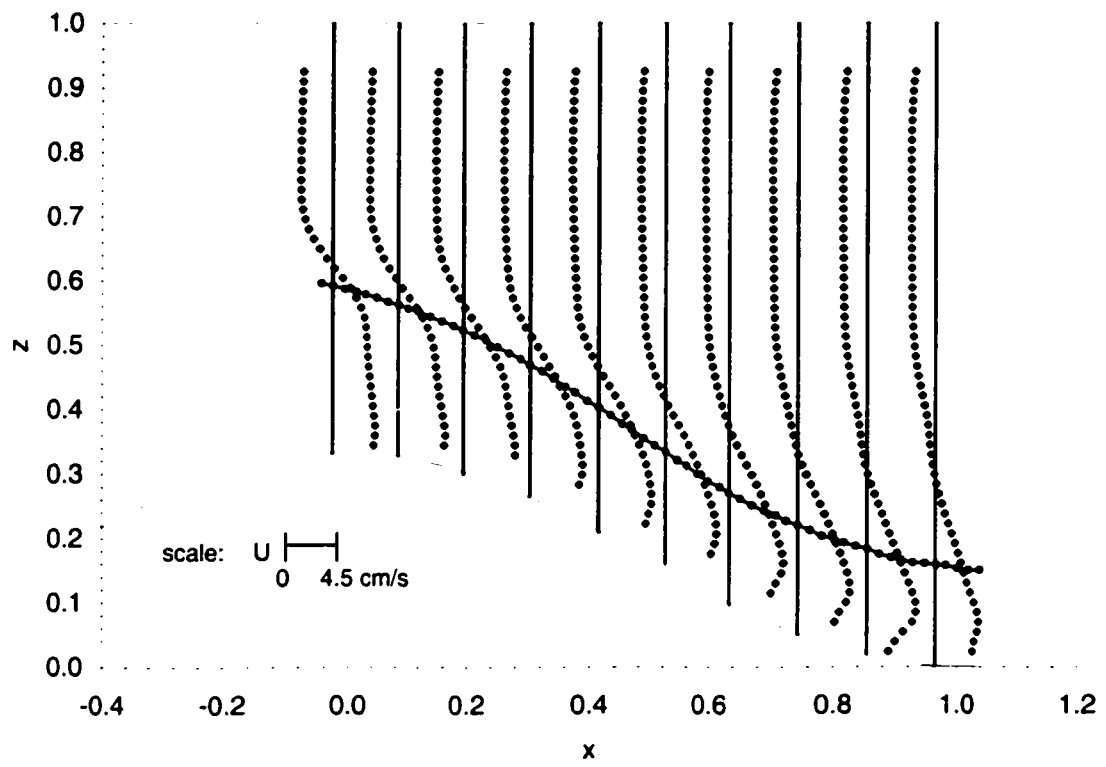


Figure 17: Average velocity profiles for Experiment 1 showing mean interface position.

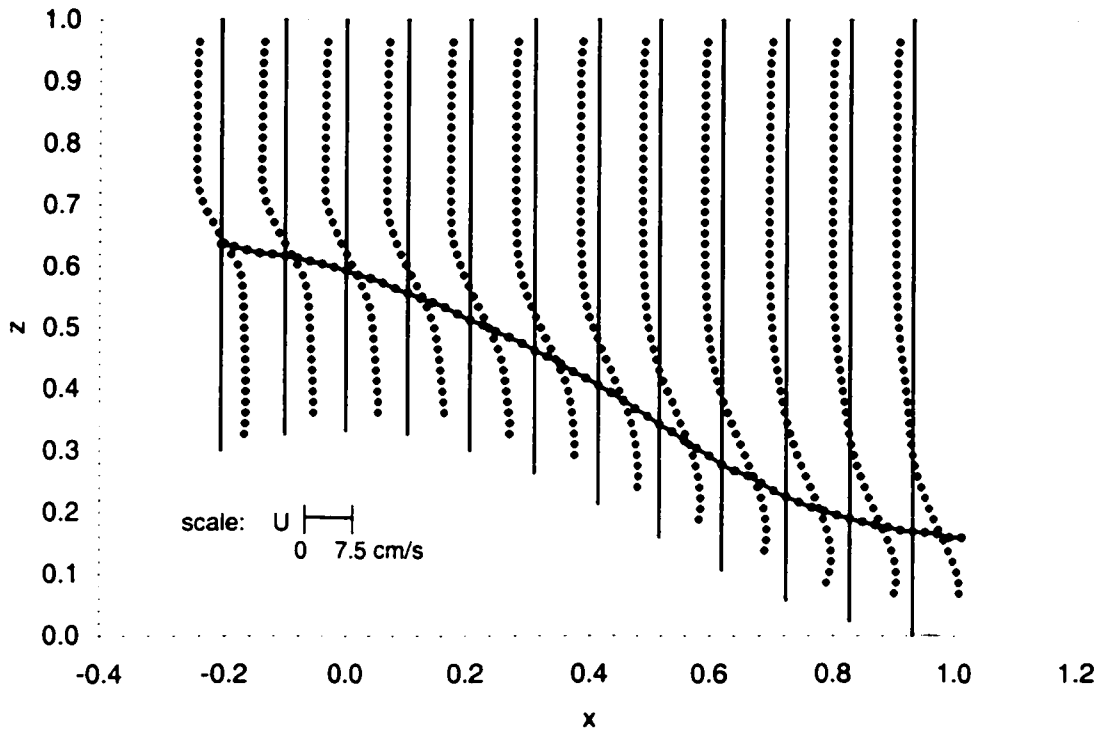


Figure 18: Average velocity profiles for Experiment 2 showing mean interface position.

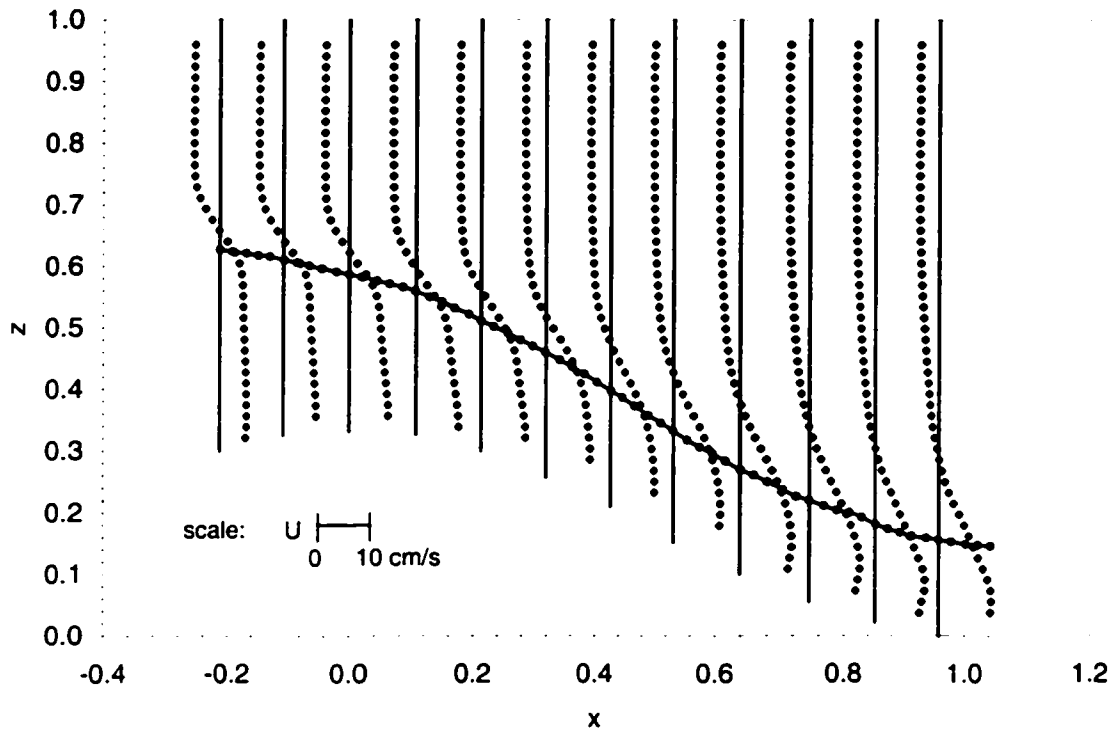


Figure 19: Average velocity profiles for Experiment 3 showing mean interface position.

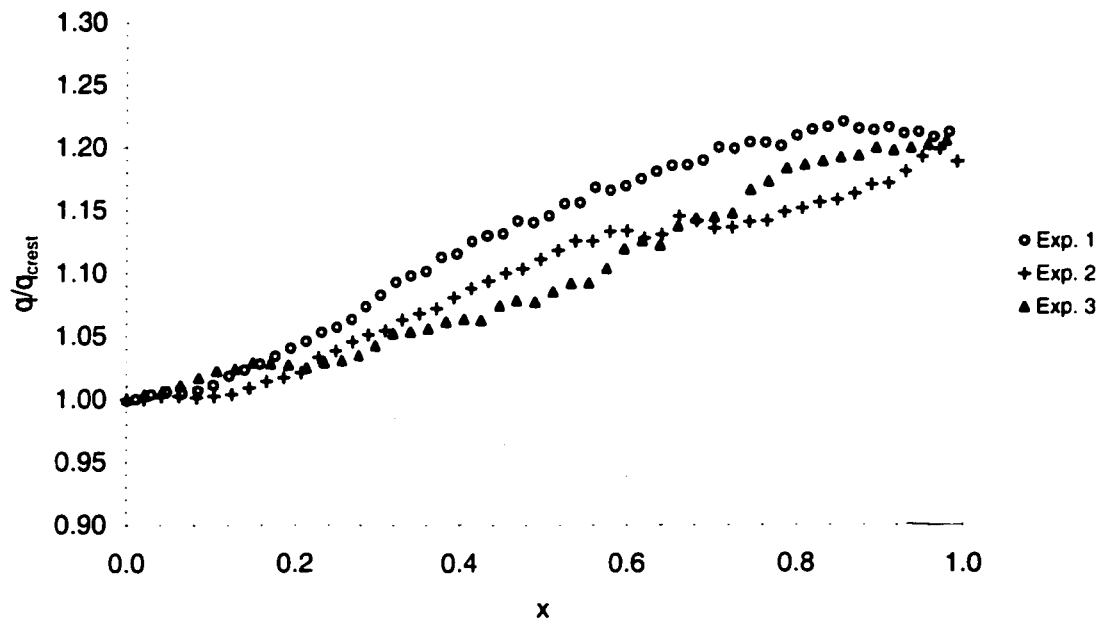


Figure 20: Variation of the flow rate divided by the sill crest flow rate along the sill for Experiments 1, 2, and 3.

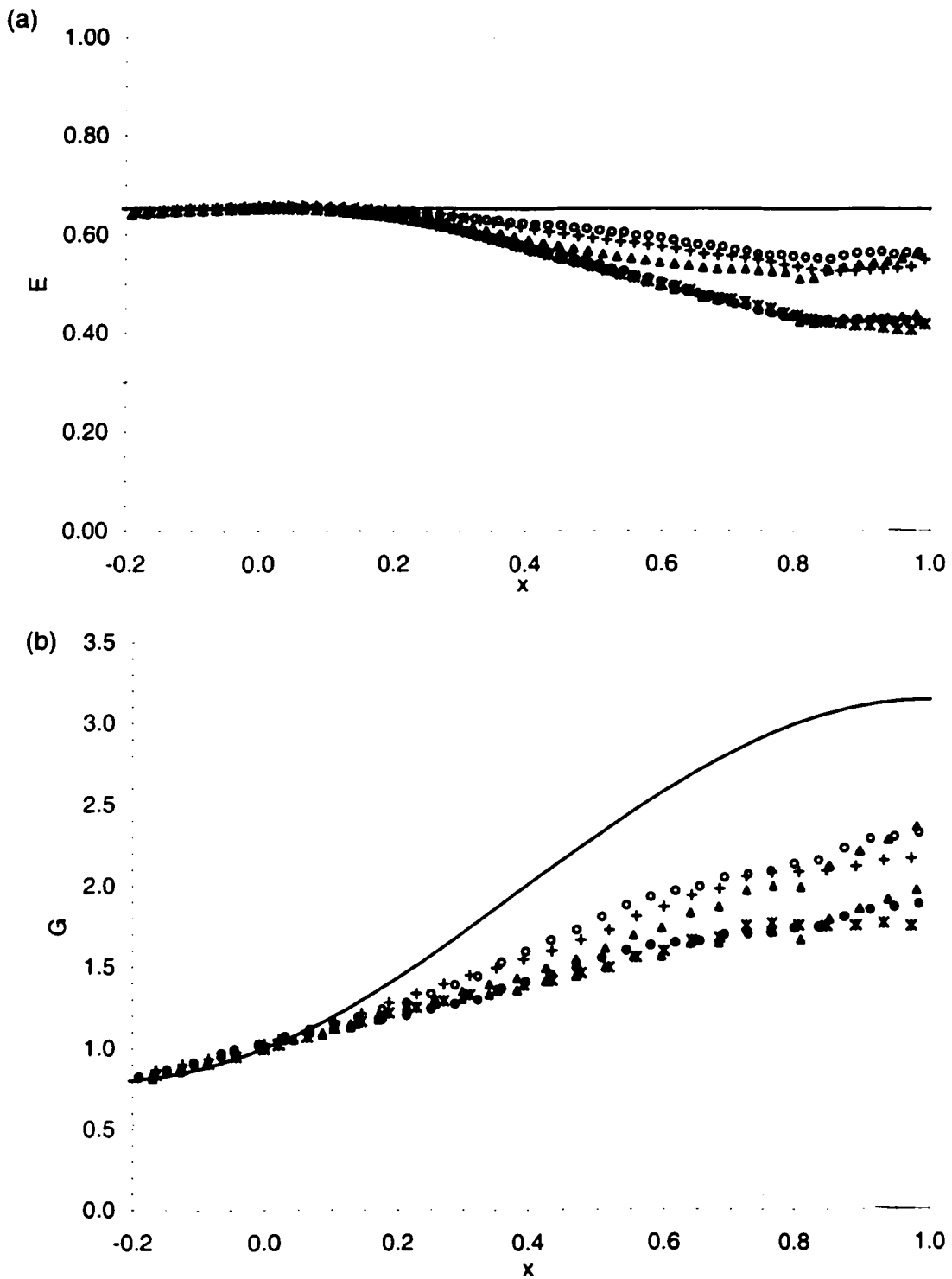


Figure 21: (a) Comparison of predictions of internal energy with experimental measurements for maximal exchange flow, (b) comparison of predictions of internal Froude number measurements for maximal exchange flow (— inviscid, hydrostatic prediction; ●, *, ▲ inviscid hydrostatic prediction of q with measured value of y for Experiments 1,2, and 3; ○, +, △ measured q and measured y for Experiments 1, 2, and 3).

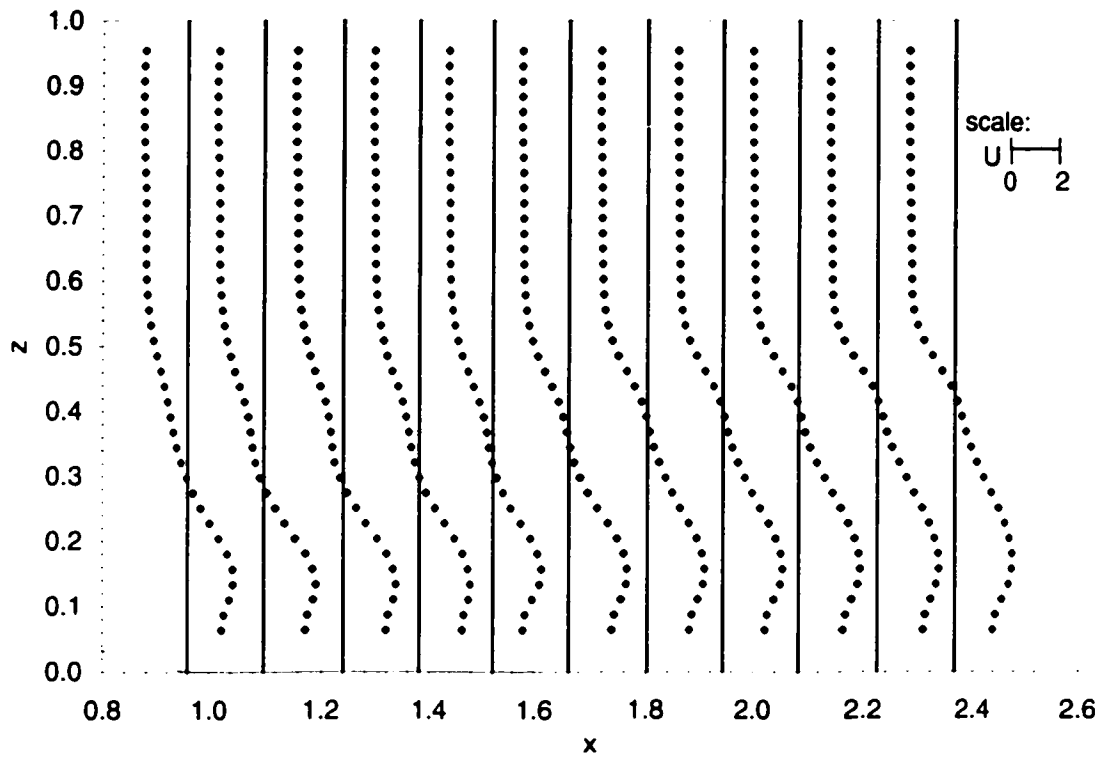


Figure 23: Average velocity profiles for Experiment 4a (velocity scale is given in cm/s).

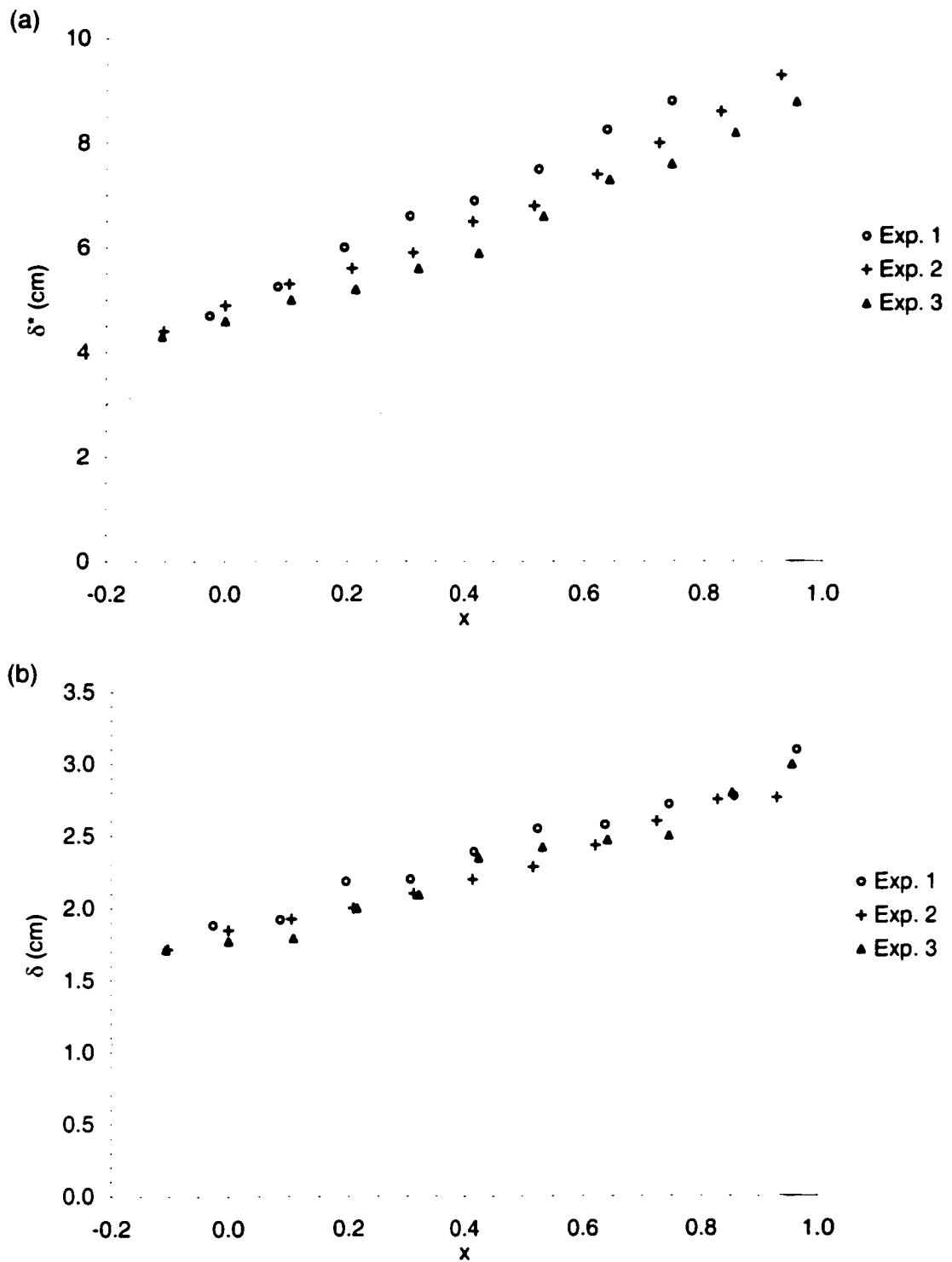


Figure 24: Variation of (a) the shear layer thickness calculated from average velocity profiles, δ^* , and (b) the shear layer thickness calculated from instantaneous velocity profiles, δ .

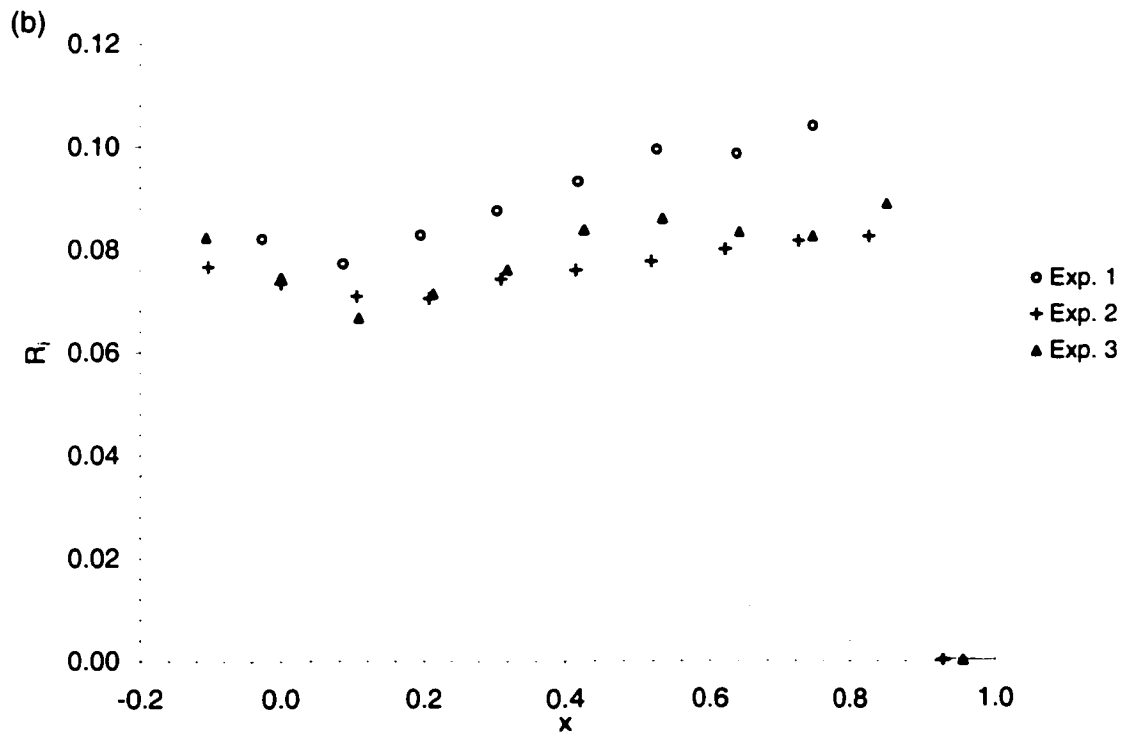
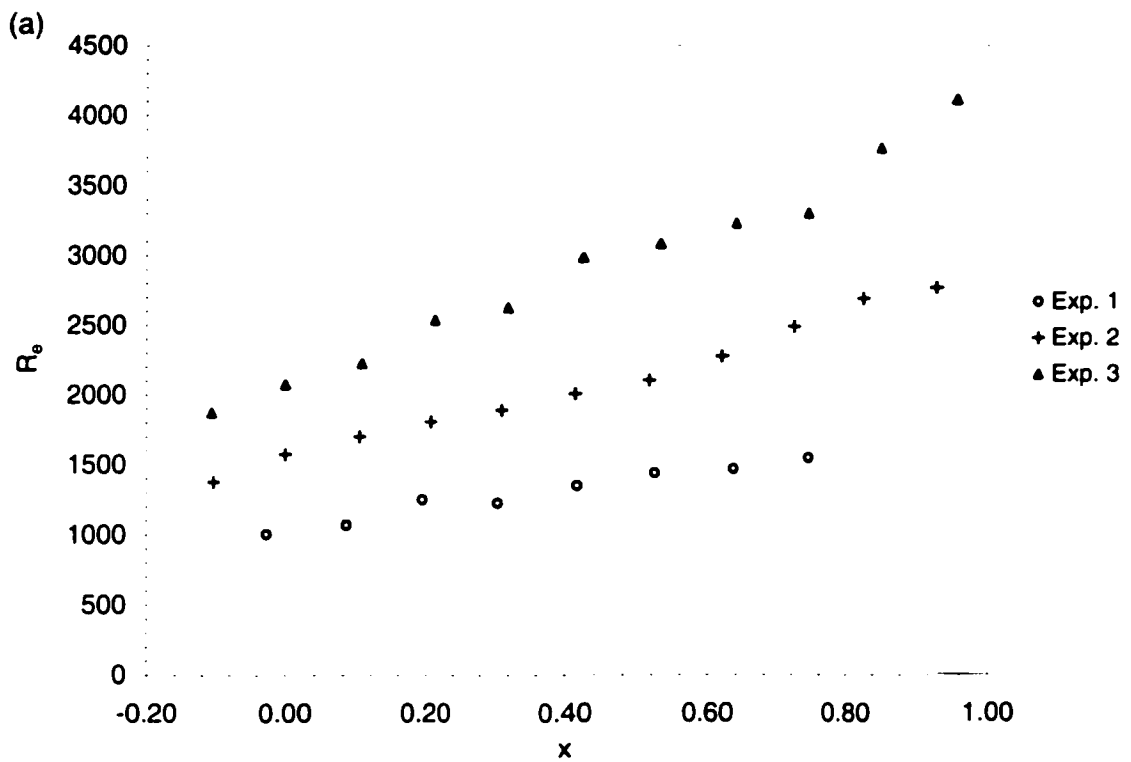


Figure 25: Variation of (a) the Reynolds number, R_e , and (b) the Richardson number, R_i , along the sill.

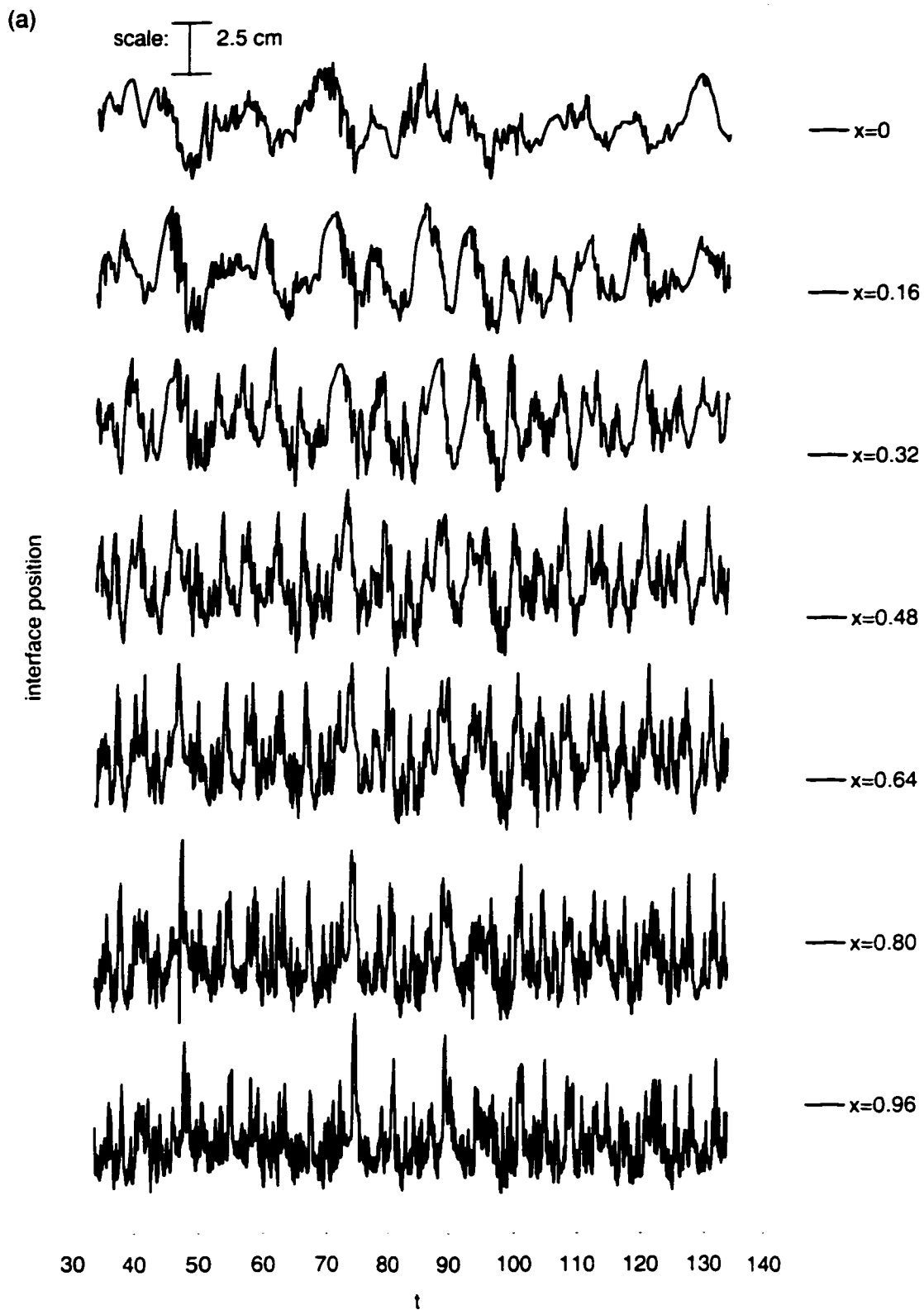


Figure 26: (a) Variation of interface position with time at different x locations for Experiment 1.

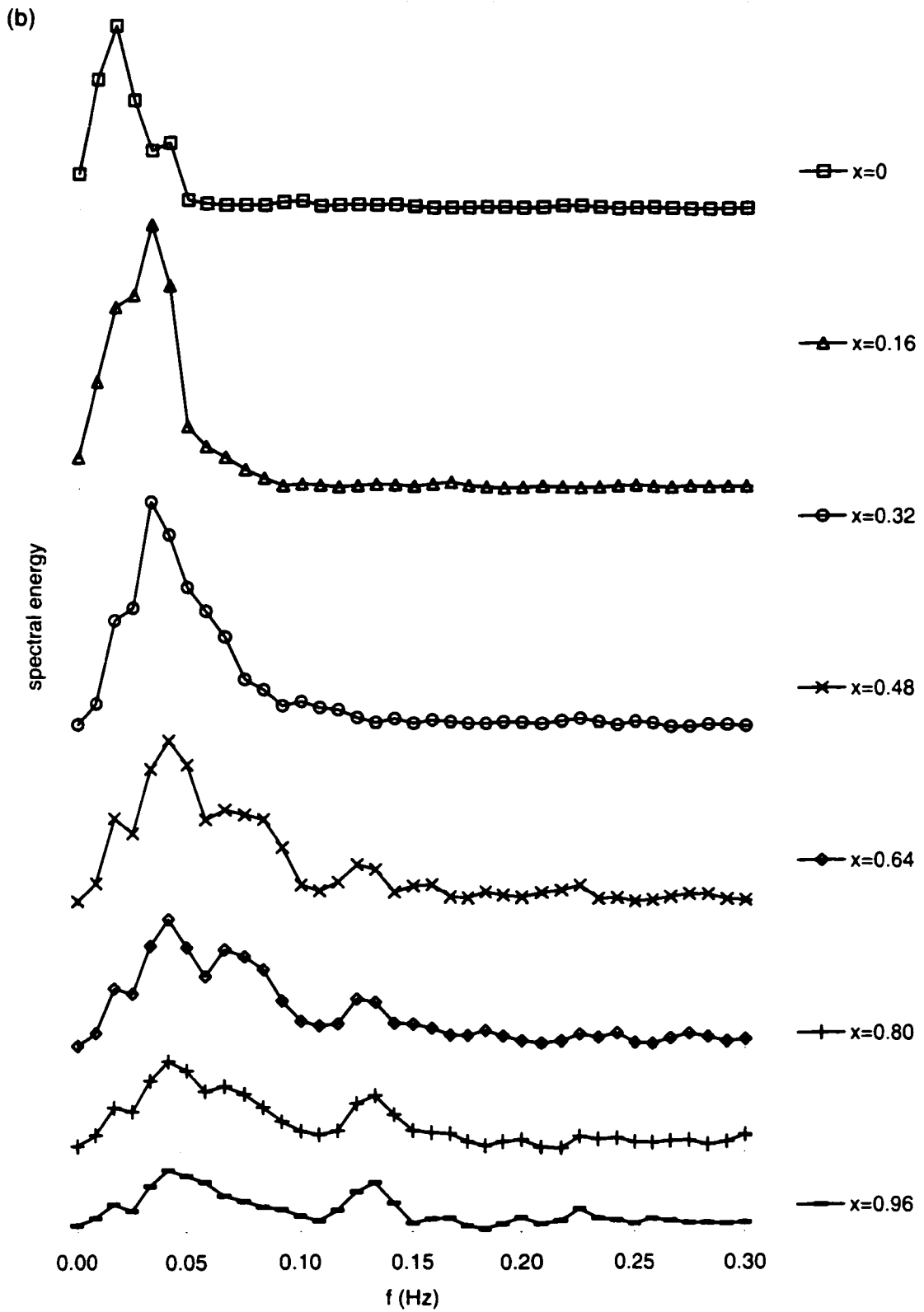


Figure 26: (b) Spectrum of the interface position time series for Experiment 1. (spectral resolution $\Delta f = 0.0083$ Hz).

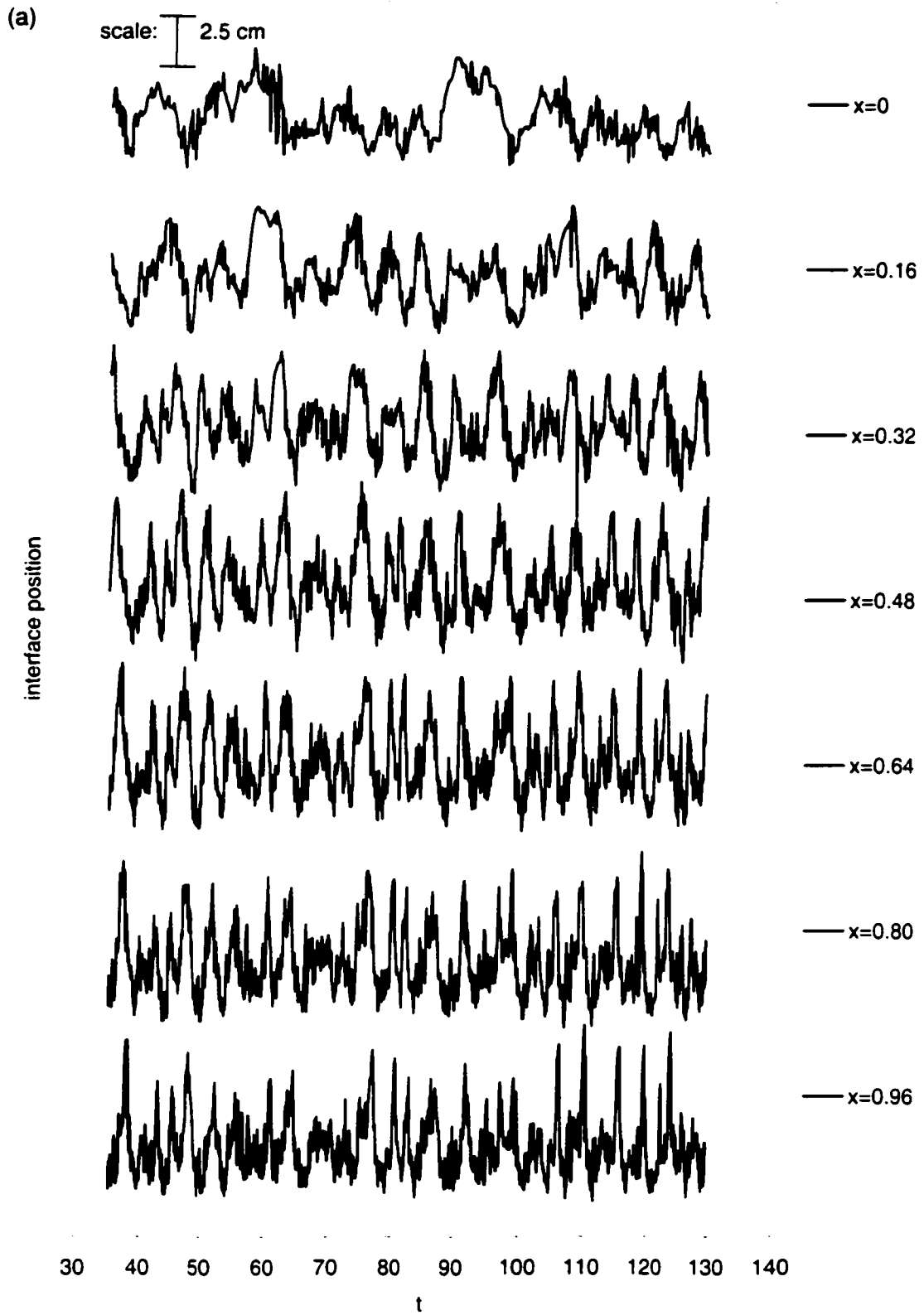


Figure 27: (a) Variation of interface position with time at different x locations for Experiment 2.

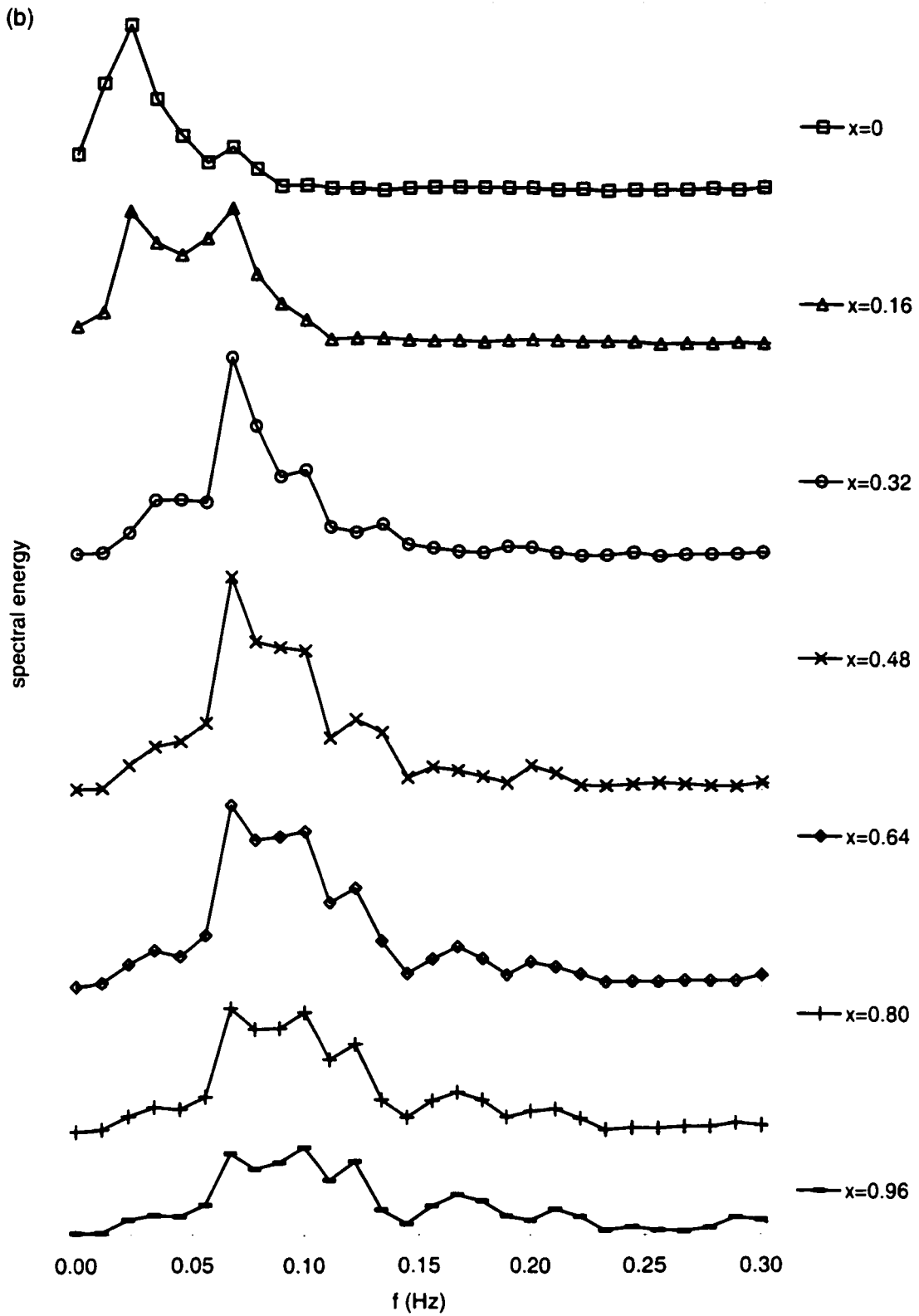


Figure 27: (b) Spectrum of the interface position time series for Experiment 2. (spectral resolution $\Delta f = 0.0111$ Hz).

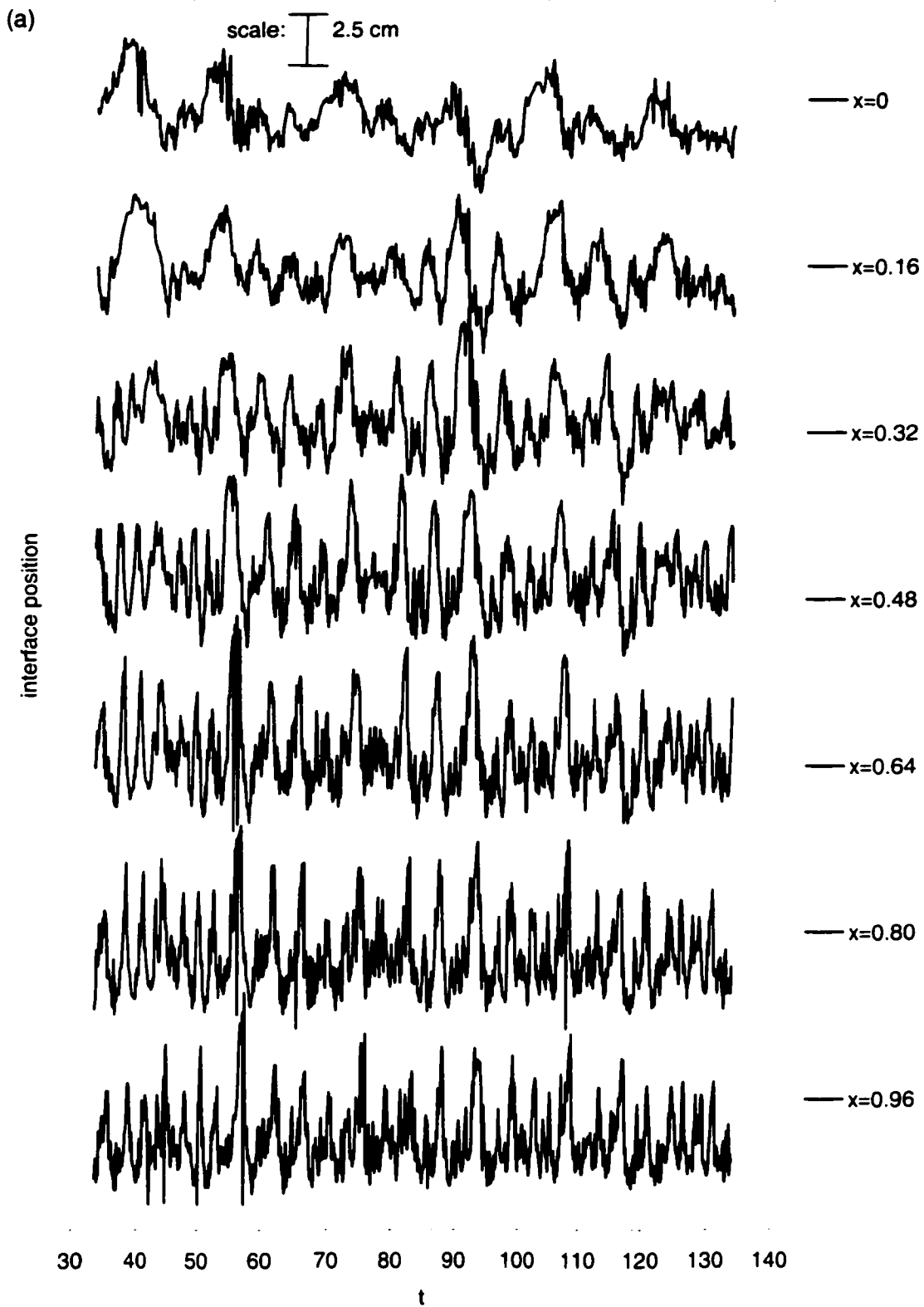


Figure 28: (a) Variation of interface position with time at different x locations for Experiment 3.

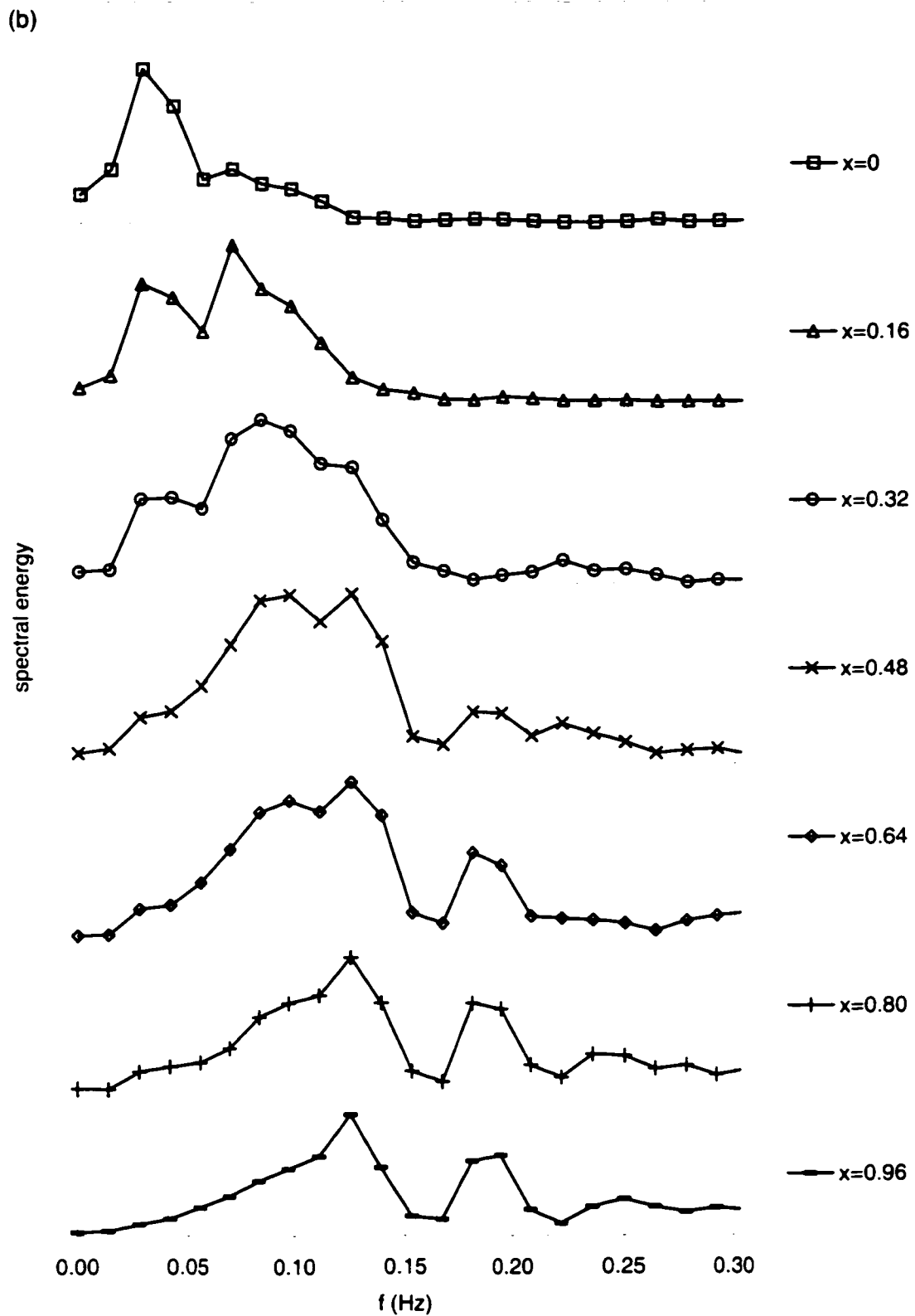


Figure 28: (b) Spectrum of the interface position time series for Experiment 3. (spectral resolution $\Delta f = 0.0139$ Hz).

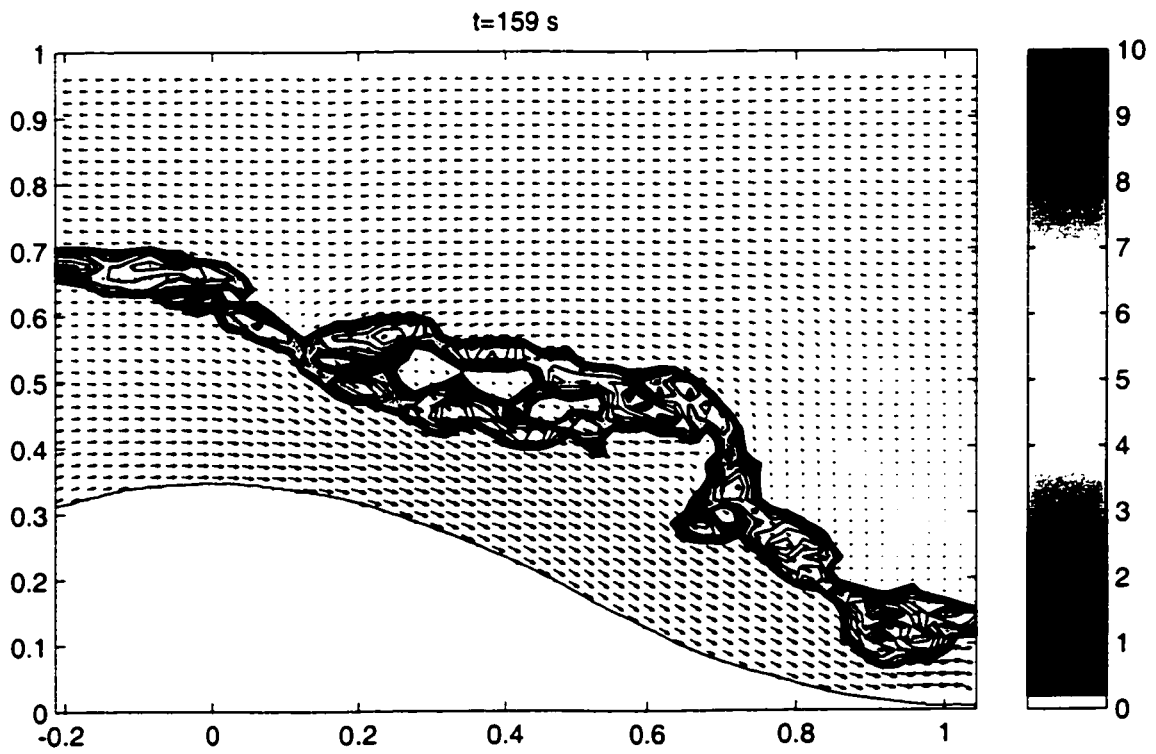
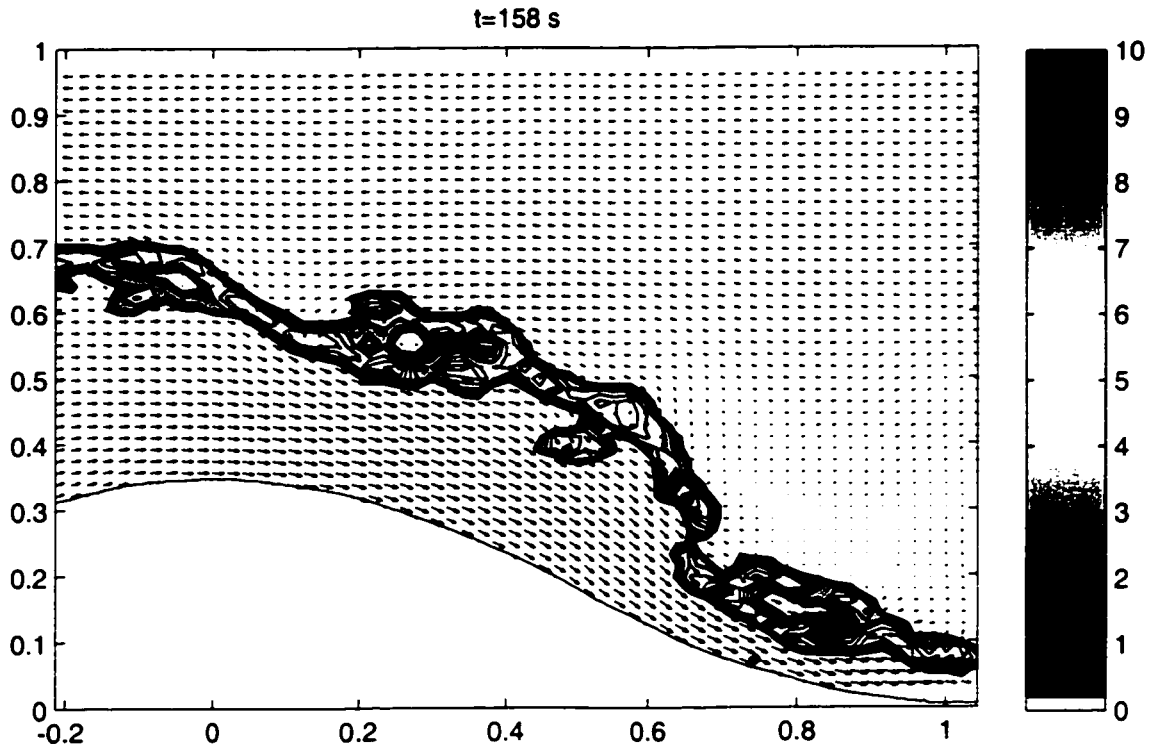
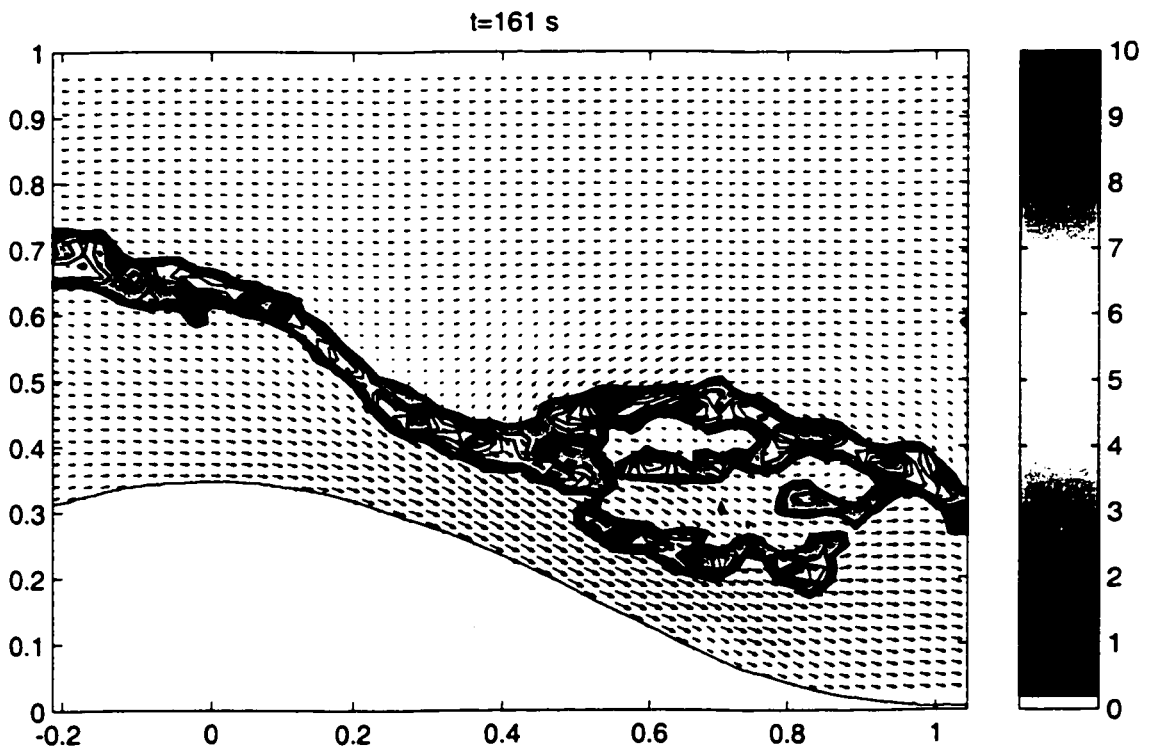
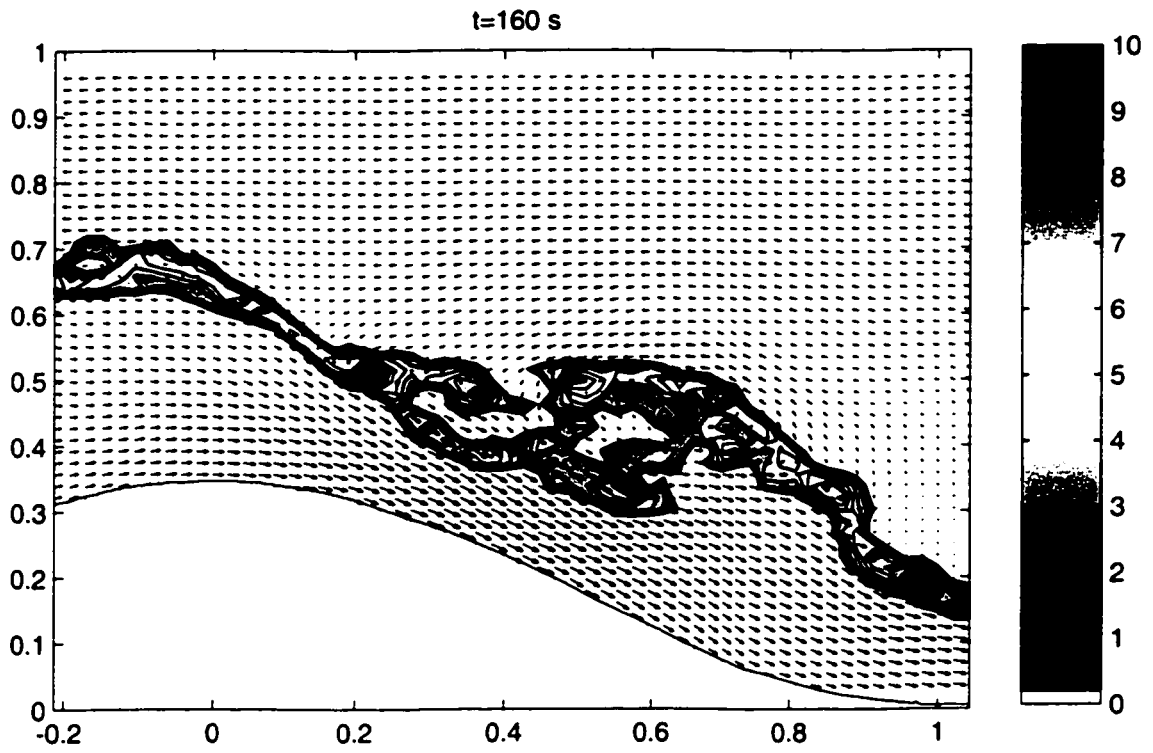
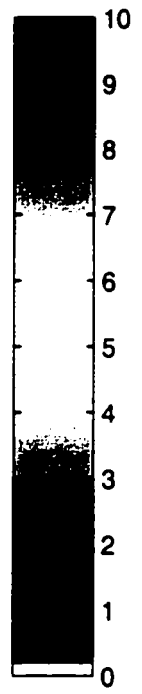
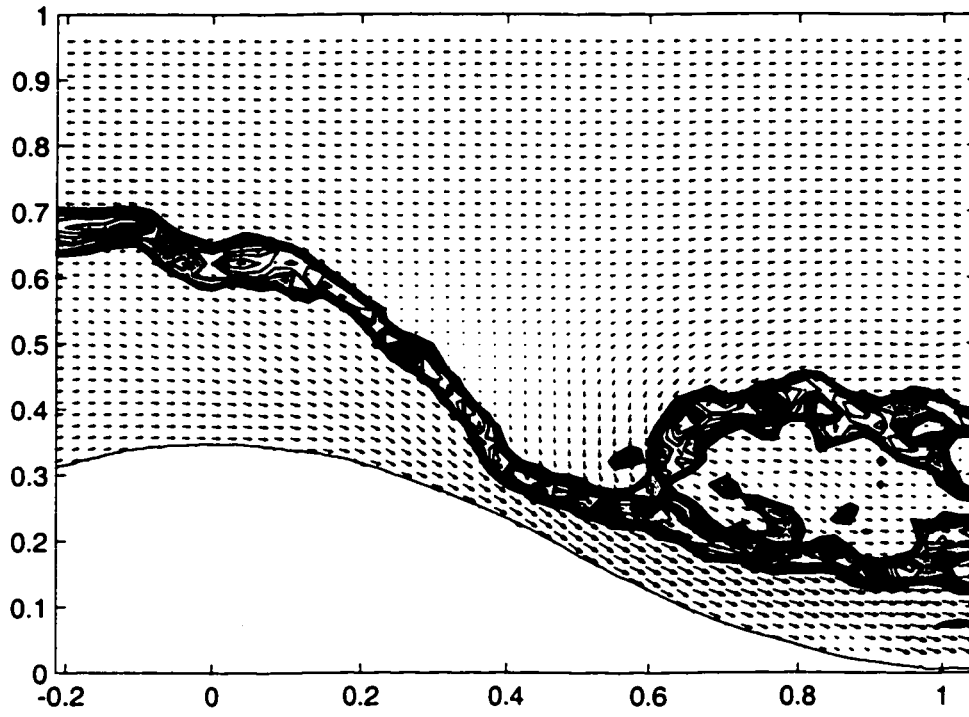


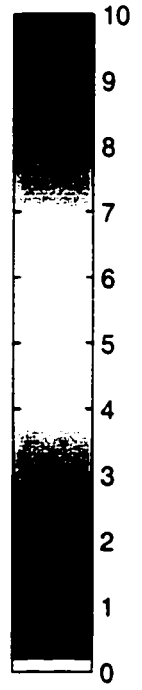
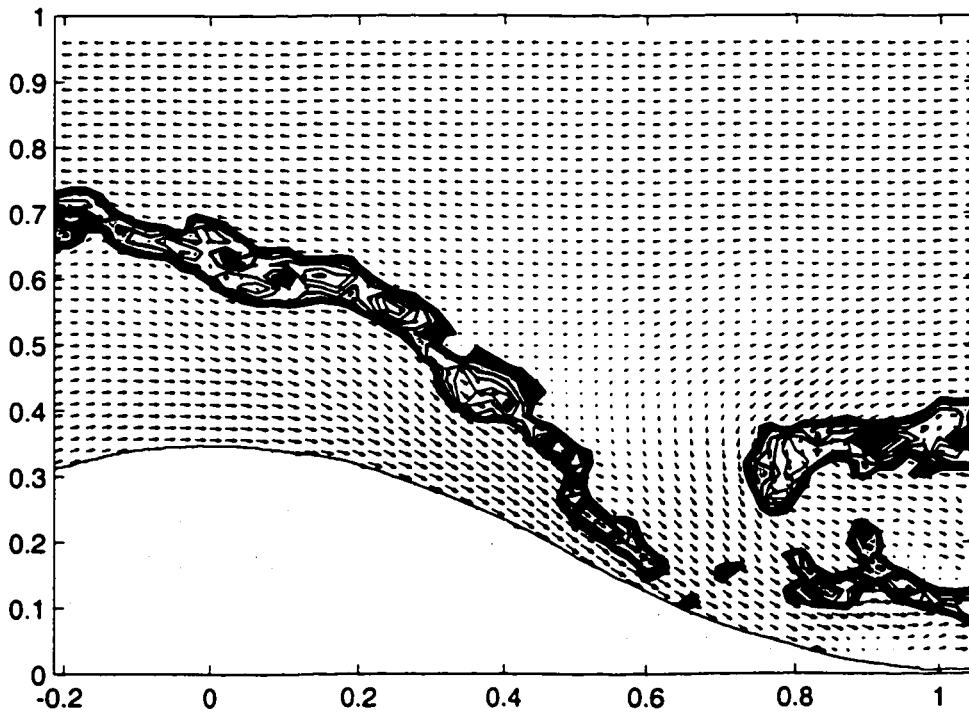
Figure 29: Series of instantaneous vorticity plots calculated from Experiment 3. Vorticity is expressed in s⁻¹.



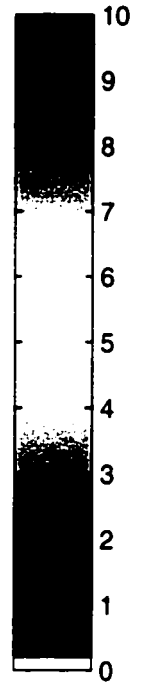
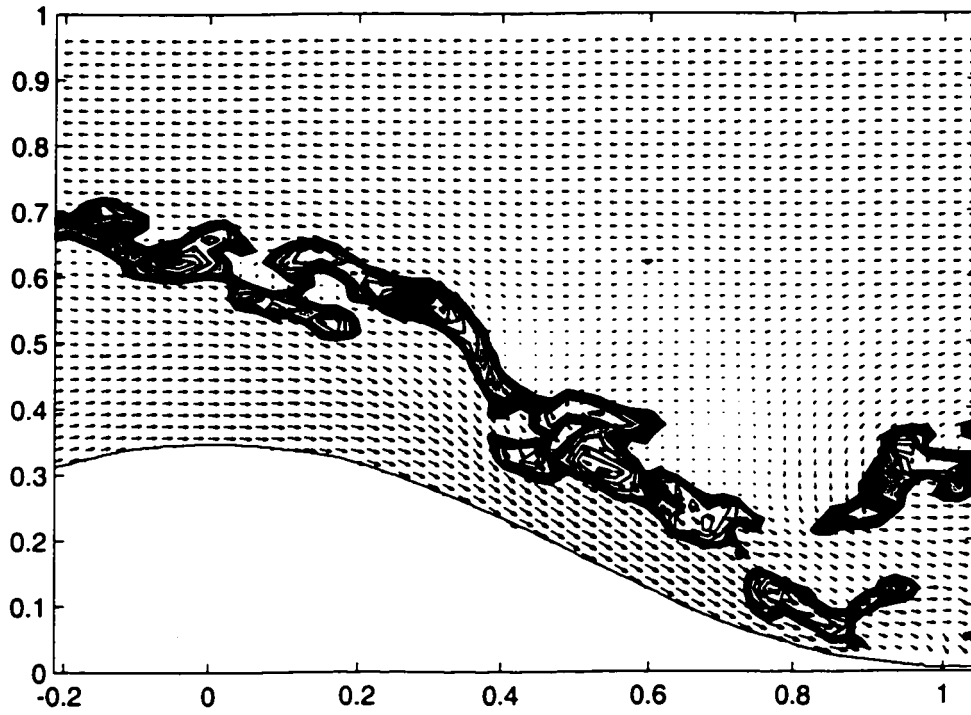
t=162 s



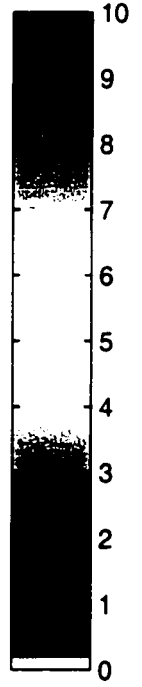
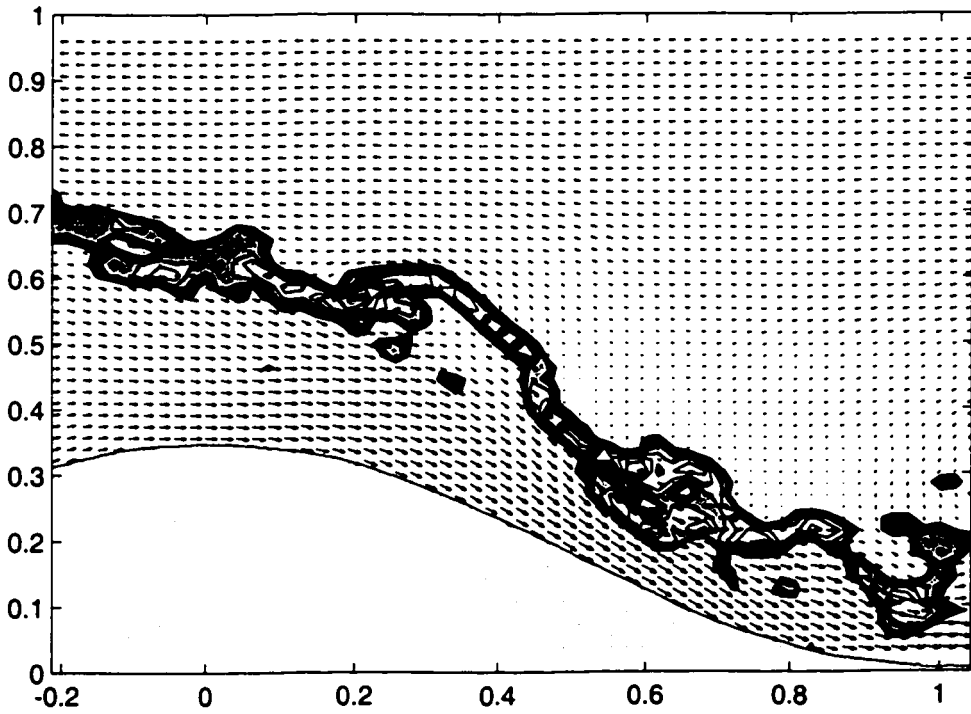
t=163 s



t=164 s



t=165 s



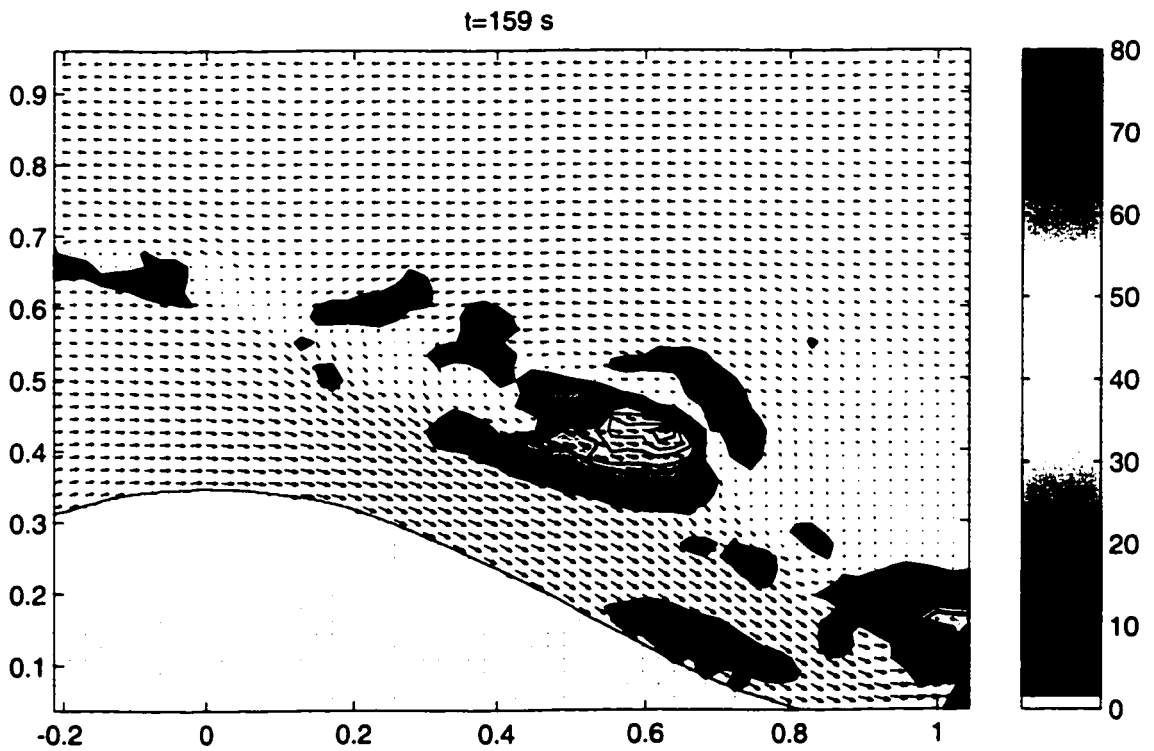
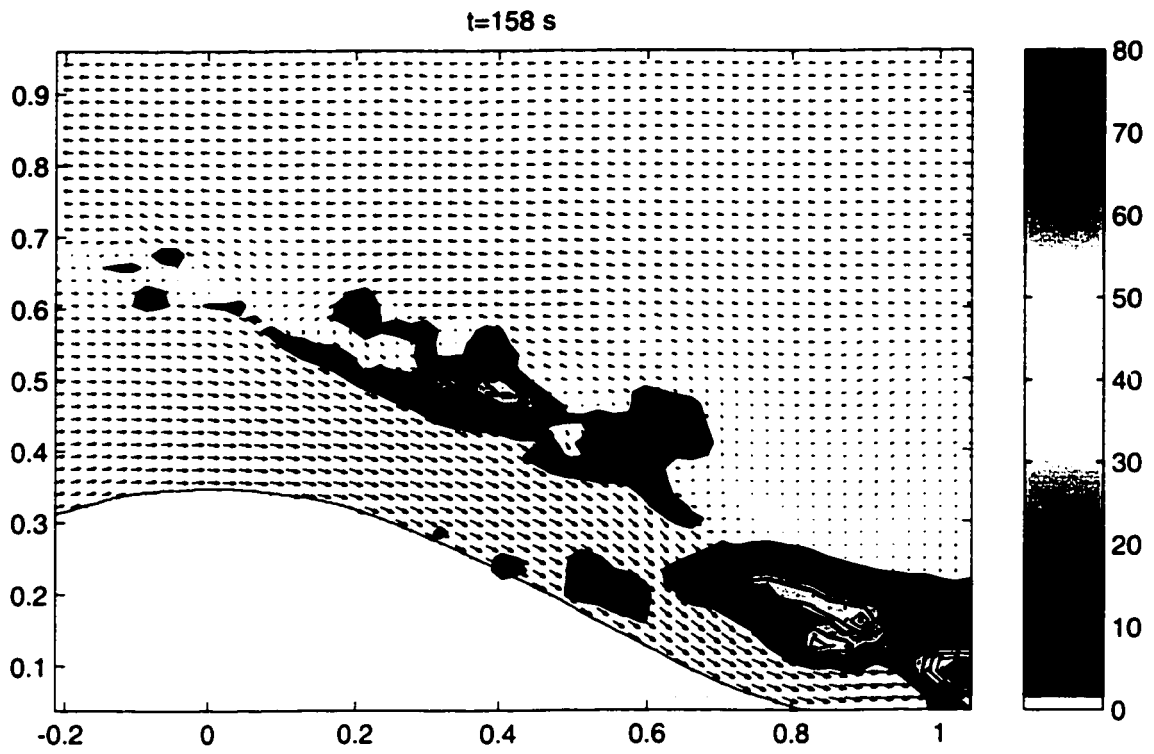
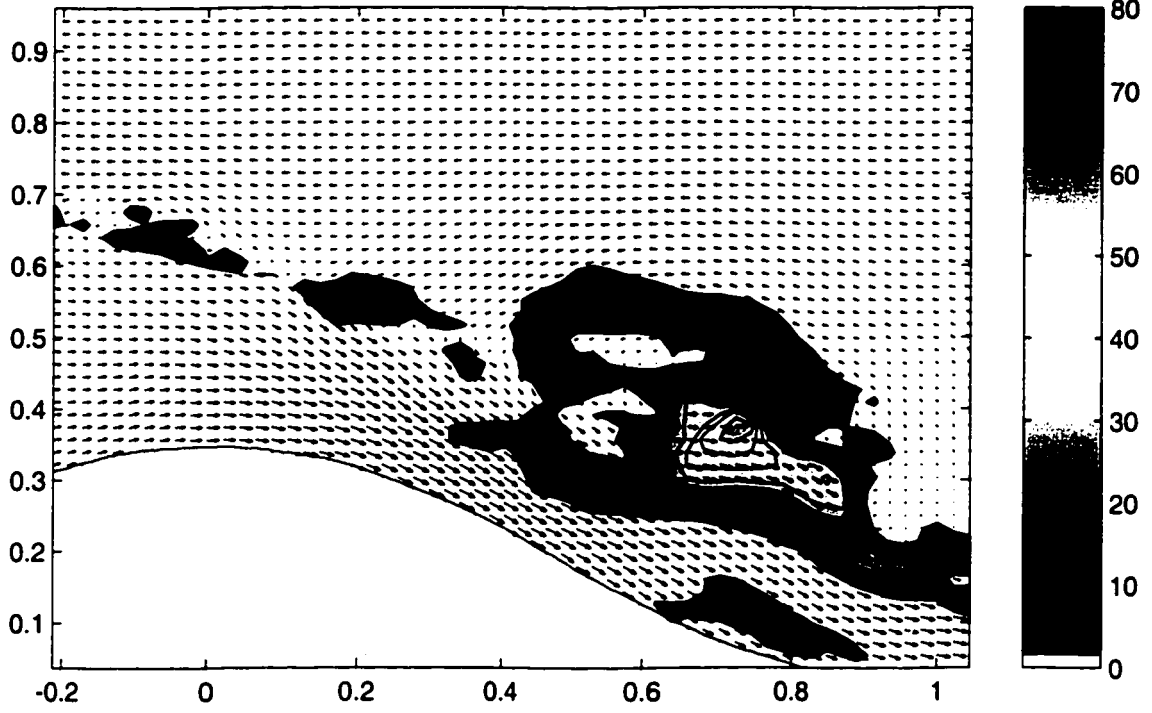
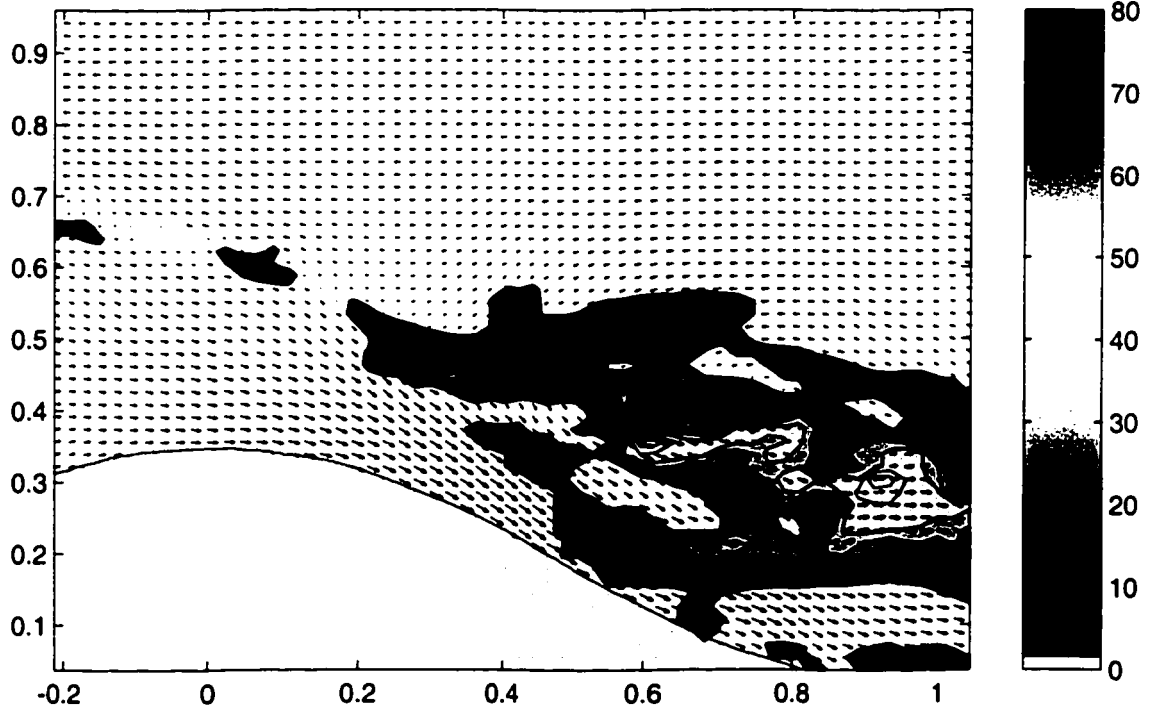


Figure 30: Series of instantaneous turbulent kinetic energy plots calculated from Experiment 3. Turbulent kinetic energy is expressed in cm^2/s^2 .

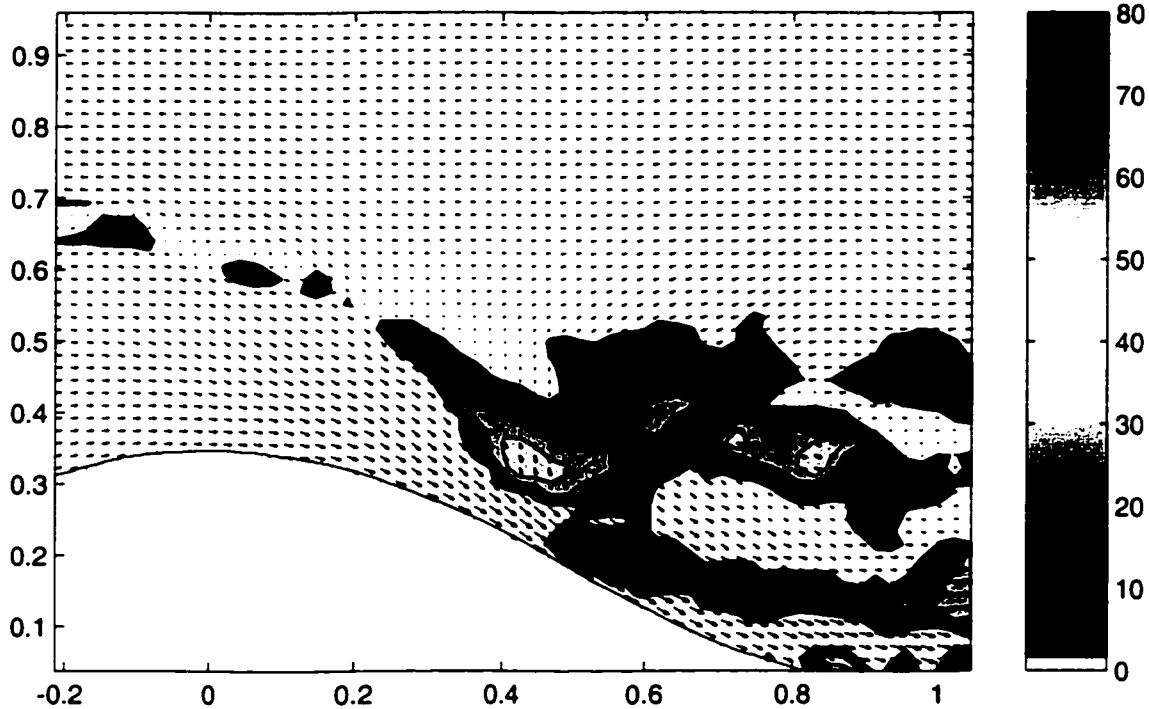
t=160 s



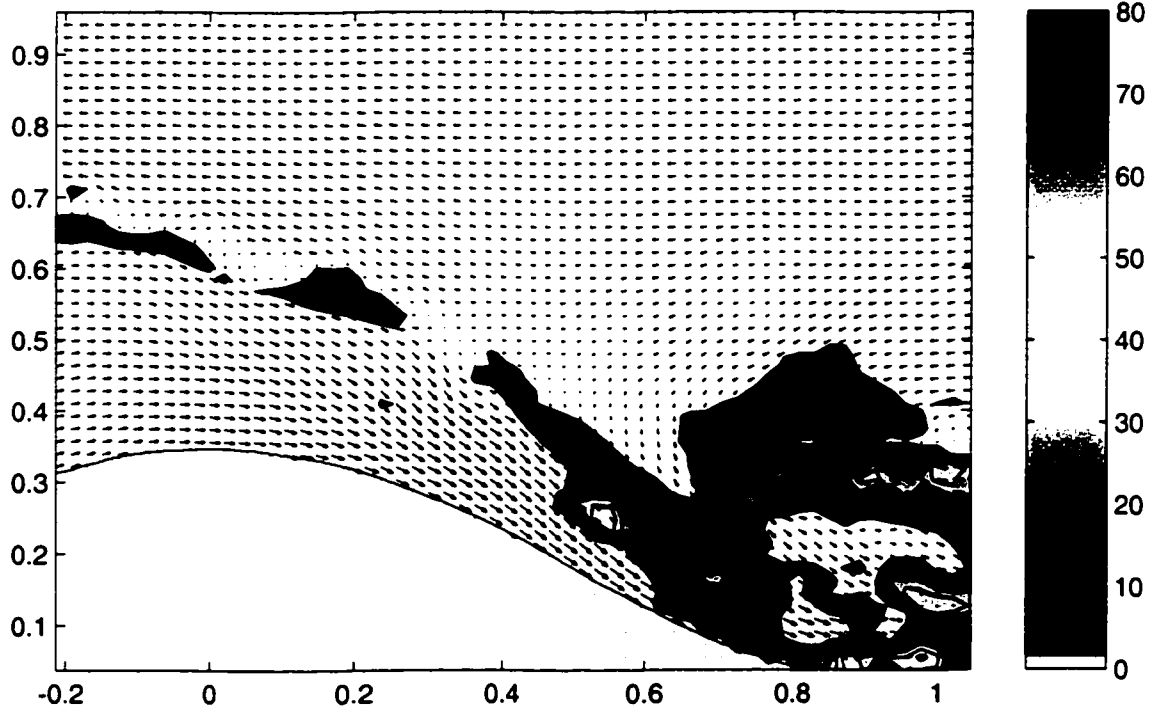
t=161 s



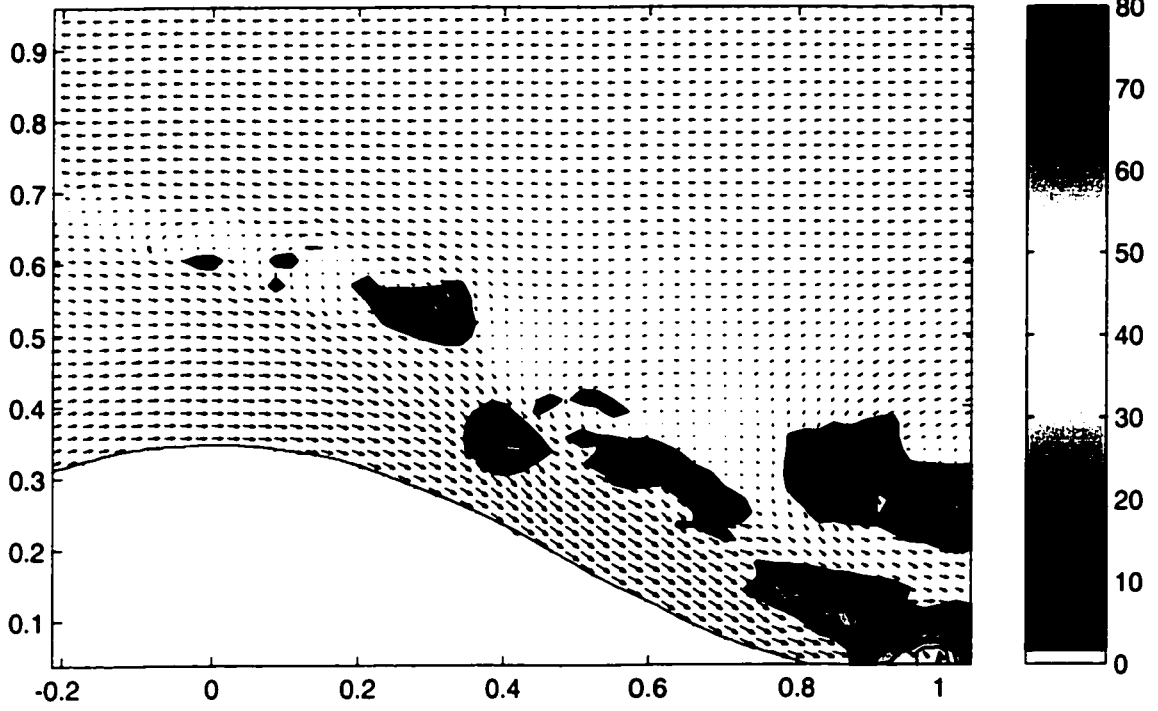
t=162 s



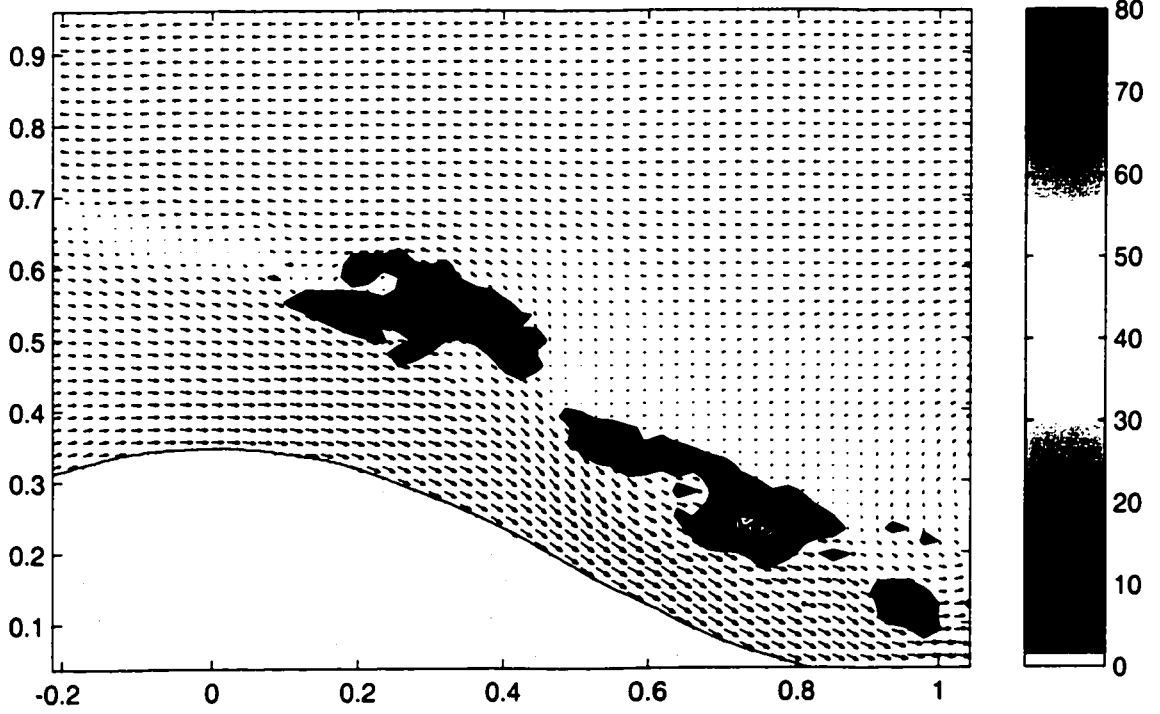
t=163 s



t=164 s



t=165 s



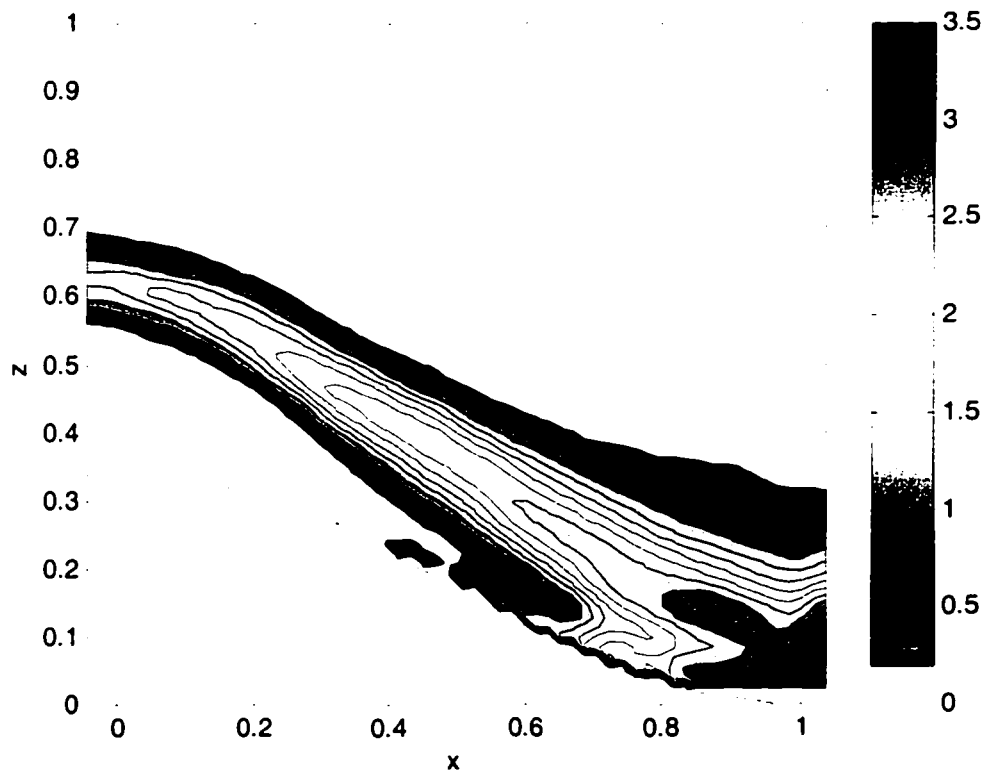
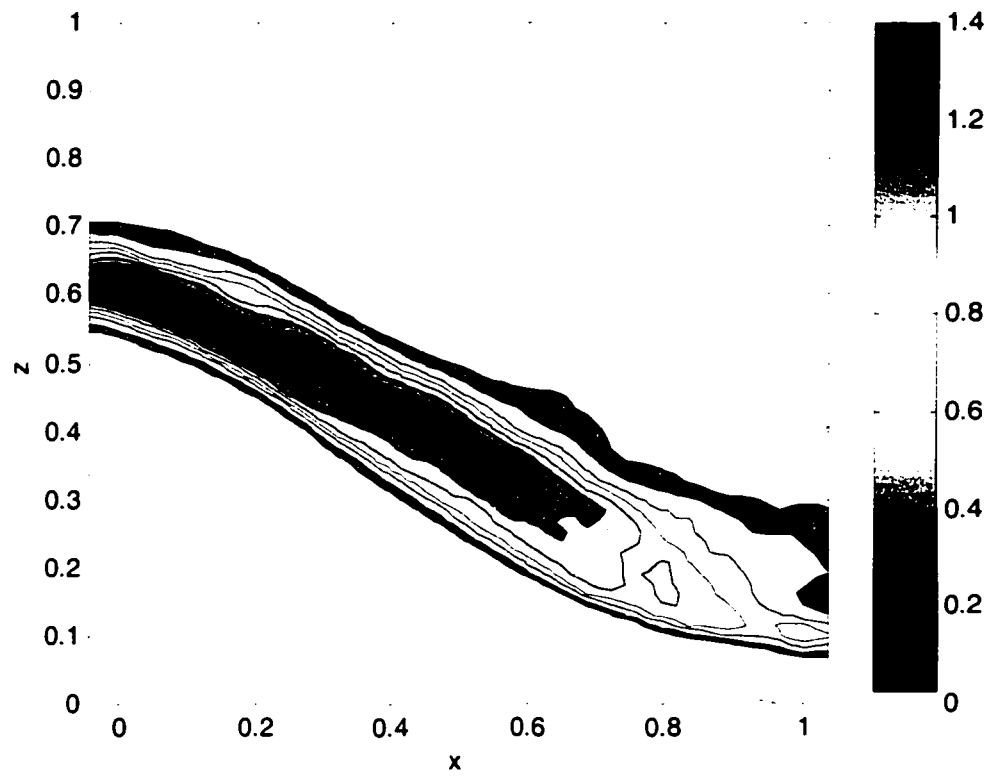


Figure 31: (a) Average vorticity field (s^{-1}) computed for Experiment 1, (b) average turbulent kinetic energy (expressed in cm^2/s^2) field computed for Experiment 1.

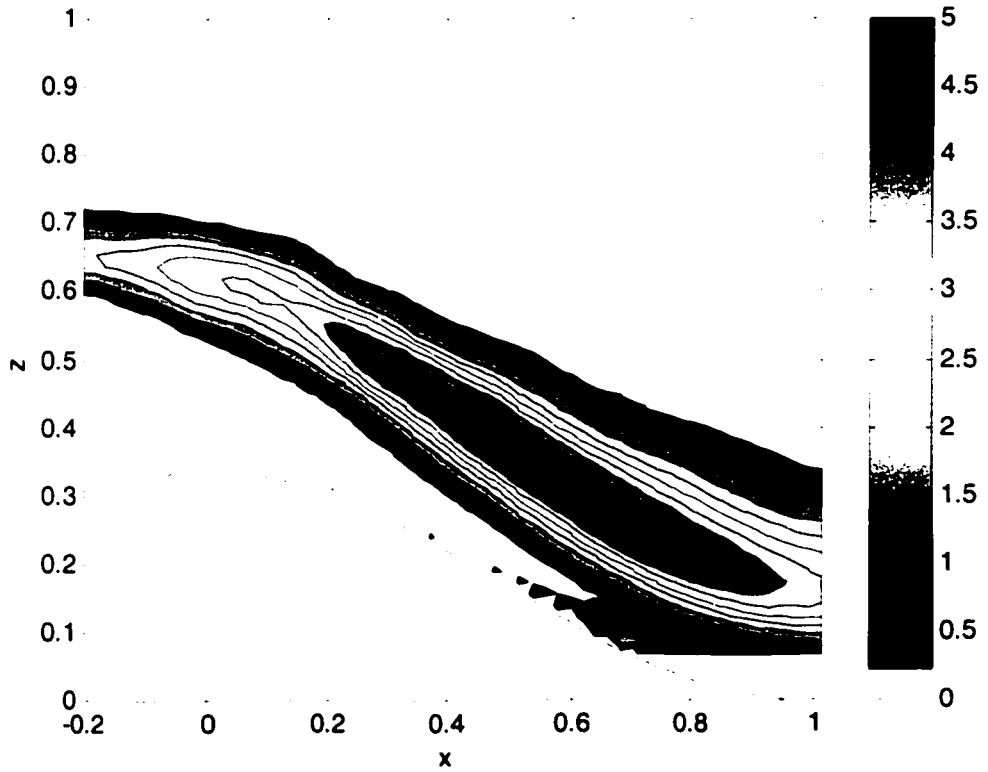
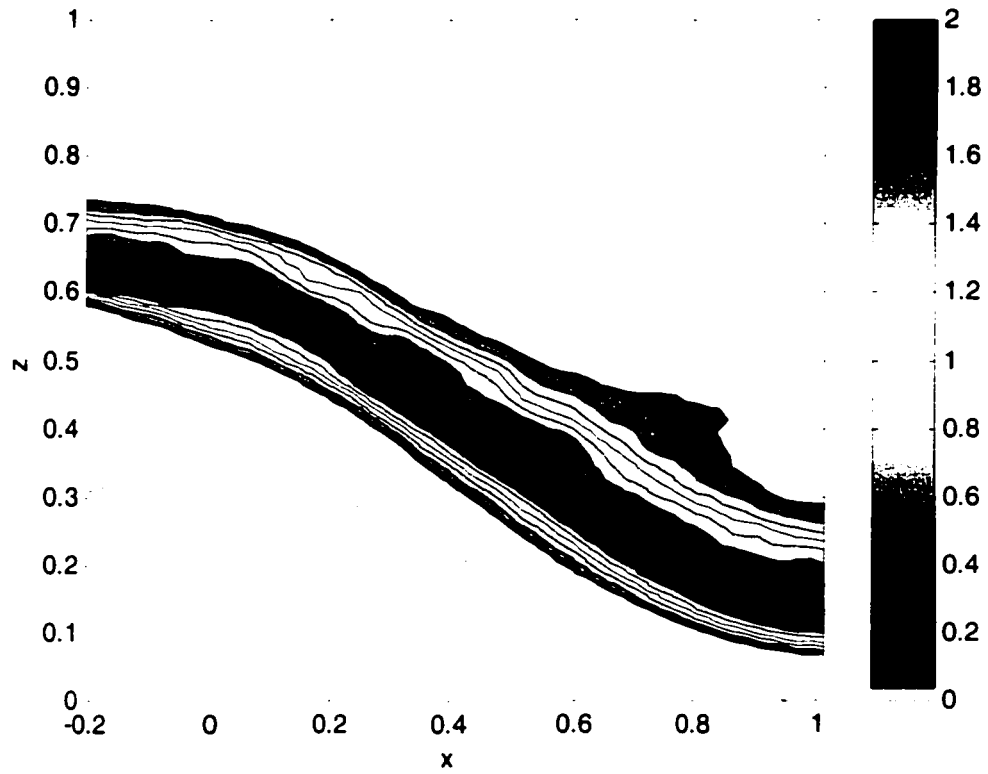


Figure 32: (a) Average vorticity field (s^{-1}) computed for Experiment 2, (b) average turbulent kinetic energy (expressed in cm^2/s^2) field computed for Experiment 2.

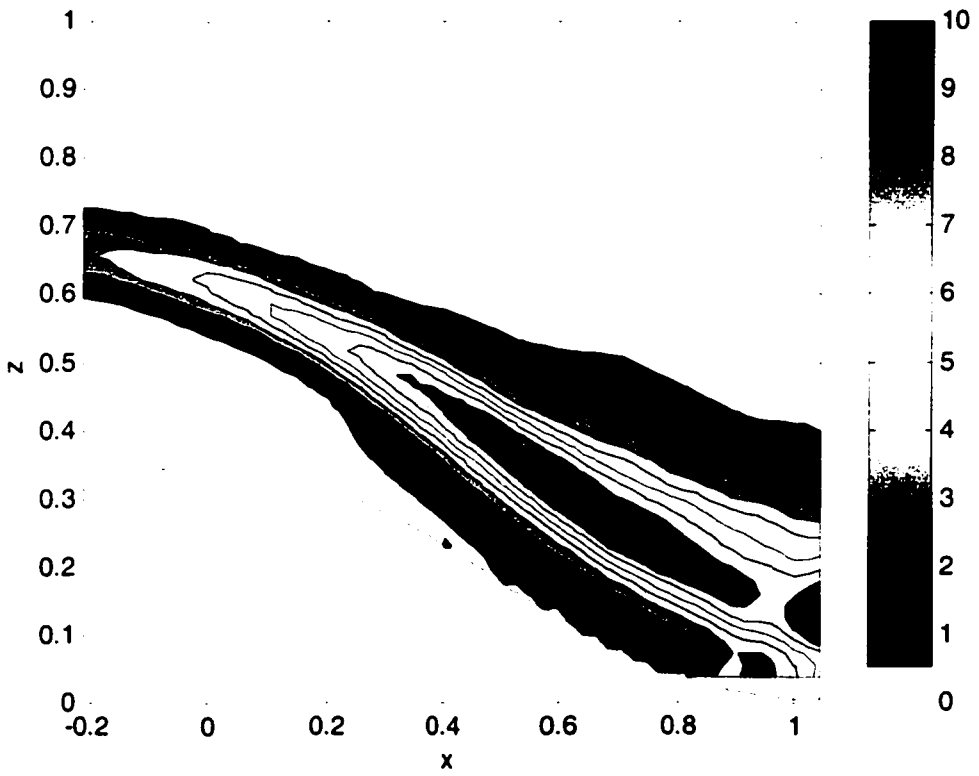
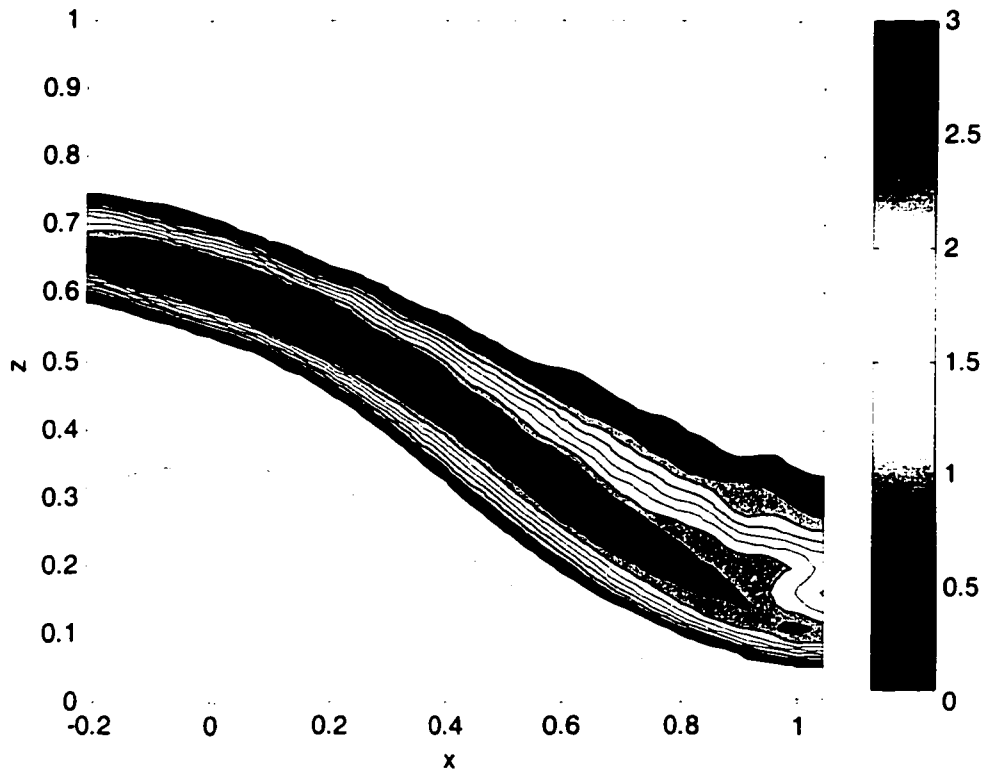


Figure 33: (a) Average vorticity field (s^{-1}) computed for Experiment 3, (b) average turbulent kinetic energy (expressed in cm^2/s^2) field computed for Experiment 3.

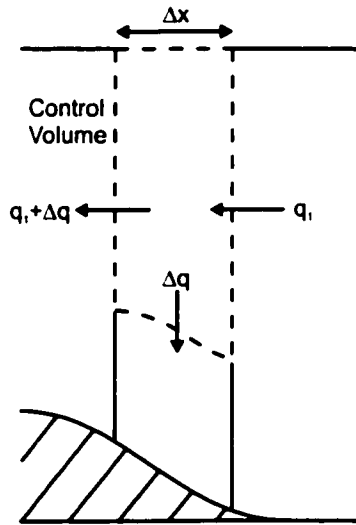


Figure 34: Entrainment of fluid from the upper into the lower layer.

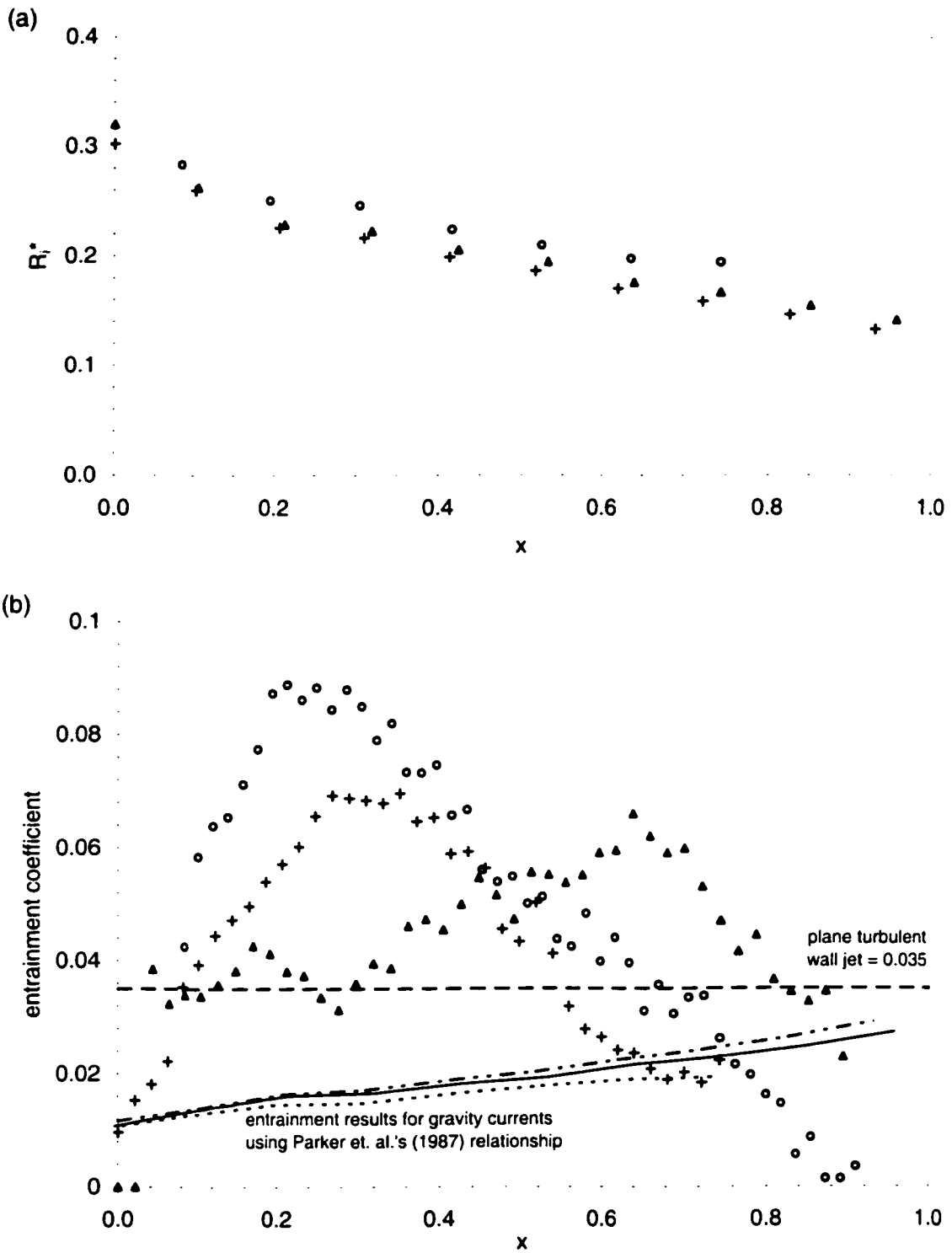


Figure 35: (a) Variation of Ri' (\circ , $+$, Δ Experiments 1, 2, and 3, respectively), (b) variation of the entrainment coefficient along the sill (\circ , $+$, Δ using Equation 28 for Experiments 1, 2, and 3, respectively; , - - - , ——— entrainment results for gravity currents using Parker et al.'s (1987) relationship and Ri' values from Experiments 1, 2, and 3, respectively; - - - entrainment coefficient for a plane turbulent wall jet (Rajaratnam, 1976).

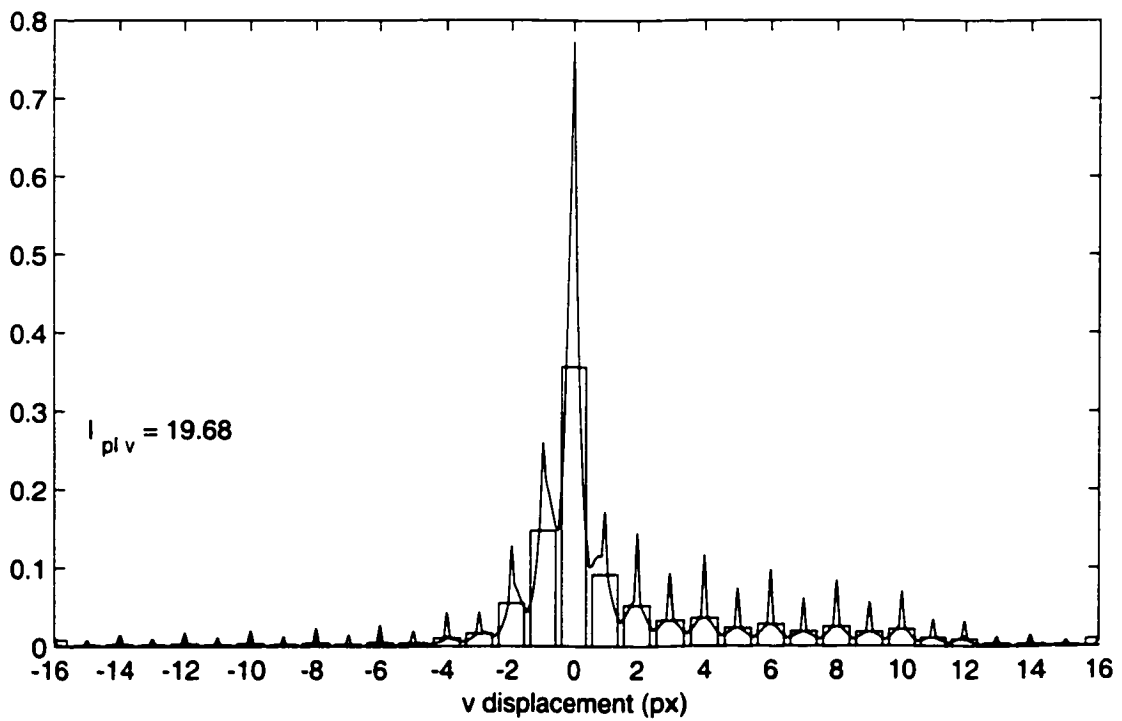
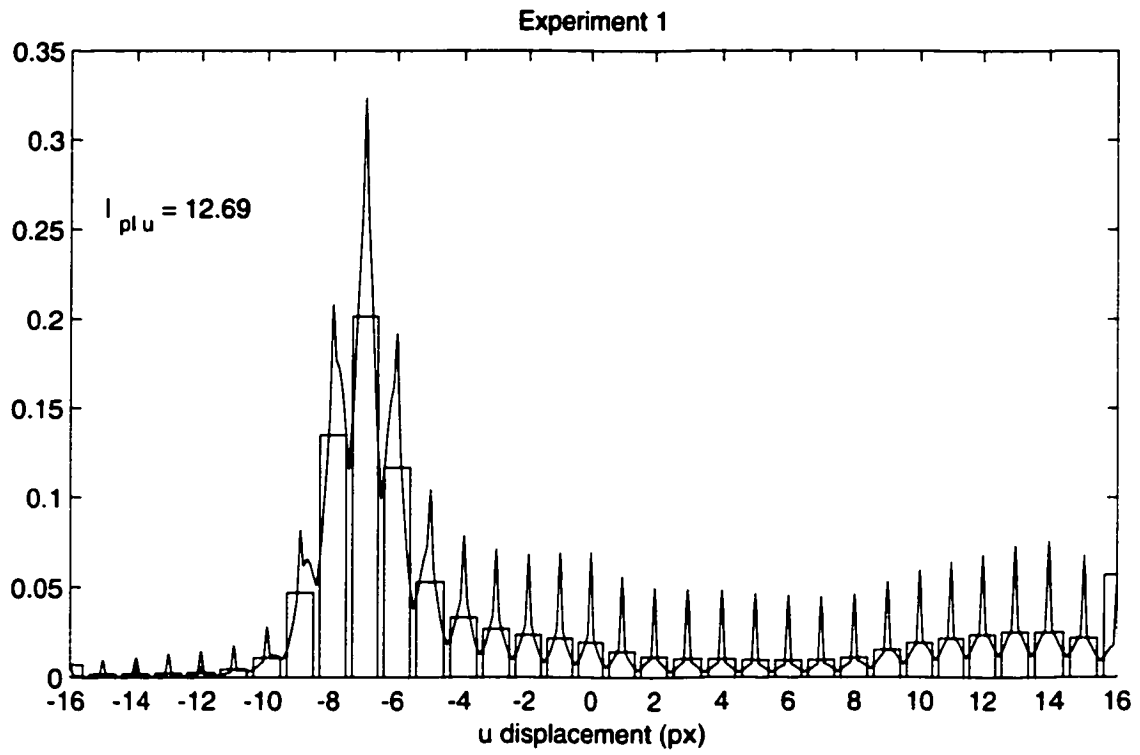
8.0 Appendix

8.1 List of Programs Used for Data Processing

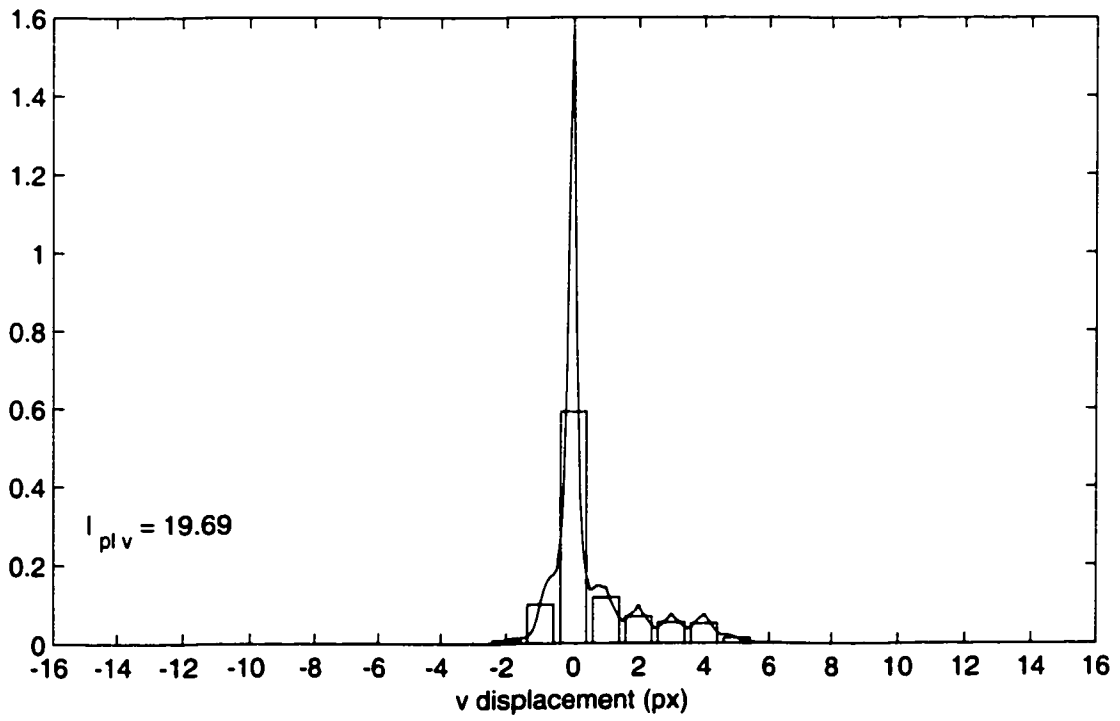
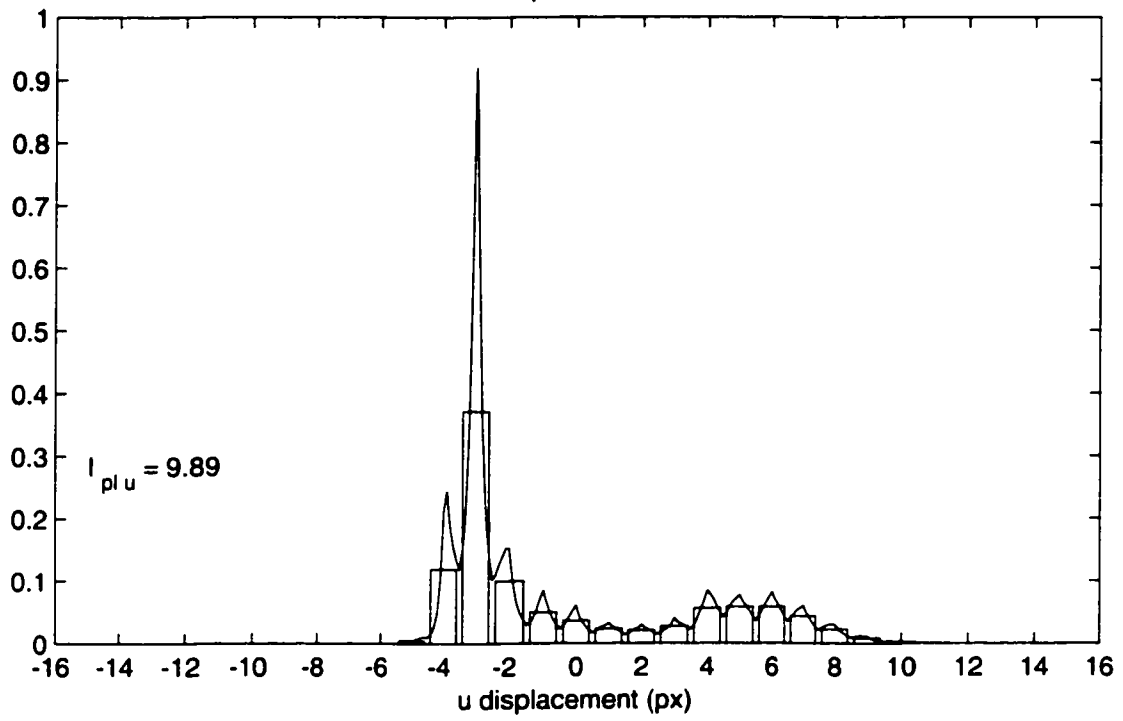
Contents of CD:

- 1 sill_location.m
- 2 image_processing.m
- 3 PIV_correct_interpolate.m
- 4 peaklock.m
- 5 calculating_average_data.m
- 6 vorticity_TKE_calculations
- 7 average_flow_rate_vs_x.m
- 8 instantaneous_flow_rate_at_x_location.m
- 9 contouring_TKE.m
- 10 contouring_vorticity.m
- 11 interface_location.m
- 12 interface_locationb.m

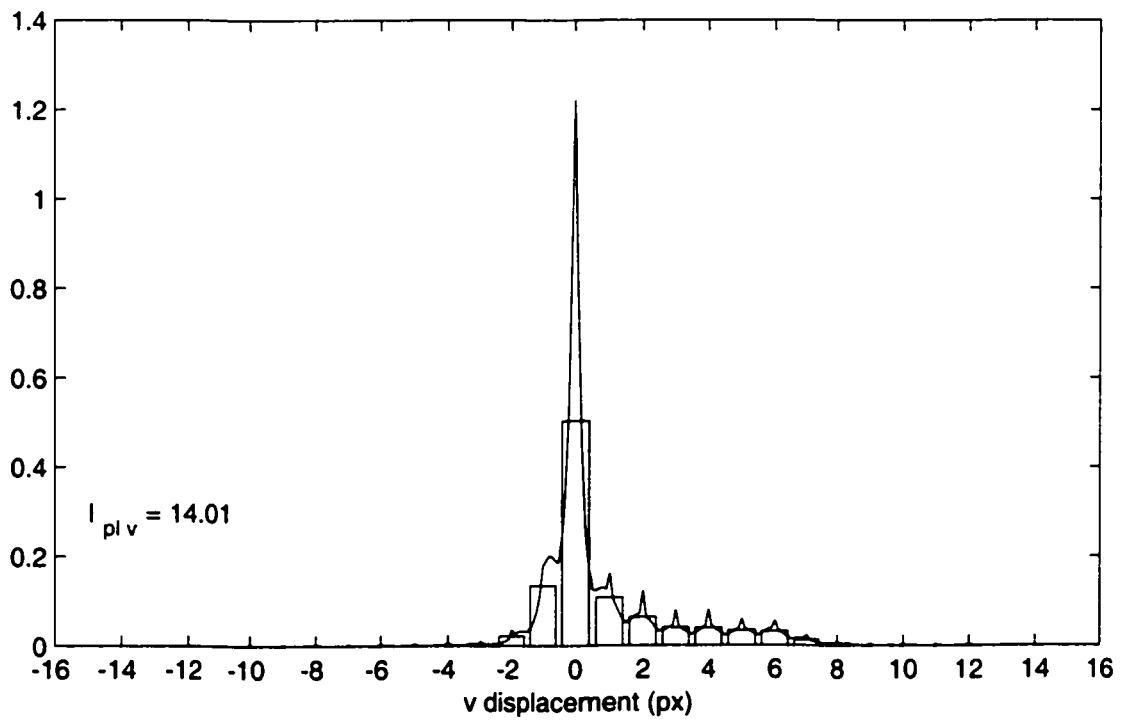
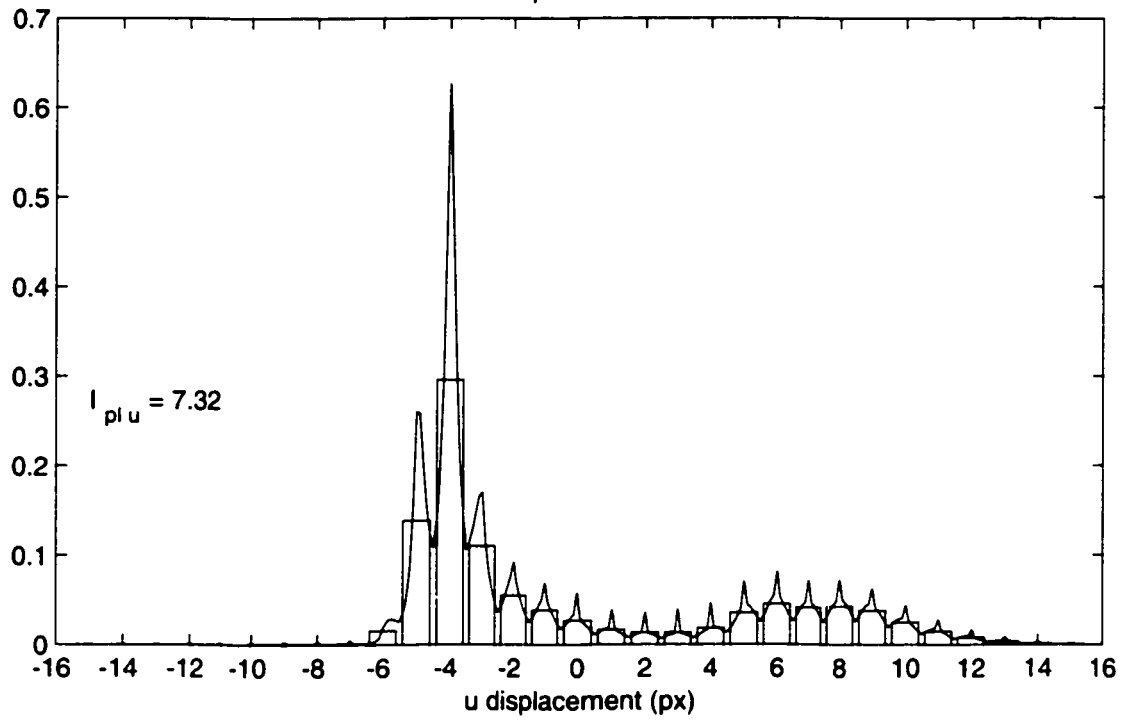
8.2 Peak Locking Results



Experiment 2



Experiment 3



8.3 Raw Shear Layer Thickness Data

Experiment 1

x (cm)	t-> (min)	2.00	2.33	2.67	3.00	3.33	3.67	4.00	4.33	4.67	5.00	5.33	5.67	6.00	6.33	6.67	7.00	7.33	7.67	8.00	ave	stdev
-0.64	2	1.8	1.8	2	2.2	2.1	2.2	1.7	2	1.9	2	1.4	2	1.9	2	1.9	2.1	1.9	1.8	1.8	1.88	0.25
2.11	1.8	1.9	2	2.3	2.4	2.3	1.8	1.8	1.8	1.8	1.8	1.8	1.9	2	1.9	2.1	2.1	2.1	1.8	1.8	1.92	0.15
4.86	1.7	1.8	2.1	2.3	2.4	2.4	1.8	1.8	2.4	1.8	1.8	2	2.3	2.3	2.1	2.6	2.5	2.6	2.6	2.18	0.32	
7.61	2.3	2.8	2	2.1	2	2.2	2.1	2	2.2	2.1	2	2	2.2	2	2	2	2.5	2.6	2.2	2.2	2.18	0.32
10.40	2.4	2.1	2.7	2.1	2.7	2.1	2.1	2.8	2.7	2.1	2.7	2.8	2.4	2.1	2.7	2.1	2.1	2.1	2.2	2.3	2.2	0.23
13.10	2.4	2.5	2.3	2.5	2.3	2.9	2.3	3.1	2.9	2.3	3.1	2.5	2.5	2.3	2.3	2.3	2.3	2.3	2.5	2.9	2.39	0.3
15.90	2.9	2.5	2.5	2.5	2.5	2.5	2.5	2.5	2.5	2.5	2.5	2.5	2.5	2.5	3.1	3.1	2.6	2.5	2.5	2.55	0.3	
18.60	2.9	2.5	2.7	2.9	2.7	2.9	2.7	2.7	2.9	2.7	2.7	2.9	2.9	2.7	2.7	2.7	2.6	2.6	2.5	2.72	0.16	
21.40	2.8	2.8	3.2	2.9	2.7	2.9	2.7	2.7	2.9	2.7	2.7	2.7	2.6	2.8	2.9	2.9	2.8	2.8	2.78	2.78	0.1	
24.10																					3.1	0.26

Experiment 2

x (cm)	t -> (min)	1.5	1.75	2	2.25	2.5	2.75	3	3.25	3.5	3.75	4	4.25	4.5	4.75	5	5.25	5.5	ave	stdev
-5.17			1.6	1.7		2		1.4	1.7	1.7	1.9	1.8		1.6	1.7		1.5		1.69	0.18
-2.58	1.8		1.6		1.8			1.6	2	1.6	2	2		1.5					1.72	0.18
0.00			1.9		2.1		1.6		2	2	2		1.8	1.6		1.8			1.85	0.19
2.58			1.7		1.8	2.1	1.9		2.1	2.1	2	2	2	2				1.8	1.93	0.15
5.17			1.8	1.8					2.4	2.4						2			2	0.28
7.75								2.3	2.1	2.1		2.3				1.7			2.1	0.28
10.33							1.9				2.4	2.2			2.3			2.2	2.2	0.19
12.92			2.8		2.1	2.3	2.1	2.3	2.2		2.2							2.2	2.29	0.24
15.50	2.4		2.4	2.4	2.3	2.5	2.4	2.4	2.4	2.5	2.5	2.4	2.6						2.43	0.09
18.08			2.8		2.5		2.4	2.4									2.7		2.6	0.18
20.67	2.7		2.8			2.6													2.75	0.13
23.25	2.6			2.5		2.7		3			2.6								2.77	0.27

Experiment 3

x (cm)	t -> (min)	1	1.2	1.4	1.6	1.8	2	2.2	2.4	2.6	2.8	3	3.2	3.4	3.6	3.8	4	ave	stdev
-5.32			1.9			1.4			1.5		1.6	1.2	1.8	1.7			1.6	1.59	0.22
-2.66						1.4	2.1		1.8		1.5			1.7	1.5		2	1.71	0.27
0.00		1.8		2.2	2.2		1.7		1.4	1.6				1.4	1.9			1.78	0.32
2.66		1.4		1.6	1.6	2.4			1.6	2.2		1.5	2.3	1.7	1.6	2.1	1.5	1.79	0.35
5.32		2.1		2.4					1.6			1.6	2.1		1.8	1.9	2.5	2	0.34
7.98		2.3	2.2	2			2.7		1.8	2.2	2.1	2.1			2.2	1.7	1.7	2.09	0.29
10.60		2.8	2	2.4	2.3									2	2.9	2.6	1.8	2.35	0.4
13.30		1.9				1.9	2.2	3.2		2.1			3.2	2.5	2.5		2.3	2.42	0.49
16.00		3.6								2.3	2.2	2.6	2.2	2.2	2.2		2.2	2.47	0.52
18.60					2.3					2.3		2.3		2.8		2.7	2.6	2.5	0.23
21.30		3.5									2.7		2.9	2.4		2.8	2.5	2.8	0.39
23.90		3.1		2.9													3	0.14	